3 Xenon Detector System

3.1 Overview

The direct observation of WIMP scattering within a radiation detector is a significant experimental challenge. Searches for these elusive particles require an extremely sensitive, low-background instrument able to separate NR events at the few-keV energy from a dominant background of ER interactions, some created by particles external to the WIMP target and others arising within it from radioactive contaminants. The LZ experiment addresses part of the background issue by operating deep underground, and by surrounding the instrument with large ultra-pure water and liquid scintillator shields. However, observing these small energy depositions in space and in time in the central LXe target requires a highly instrumented double-phase (liquid/vapor) Time Projection Chamber (TPC) assembled from high-performance, low-radioactivity components operating in a cryogenic environment. An additional constraint is that the detector must operate as conveyed underground, which demands stringent quality requirements of its components.

While LXe is inherently a very radio-quiet detector material, with high enough density and atomic number to very effectively self-shield against external backgrounds, the design of this new detector requires nonetheless that attention be paid to the radiopurity of a number of significant detector elements, such as the PMTs, their voltage-divider bases, cabling, support structures, and reflecting surfaces. This imposes serious constraints on material composition and their location, adding significant complication to the design of the instrument. The details of these developments will be described in the related sections below.

The Xenon Detector System includes the LXe TPC and ancillary systems required for its readout, monitoring and control. An additional anti-coincidence detector is formed by a layer of LXe enveloping the TPC, which we term the “Xe Skin” detector. The main components of these two instruments are described in this chapter: the TPC, including HV delivery, PMT systems, and internal liquid flow and monitoring instrumentation; and the Skin detector and its readout. We describe at the end of this Chapter our multi-scale System Test effort which is working to validate the performance of many detector components before their assembly into LZ.

An overview of the xenon detector system is shown in Figure 3.1.1. The LZ TPC diameter is determined by the maximum cryostat width that can be conveyed underground and the matching TPC length provides a compact form factor to minimize external radioactivity backgrounds. The TPC itself has a three-electrode configuration: a cathode grid at the bottom, a gate grid just below the liquid surface, and an anode grid just above the liquid surface. It features two arrays of PMTs, one immersed in the LXe viewing up (241 tubes), and the other in the gas phase viewing down (253 tubes). The WIMP target contains 7 tonnes of active LXe, located vertically between the cathode and gate grids and enclosed laterally by a cylindrical arrangement of PTFE reflector panels. These embed a resistive electrical ladder which grades provides an approximately vertical electric field inside the TPC. Interactions in this region generate prompt vacuum ultraviolet (VUV) scintillation light detected by the PMTs (S1 pulse). The applied electric field sweeps the ionization charge liberated at the interaction site and drifts it upward to the liquid surface past the gate electrode; these electrons are extracted into the vapor phase, where they generate electroluminescence—which is again detected by the same two PMT arrays (S2 pulse). This double-phase TPC technique, which generates two optical pulses per interaction, resolves the energy deposition sites with great spatial accuracy down to very low en-

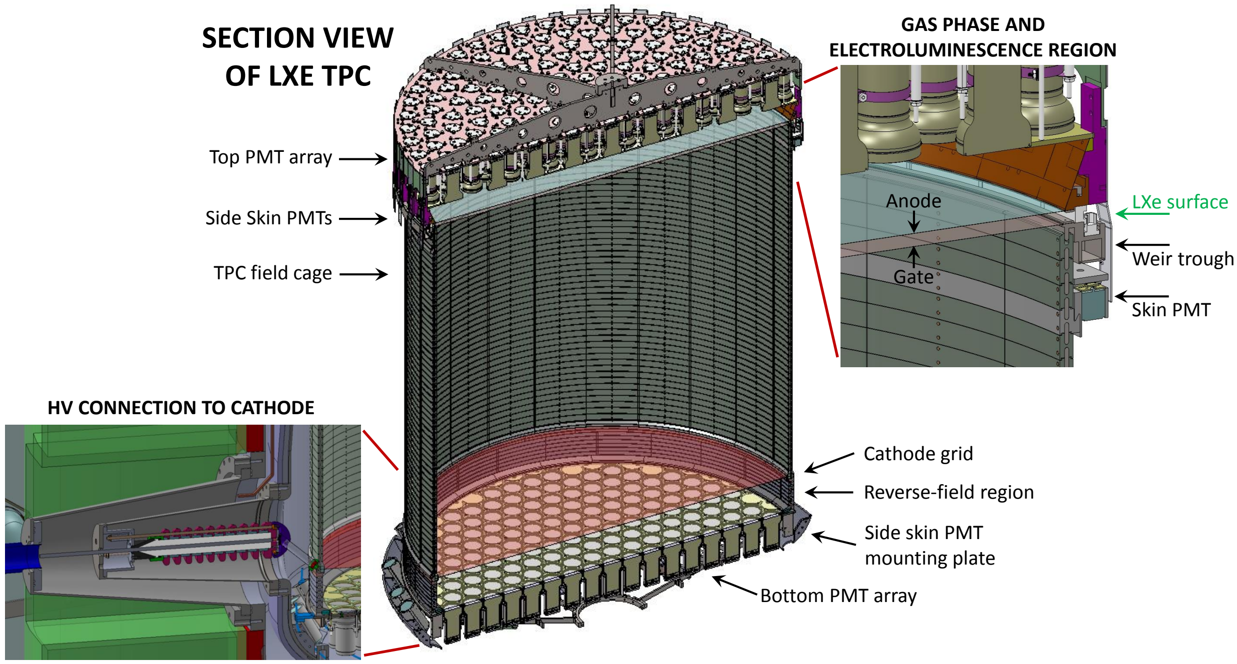

Figure 3.1.1: Schematic views of the Xenon Detector. The 7-tonne active region is contained within the TPC field cage between cathode and gate electrodes, viewed by "top" and "bottom" PMT arrays in the vapor and liquid phases, respectively. S2 signal generation occurs between the liquid surface and the anode (right inset). The HV connection to the cathode (left inset) uses a dedicated conduit leading from outside of the water tank. Below the TPC, a reverse-field region grades the cathode potential to low voltage at the bottom PMT array. The Side Skin PMT readout is shown outside of the TPC field cage.

ergies, allowing identification of multiple scatter events and, as described in the previous Chapter, it provides discrimination between ER and NR interactions.

Table 3.1.1 lists the key design parameters of the Xenon Detector System needed to meet the LZ scientific requirements. An important enhancement beyond LUX is the treatment of the Skin layer of LXe located between the PTFE-clad field cage and the cryostat inner wall, as well as the region beneath the bottom PMT array. A high-quality dielectric standoff is needed between the high electric field regions of the field cage and the grounded vessel wall. A few-cm-thick layer of LXe performs this role, with the added advantage of allowing measurement of any energy deposited in this layer, from which we read out the scintillation light. Operated as a stand-alone veto, this layer is too thin to have high efficiency. However, the combination of this Skin Detector and the liquid scintillator Outer Detector is highly efficient at tagging internal and external backgrounds. The efficiency is further enhanced by the overall minimization of inert materials that can absorb gamma rays and neutrons: The TPC is constructed of the minimum needed mass of PTFE and field-shaping rings, and the vessels and PMT support structures are made of titanium. Both PTFE and Ti have low density and atomic number, and are thus quite transparent to gamma rays. Important design drivers for the Skin are its optical decoupling from the TPC, and compatibility between the Skin readout and the TPC HV design.

Another area of major difference between the device described here and the previous LUX and ZEPLIN detectors is the side-entry method to deliver the high-voltage connection to the cathode, and the relatively short "reverse-field" region (RFR) between the cathode and the lower PMT array. The RFR is especially

Table 3.1.1: Main parameters of the Xenon Detector System.

Parameter	**Value**
Liquid xenon	
TPC active mass	7,000 kg
Skin mass (side+dome)	2,000 kg
Total mass within cryostat	9,600 kg
Photomultipliers	
TPC (Hamamatsu R11410-22)	253 (top) + 241 (bottom)
Top Skin (Hamamatsu R8520-406)	93
Bottom Skin (Hamamatsu R8778)	20 (side) + 18 (dome)
Vertical dimensions (cold)	
Electroluminescence region (gate-anode)	13 mm (8 mm gas)
Drift region (cathode-gate)	1,456 mm
Reverse-field region (sub-cathode)	137.5 mm
Transverse dimensions (cold)	
TPC inner diameter	1,456 mm
Field cage thickness	15 mm
Skin thickness at surface (at cathode)	40 (80) mm
Electric fields	
Electroluminescence field (GXe)	10.2 kV/cm
Drift field baseline (goal)	0.31 (0.65) kV/cm
Reverse field baseline (goal)	2.9 (5.9) kV/cm
Drift (reverse-field) stages	57 (7)
Operating conditions	
Operating pressure (range)	1.8 (1.6 to 2.2) bar(a)
Equilibrium temperature	175.8 K (−97.4 °C)

challenging because of the very high electric field there, which results from balancing a high cathode voltage and minimizing the mass of S2-inactive LXe below the cathode. Our approach to these issues is described below in separate sections on the reverse-field region and cathode HV delivery system.

By design, the structures surrounding the central LXe volume are as lightweight as possible for transparency to gamma rays and neutrons; this also helps to keep their total radioactivity low. The most challenging requirements on the intrinsic radioactivity (i.e., radioactivity per mass or area) are in the largest or most massive components—the PTFE walls and field-shaping rings, and the PMTs with their bases and cables. This Chapter discusses the approach to obtaining the needed radioactivity levels for a number of these major items. However, the absolute level of radioactivity surrounding the detector must be held at acceptable levels, so all components must be carefully selected and screened. The screening program that ensures this is discussed in Chapter 9.

3.2 The Liquid Xenon Time Projection Chamber

At the heart of the LXe TPC are the field cage embedded in the reflective PTFE panels and the various electrode grids. The grids and field cage create the set of electric fields that drift the electrons to create the S2 signal, and the highly reflective PTFE panels are essential for efficient measurement of the initial S1 scintillation signal. In this section we describe the electrostatic design of the TPC, and then highlight optical and thermal considerations that shape this design.

The electric field configuration inside the TPC volume defines three distinct regions: (1) the drift region, (2) the reverse-field region, and (3) the electroluminescence region. We describe these in turn, with help from Figure 3.1.1 which overviews the detector geometry, and Figure 3.2.1 which illustrates the field distributions.

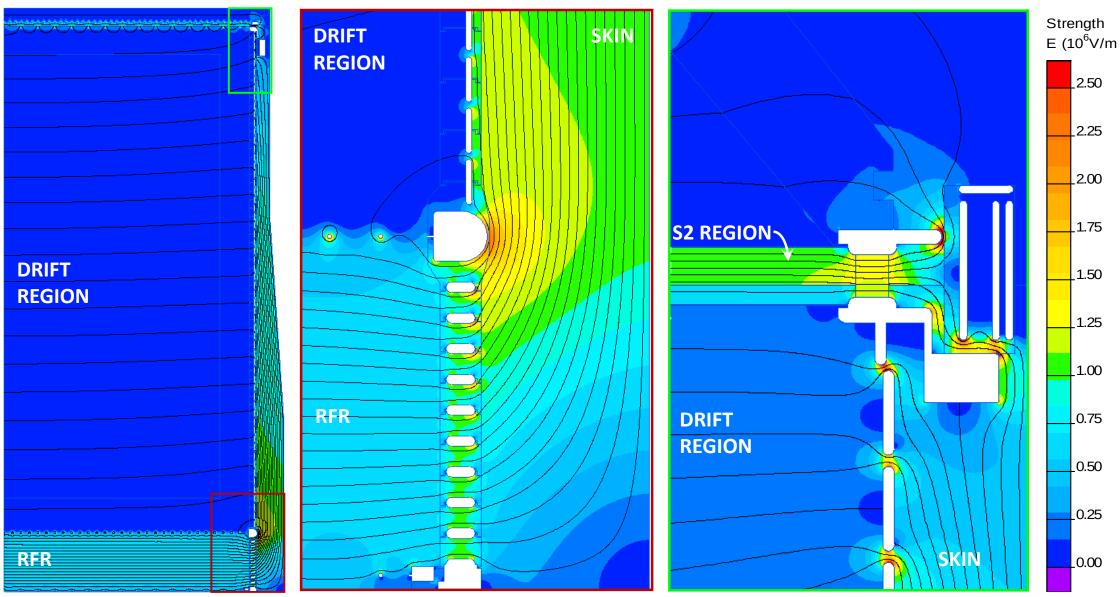

Figure 3.2.1: Electrostatic modeling of the various electric field regions of the TPC; applied voltages are design goals rather than nominal in this figure (cathode: −100 kV, gate: −7 kV, anode: +7 kV); the field on cathodic surfaces in the liquid phase is kept below the 50 kV/cm allowable field. Left: General cross-section showing the drift field in the active region, the side Skin, the reverse-field region below the cathode, and the electroluminescence (S2) region at the top. Center: Detail of the drift and reverse-field regions with field-shaping structures embedded in the PTFE walls (expanding region in red in the left panel). Right: Detail of the electroluminescence region in the TPC top corner (in green in the left panel). In all panels the right-most surface is the grounded inner cryostat wall.

3.2.1 Drift Region

The region between the cathode and gate contains the active volume (WIMP target) and is therefore the most important region of the detector. This is where electrons are removed from the particle interaction site and drifted up to be detected in the vapor layer above the surface. Hence, the electric field strength and uniformity in this region have a major impact on the ability to identify and locate interactions in the detector. It is important that the electric field in this region is as uniform as possible, with field lines parallel to the PTFE reflector walls, so that S2 pulses can be generated for all interactions in this region. The electric field requirement for LZ is 0.3 kV/cm, with a design goal of 0.6 kV/cm. This range will provide the required level of ER/NR discrimination of 99.5 % or better.

An additional requirement in our design is that all cathodic surfaces immersed in the LXe must comply with a maximum allowable field of 50 kV/cm. As described in the LZ Conceptual Design Report (Section 3.4.2 in [1]], is can be problematic to sustain higher fields in particular on practical stainless steel surfaces.

To produce a uniform electric field between the cathode and the gate electrodes a set of 57 equally-spaced field rings is embedded within the PTFE and connected by pairs of 2 G Ω high-voltage resistors. The rings will be made from titanium from the same source as that used for the cryostat. The details of the design can be seen in Figure 3.2.1. The rings are "I"-shaped to help maintain the uniform field pattern needed within the TPC region by keeping the equipotential surfaces nearly normal to the inner surface of the PTFE ring. The field-shaping rings are embedded in vertically-segmented rings of PTFE that have been precision machined and then assembled in a stack to produce the completed field cage. In areas where the large difference in thermal contraction between PTFE and the metal field-shaping rings would cause problems, the PTFE rings are additionally segmented in the circumferential direction to allow the PTFE segments to slide along the field rings when the detector is cooled. The field cage structure will be mounted to the lower reverse-field region and lower PMT support, which in turn is supported from the bottom of the cryostat inner vessel.

All electrodes consist of woven meshes made from thin stainless steel wires—these are described in detail in Section 3.6.4. The cathode is at the highest potential and the design of its holding ring must be optimized to avoid high-field regions (see Figure 3.2.1 center).

The issue of field uniformity is important. In LUX it was observed that field lines near the lateral edges of the TPC, particularly near the top and bottom, are not fully parallel to the PTFE surfaces. We have come to understand this as being intrinsic to its design: The overall fields resulting from the grids and field cage structure were designed using 2-D electrostatics calculations that treated the grids as continuous conducting sheets. It is well known [2, 3] that the 3-D stretched-wire grids have an electrostatic transparency such that the bulk electric fields are somewhat (∼10 %) different to the values calculated assuming the grids are conducting planes, and this effect was taken into account in establishing the LZ operating fields. A subtler additional effect happens at the top and bottom of the TPC cylinder, where the transparency of the grids causes some bleed-through of the concentrated fields that terminate on the vessel and other grounded structures just outside the main part of the TPC. A more complete calculation using transparent grids reproduces the observed pattern in LUX. Such an effect was in fact previously observed in XENON100 and understood as described above [4].

In LUX, this effect caused electrons at the bottom edge of the detector to deflect 2 cm to 3 cm inward as they followed distorted field lines. This did not pose a fundamental problem for the science data, since the effect could be readily corrected for in analysis. Nonetheless, we will seek to better control the fields in LZ. Based on preliminary electrostatic calculations, we believe that this effect can be mitigated, for example by adjusting the values of the last few resistors at the top and bottom of the field cage (this is not assumed in this report). Another design change over LUX is the vertically-segmented design of the PTFE field cage walls. The essentially uninterrupted PTFE surfaces of the field cage are necessary for good light collection, but not ideal from the point of view of good high-voltage design practice, because insulating surfaces can at least in principle accumulate charge that distorts fields. LUX was constructed from single, continuous slabs of PTFE in the vertical direction, whereas the 2.5-cm-tall segments in LZ provide much shorter paths to the conducting field rings from any location on the PTFE walls.

3.2.2 Reverse-Field Region

Located between the cathode grid and the bottom PMT shield grid, the RFR is a significant challenge for constructing the LZ TPC because of the high fields involved (3 kV/cm to 6 kV/cm). The cathode voltage must be graded to near-ground while keeping all surfaces in this region below the 50 kV/cm allowable field.

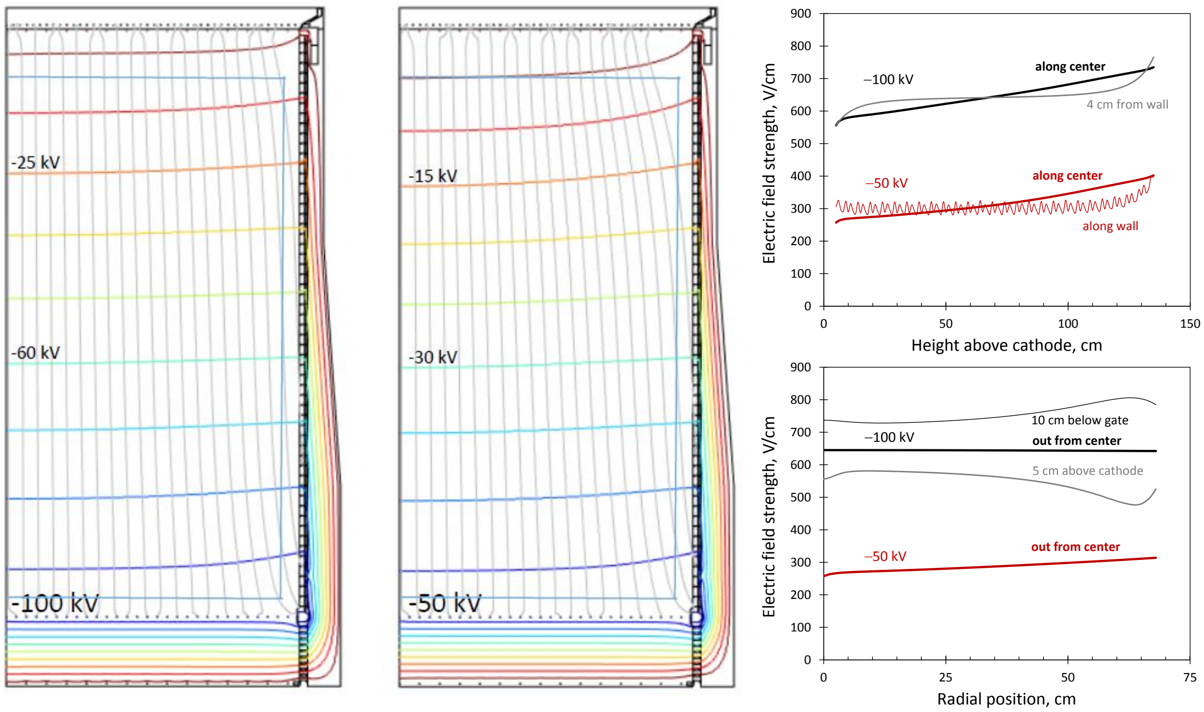

Figure 3.2.2: TPC field uniformity. Left and center: Equipotential lines and electron trajectories for −100 kV and −50 kV cathode HV. In both cases a preliminary 5.6-tonne fiducial volume is shown which extends from 5 cm above the cathode to 10 cm below the gate, out to 4 cm from the TPC tall. Right, top: Field magnitude vertically along the center of the fiducial volume as well as along the TPC walls; Right, bottom: Field strength horizontally out from the center at the bottom, middle and top of the fiducial volume.

At the same time, this space must be kept as small as possible, both to reduce the amount of expensive LXe in this region, and to reduce the rate of events that scatter in both the reverse-field region and the active volume of the TPC. Such events are a class of background that can mimic WIMP signals; however, they have an acceptably low rate for the design presented here. In the LUX detector, due to the much lower cathode voltages and the shorter drift region in the TPC, this was handled with a 4 cm spacing and no field grading between the cathode and PMT shield grids, along with a near-zero field region of 2 cm between the shield and the PMT front surfaces. For the LZ configuration, we have chosen a voltage-grading structure similar to that in the drift region. This better defines the fields, and is a more robust approach to the more challenging LZ voltage requirements.

The RFR design, shown in Figure 3.2.3 (left), is composed of a stack of eight PTFE “rings”, each ≈1.5 cm high and embedded with titanium field-shaping rings. These conducting rings are optimized for field uniformity above the PMTs—to control the electrical environment near their input optics—while keeping the region between the TPC and the grounded cryostat below 50 kV/cm. The central panel in Figure 3.2.1 shows the fields in this region. The smooth oval shape of the RFR rings, compared with the “I”-shape in the drift region, creates lower surface fields on these elements at the expense of a less-uniform field in the central LXe region. This is not problematic since the uniformity requirement is not strong in the reverse-field region.

The voltages between each of the field rings are graded down from the cathode potential using a set of series resistors, similar to those used in the drift region, but with a higher resistance value between each ring to accomplish this stronger field grading. The resistors in the reverse-field region are more challenging

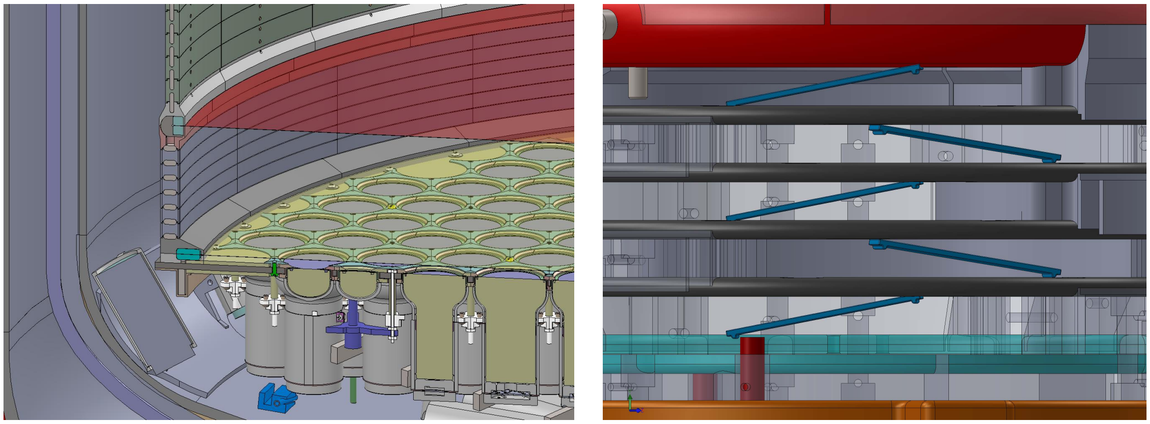

Figure 3.2.3: Reverse-field region design. Left: The RFR, with the cathode and bottom shield grids visible, and the oval field-shaping rings used here. Right: Placement of the RFR field-grading resistors, which are embedded inside the PTFE ring structure and attached to successive field-shaping rings.

for radioactivity than those in the drift region because they are larger. The main radioactive challenge in electronic components is alumina ceramics, which in all standard (non-"synthetic") forms is very high in both gamma activity and neutron yield. We use standard surface-mount resistors with the exception of getting the manufacturer to make them with a thin protective glass coating instead of potting them in epoxy. The resistors have the smallest available ceramic mass for the required voltage rating. Figure 3.2.3 (right) shows the current design and location of these grading resistors inside the PTFE spacers. The lowest PTFE "ring" will be attached to the top of the lower PMT shield grid and this grid will be spaced approximately 2 cm above the PMT surfaces, also using a PTFE spacer ring. The entire assembly will in turn be attached to the lower PMT support structure, which will then be fixed to the cryostat for final mechanical support. Electrostatic and mechanical studies of this region have been carried out, and are part of the System Test program described at the end of this Chapter.

3.2.3 Electroluminescence Region

In the region above the gate grid, drifting electrons are emitted across the liquid surface and produce electroluminescence (S2) photons while traveling through the gaseous phase on their way to the anode. The separation between these electrodes is merely 13 mm, since only a narrow gas gap (8 mm) is required to provide enough S2 gain. Fields here are necessarily high (≈10 kV/cm in the gas phase) demanded by both the cross-phase electron emission process and the S2 photon production. The field in the liquid above the gate is approximately half that in the gas above the surface due to the relative permittivity of the liquid phase ($\epsilon_r = 1.96$).

The optimization of the grids to create the S2 signal requires care, as is discussed in detail in Section 3.6; the mechanics of having gate and anode grids with very low deflection from the large electric fields is challenging; both the Skin PMTs (Section 3.7) and the weir structure (Section 3.8) must be accommodated in a tight space; and the overall structure must maintain a very low level of distortion in the rings supporting those grids, so that a parallel arrangement of electrodes and liquid surface can be obtained (tip-tilt adjustment of the detector to assure parallelism of grids and liquid surface is discussed in Chapter 5). A close-up view of this region is shown in Figure 3.2.4.

The field in the liquid above the gate must be significantly stronger than the field in the drift region: a ≈5-kV/cm "extraction" field is needed below the liquid surface in order to give most electrons sufficient kinetic energy to overcome the energy barrier at the liquid surface (0.61 eV) and be extracted into the gas

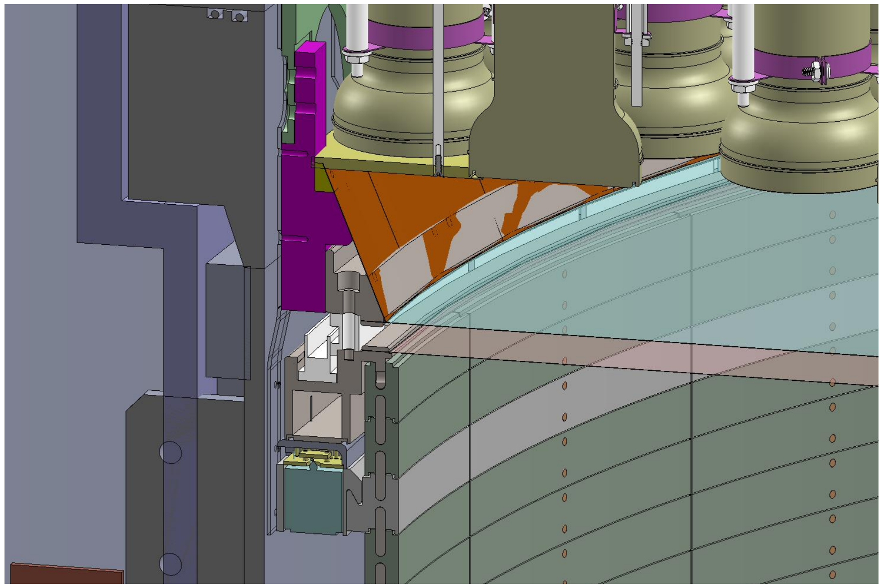

Figure 3.2.4: The electroluminescence region, with the gate and anode grids shown, along with the weir and top Skin PMTs.

phase with high probability [5]. Once electrons enter the gas phase, where the field is approximately twice as strong, they are accelerated and produce electroluminescence photons in the 8-mm drift distance until they are collected on the anode grid. The photon yield is ≈800 photons per emitted electron at 1.8-bar operating pressure, with 10 kV/cm in the gas [6]. For these operating conditions, the electron transit time to the anode is ≈1.2 μs which, along with diffusion while the electrons travel in the drift region, determines the width of the S2 pulse.

Because the S2 signal develops as the electrons drift from the liquid surface to the anode electrode, it is essential to minimize the variance of S2 photon production for different electron emission points, as this relates directly to the energy resolution achieved in the S2 channel. This imposes requirements on grid deflection as well as micro-uniformity of electric fields. The intricacies of this design are described in Section 3.6. Additional constraints come from the need to attach other elements to the side of this region of high field, such as the weirs that control the liquid level and the side Skin PMTs—this can be appreciated from Figure 3.2.1 (right). The "top corner" of the TPC is a crowded region and required significant design effort.

3.2.4 VUV Reflectors

In the same way that the electrostatic design of the TPC optimizes the detection of ionization electrons extracted from particle interactions, the optical design must accomplish the harder task of maximizing the detection of scintillation photons. Although the numbers of each quanta produced initially are comparable, it is easier to detect electrons efficiently than it is to detect photons. The energy threshold of the TPC is therefore determined primarily by its ability to detect prompt scintillation (S1).

PTFE is the VUV reflector of choice for this purpose, possessing good mechanical properties, low outgassing, and—crucially—achieving hemispherical reflectances in the liquid xenon as high as ≈97 % at the xenon scintillation wavelength. The experience of the LUX experiment in optimizing light collection within the TPC volume was very successful, translating to a very low NR detection threshold of below 4 keV. We plan to use machined "segments" of high-purity PTFE approximately 1.5 cm thick and 2.5 cm tall to form the inner reflecting surface in the TPC region as well as the outer reflecting surface between the TPC and the cryostat wall, which itself will have a one-mm-thick segmented lining of PTFE.

There are many types of PTFE exhibiting different reflectivity both in the liquid and gas phases [7, 8]. It is essential that the best material is selected for this purpose since this is a leading parameter that determines the performance of both the TPC and the Skin detectors. The topic of S1 photon detection is discussed in some detail in Section 3.5; the PTFE reflectivity is such a critical parameter that we devote part of our System Test program to this topic, as described in Section 3.10.

The radioactivity of this material must be held extremely low both because of direct gamma-ray production but, more importantly, neutron production from (α,n) reactions on F from α decays in the U and Th chains. The raw precursor material for structural PTFE is a powder form produced by only a few suppliers, and is expected to be extremely radio-pure because it is synthesized from gas. A large number of smaller manufacturers produce structural shapes from these powders, and the final material can be very low in radioactivity if there is sufficient care in controlling contamination (e.g., from dust) in this second manufacturing step. In this topic we benefited from the experience of the EXO-200 collaboration, who achieved excellent radiopurity, rendering this critical material sub-dominant in terms of background in LZ, as detailed in Chapter 9.

3.2.5 Thermal Considerations

Given that the inner detector region is primarily made from PTFE, stainless steel and titanium parts, attention must be paid to the differential thermal contraction as the detector is cooled to LXe temperatures. The PTFE that makes up the majority of the surface area of the TPC is expected to shrink by ≈1.5 % linearly [9, 10], or about 7 cm in circumference and 1 c̃m in TPC radius when cooled from room temperature to ≈170 K. Stainless steel, by contrast, contracts only ≈0.2 % over the same temperature range, and titanium even less. Where this difference would result in destructive forces in the assembly, the metallic field cage rings will be constructed as solid parts, while the PTFE parts are segmented both horizontally (i.e., into rings) and vertically, so that each ring is itself composed of several segments. These segments contract and slide circumferentially along the solid metal field cage rings. In this way, the overall diameter of the TPC is determined by the metal field cage rings, and thus undergoes a relatively small thermal contraction. As the PTFE shrinks, the seams between the segments open, but the design has overlaps so there will continue to be a reflecting surface in the exposed gaps. In the vertical direction, the dimension of the field cage is determined by a combination of PTFE panels and metal rings. There is an overall height (top PMT array to bottom PMT array) contraction of ≈1 cm. To minimize the movement in the critical region where the HV connection to the cathode is made (discussed in Section 3.3), the entire TPC assembly will be supported from the bottom PMT array, which will be connected to the cryostat vessel. This means that the top PMT array will move downward during cool-down, increasing the clearance in the top dome.

3.3 Cathode HV Delivery System

3.3.1 Cathode HV Requirements

The cathode HV is a key performance parameter that will directly affect the science reach of the instrument because of its impact on ER rejection and other factors. Table 3.3.1 summarizes the HV requirement and some detector parameters it determines. The LZ nominal operating voltage is −50 kV, which establishes a drift field of ≈300 V/cm and allows LZ to meet its baseline sensitivity. The design goal is −100 kV—the maximum operating voltage for the system. Introduction of HV into the Xe space is challenging because of possible charge buildup and sparking, and since high-field regions can produce spurious electroluminescence that blinds the detector to the minute flashes of light produced by WIMP interactions.

Table 3.3.1: Dependence of TPC parameters on cathode HV.

Parameter	−30 kV (LUX)	−50 kV (Base)	−100 kV (Goal)	Comments
TPC drift field, kV/cm	0.17	0.31	0.65	Gate −5.5 kV
ER/NR discrimination	99.6 %	99.7 %	99.7 %	NEST LZ04
Electron drift velocity, mm/μs	1.5	1.8	2.2	[11]
Maximum drift time, μs	970	806	665	Interactions at cathode
Longitudinal diffusion, μs	2.4	2.2	2.0	FWHM, cathode events
Transverse diffusion, mm	2.4	1.8	1.4	FWHM, cathode events
Gate wire field, kV/cm	−64	−62	−58	
Cathode wire field, kV/cm	−18	−31	−63	

The LZ operating and design voltages were determined through a combination of task-force activity, evaluation of WIMP sensitivity, and project cost and risk. At the nominal voltage, an ER rejection efficiency of 99.5 % is expected at 50 % NR acceptance, as demonstrated in previous double-phase Xe detectors and modeled through the Noble Element Simulation Technique (NEST) simulation package. The LZ cathode is required to operate up to −50 kV; in addition to allowing adequate discrimination power, this voltage further minimizes drift time, event pileup, charge cloud diffusion, and optimized energy resolution. All subsystems in LZ will be designed to withstand higher voltages to help ensure that a −50 kV operational voltage can be met. High voltage tests of LZ prototypes and final components will also be done to ensure this voltage capability. The planned design safety factors (DSFs) and test safety factors (TSFs) are summarized in Table 3.3.2.

Table 3.3.2: Design safety factors (DSFs) and test safety factors (TSFs) for the cathode high voltage delivery system. The DSFs and TSFs are defined as percentages above −50 kV (e.g. a 100 % safety factor implies a voltage of −100 kV).

Item	Design Safety Factor	Test Safety Factor
Cathode power supply	140 %	140 %
Warm feedthrough	200 %	200 %
Cable	200 %	200 %
Grading region	100 %	140 %
Cathode connection region	100 %	140 %

3.3.2 HV System Overview

A schematic overview of the cathode HV system is shown in Figure 3.3.1. The baseline LZ design places the cathode HV feedthrough (from air into Xe space) outside the shield at room temperature, at the end of a long vacuum-insulated, Xe-filled umbilical. The cathode high voltage cable has been chosen to be Dielectric Sciences model SK160318. It is rated to 150 kV, and has a conductive polyethylene core, polyethylene insulator, and conductive polyethylene sheath. With the dominant cable material being polyethylene, Rn emanation is minimized. Polyethylene is also known to be a safe material in LXe, mitigating concerns about emanation of electronegative contaminants. With the feedthrough at room temperature and far away from the active LXe, there are no concerns of thermal contraction compromising a leak-tight seal to the Xe space, and no concerns about feedthrough radioactivity. A feedthrough at the warm end of the umbilical allows a commercial polyethylene-insulated cable to pass from a commercial power supply, through a double O-ring seal, and into the gaseous Xe. The cable then travels through the center of the umbilical and routes the HV through LXe and to a field-graded connection to the cathode.

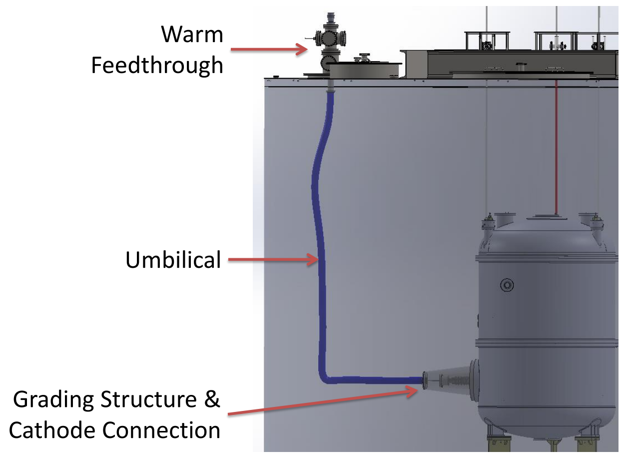

Figure 3.3.1: Schematic overview of the cathode HV delivery system.

3.3.3 Cathode Supply and Cable Connection

The cathode grid power supply (Spellman SL120N10) is rated at −120 kV and is limited to a maximum current of 100 µA. This power supply has an adjustable current trip feature which can be used to shut the power supply off in the event of an over-current condition such as HV breakdown to protect the load. The output cable leads directly into the warm feedthrough, and from there into the xenon space and cathode connection region.

3.3.4 Cathode Feedthrough

The warm cathode HV feedthrough, shown in Figure 3.3.2, allows high voltage to be passed from outside the LZ detector into the top of the Xe-filled umbilical space. The HV cable passes continuously through the feedthrough, with electric field confined to the cable insulation. The feedthrough includes 2 O-rings that seal to the outside of the conducting outer sheath of the HV cable. Between the O-rings is a vacuum space, maintained with a turbopump and monitored with a residual gas analyzer. The first O-ring allows the cable to pass between air and vacuum, and the second O-ring allows the cable to pass from vacuum to xenon gas in the umbilical. The cable is supported mechanically, both in air before the first O-ring, and in the xenon gas space after the second O-ring.

3.3.5 Cathode HV Umbilical

The cathode HV umbilical is designed to carry the Dielectric Sciences HV cable from the warm feedthrough to the cathode of the detector. The umbilical is a nested pair of tubes that protrude from the side of the detector at about the height of the cathode. The tubes include formed bellows for flexibility, and after leaving

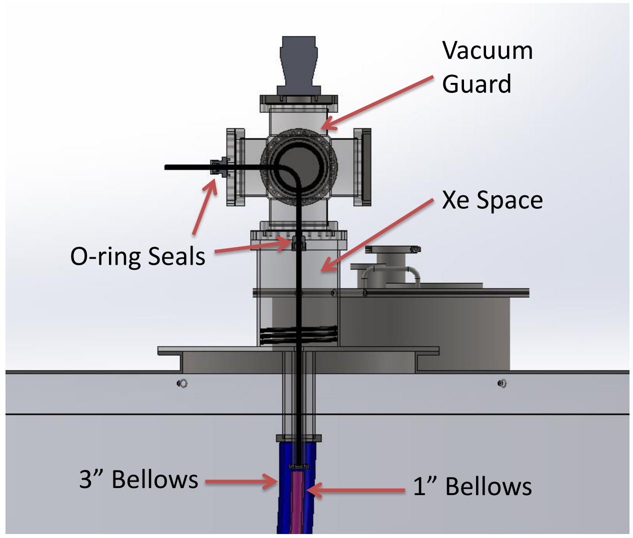

Figure 3.3.2: Warm feedthrough detail for the HV connection to the cathode.

the cryostat horizontally, bend upward to the top of the water tank. The HV cable is also flexible, allowing it to turn with the umbilical.

The 1-inch-diameter inner tube of the umbilical is connected to the Xe space and is joined to a stainless steel cone that makes a seal to the inner vessel of the detector. To avoid gas bubbles within the cone that might cause electrical discharge, the cone is cooled through a conducting strap in the vacuum space that connects to a detector thermosyphon. The 3-inch-diameter outer tube of the umbilical contains vacuum and is similarly connected to the outer vessel of the detector.

The outside of the outer tube is immersed in the water of the tank. The evacuated space between the tubes contains super-insulation reflective wrap and acts to thermally isolate the Xe space from the water. This allows LXe to fill the inner tube of the umbilical until it reaches a height equal to the level of the Xe surface inside the detector. Thus the lower part of the umbilical is filled with LXe, while the upper part contains Xe gas. The long length of LXe is necessary to accommodate the field-grading region of the HV cable.

A gas return to the circulation pump connects to a tube that leads inside the xenon-filled inner umbilical to just above the liquid surface. This port allows control over the flow of Xe boiling in the lower umbilical. A second port connects to the high end of the umbilical, to slowly purge xenon exposed to the warm cable directly to the Rn scrubber system. Finally, the high end of the umbilical connects to the warm HV feedthrough. The feedthrough and umbilical are supported by the top of the water tank.

3.3.6 Spark and Discharge Mitigation

The field-grading structure at the cold end of the HV cable, shown in Figure 3.3.3, allows for the ground braid of the cable to terminate while the polyethylene insulation and conductive center of the cable continue. The departure of the cable ground braid from the cable surface is gradual, and connected to a stress cone made of conductive polyethylene. The stress cone is cryofitted within a xenon-displacing polyethylene wedge, which expands to a polyethylene tube that tightly surrounds the cable insulation. As this tube is larger in outer radius that the commercial cable, the field within the LXe is reduced in comparison with a design that only relied upon the cable insulation. This polyethylene structure is long in order to minimize the electric field parallel to the surface of the cable, and is surrounded by 20 field rings made of conductive plastic. These rings enclose coil springs that grip the cable circumferentially and provide electrical contact to its surface. The field rings are connected in series by small resistors to establish a uniform voltage grading between them. The highest potential ring is connected to the center conductor of the cable, while the lowest potential ring is connected to the cable ground braid. The surfaces of the rings are heavily rounded, and the resistors are nested between them. This minimizes the field within the LXe that surrounds the grading structure and separates it from the grounded wall of the inner tube of the umbilical. The grading ring structure is supported by three rods entirely from its grounded end, which is attached to the inside of the umbilical. The rods are pulled by springs to the ground end, and the rods compress the ring structure for rigidity. The entire grading structure is immersed within the LXe; all sections of the cable within Xe gas have an intact ground shield. The end of the grading structure connects to a rounded mushroom head, also made of conductive polyethylene, which captures the spring connection to the cathode.

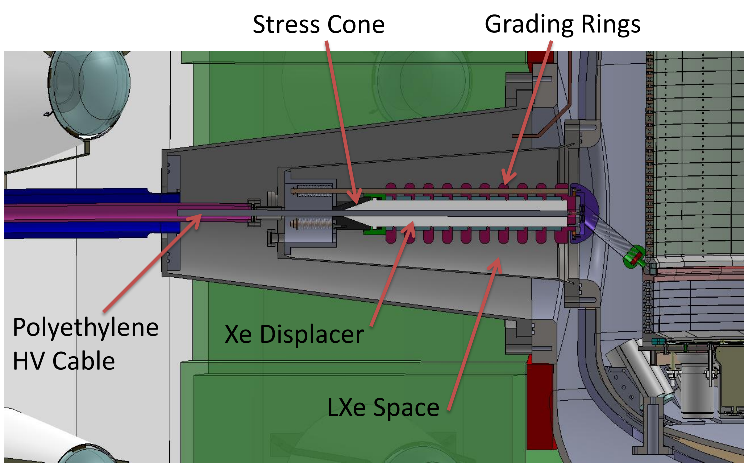

Figure 3.3.3: Schematic of the flexible HV connection to the cathode grid, showing details of the field-grading structures on the incoming HV cable required to keep the fields in the LXe below 50 kV/cm.

3.3.7 HV Connection to Cathode Ring

A schematic of the HV connection to the cathode is shown in Figure 3.3.4, and the simulated electric fields in this region are shown in Figure 3.3.5. Because the TPC (including the cathode grid) is supported from the bottom of the vessel, the cathode grid moves down approximately 2 mm as the PTFE TPC components contract when the system is brought from room temperature to operating temperature (≈172 K). To account for this movement, there is a compliant spring connection between the end of the grading structure and the cathode grid ring.

The grading structure mushroom head is attached to the spring connection prior to installation into the detector. The lower end of the spring is captured by a rounded cup that has a through hole at its lower end, so that the mushroom head, spring and cup are all one assembly. A loose screw is captured inside the rounded cup. This screw will make the connection to the cathode ring. This screw is captive and cannot fall out of the assembly. The threaded end of this screw sticks out of the lower end of the cup.

During underground installation, the outer and inner cryostat ports are opened. A long narrow screwdriver is inserted through the mushroom head and into the spring, where it engages the head of the captive screw. The end of this screw emerges from the lower end of the cup. The screw inserted into the socket in the cathode ring and tightened. This mechanically and electrically connects the mushroom head to the cathode ring. A disk spring held captive under the screw head provides a constant force that prevents unscrewing.

The end of the cold grading structure is then brought close to the mushroom head. The mushroom head is grasped by hand and pulled toward the end of the cold grading structure, and rotated counter clockwise.

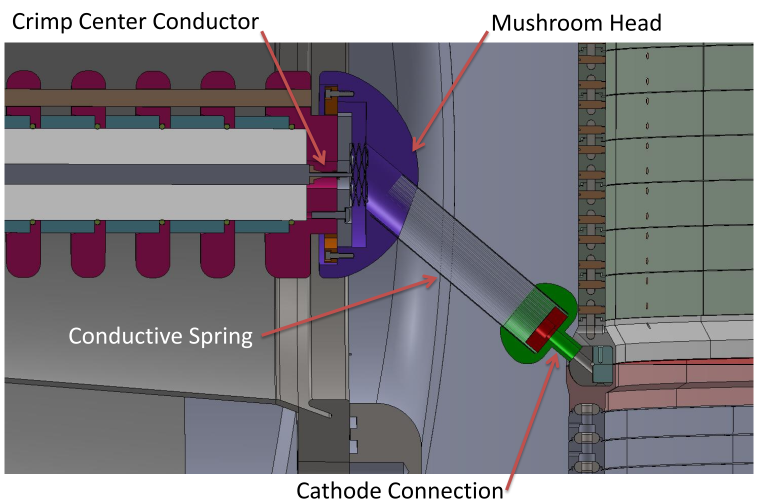

Figure 3.3.4: Schematic of the cathode connection region.

This stretches the spring. The mushroom head is then pushed into the cold grading structure and rotated clockwise. This compresses a wave spring that is held captive on the end of the cold grading structure. The wave spring makes an electrical connection between the cold grading structure and the mushroom head. It also engages detents in the blue cap and provides a force that prevents the unscrewing of the blue cap. The mechanical locking of the mushroom head to the cathode grading structure resembles that of a bayonet mount.

At this point the spring is in its extended position. The spring is relaxed when the inner CHV cone is brought to meet the face of the cryostat. Ports in the back of the inner CHV allow for inspection of the spring to make sure it is located correctly. After the correct position is verified and electrical continuity to the cathode is verified, the bolts connecting inner CHV cone are tightened, making the seal between the inner cone and the inner cryostat.

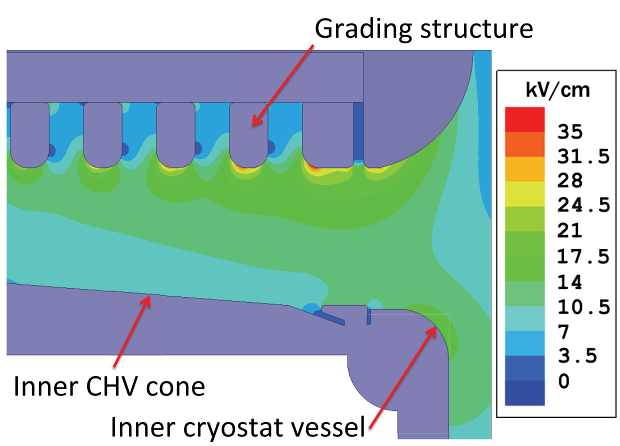

Figure 3.3.5: Simulation of the electric fields in the cathode connection region, assuming an applied cathode voltage of -100 kV.

3.3.8 HV Safety Issues

The combined stored energy from the cathode power supply output capacitance, output cable capacitance, warm feedthrough and umbilical capacitance, and TPC capacitance is 8 J at the maximum operating voltage of −100 kV and is classified as a 3.2C [12] shock hazard per the DOE Electrical Safety Handbook [12]. This shock hazard class indicates that injury or death could occur by contact. To mitigate this hazard, engineering controls are required for operation, and administrative controls are required for electrical work. Specific "lockout/tagout" and grounding procedures will be implemented for various operations such as unplugging the output cable and accessing the internals of the warm feedthrough, umbilical, and the TPC. Each worker who is authorized to perform these tasks will have specific high voltage and capacitor safety training.

3.4 Photomultiplier Arrays

To reach the performance specifications described previously, the Xe detector is equipped with top and bottom arrays of 3-inch-diameter PMTs (Hamamatsu R11410-22) to view the active region of the TPC. A top ring of smaller, 1-inch-square PMTs (R8520) view the scintillation light emitted in the side Xe Skin, with additional 2-inch PMTs (R8778) recycled from LUX complementing the Skin readout at the bottom of the detector. All three PMT types, shown in Figure 3.4.1, have been developed to meet important performance requirements in the field, including good spectral response in the VUV, good single-photoelectron definition, low dark noise, and the ability to operate at LXe temperature—in addition to having ultra-low levels of radioactivity: of order mBq/unit in U / Th / ^{60}Co / ^{40}K for the 3-inch and 1-inch tubes, and a few times higher for the 2-inch units. This section details the properties and deployment of the PMTs for the TPC and Skin. Subsequent sections discuss the design and optimization of S1, S2, and Skin optical signals.

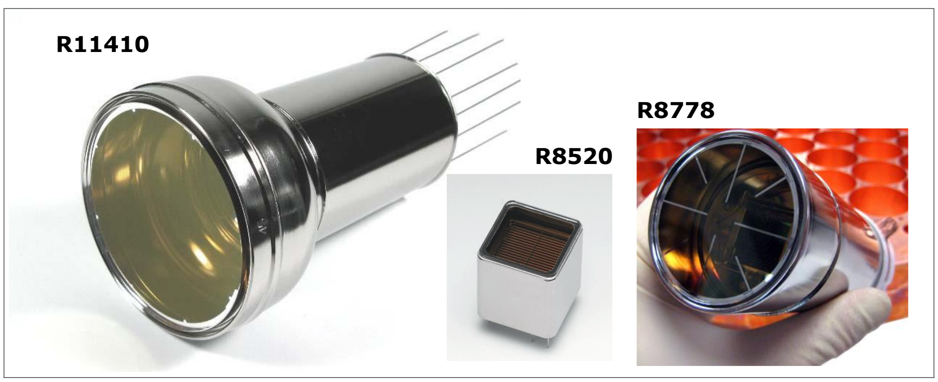

Figure 3.4.1: Photographs of xenon-space photomultipliers in LZ.

The LZ Collaboration has been pursuing the development of low-background PMTs tailored specifically for use in LXe with a radioactivity goal of 1/1 mBq per unit in for U/Th and QE >30 % at 175 nm wavelength [13]. The detector configuration requires ≈500 3-inch tubes. Because of its outstanding radiopurity, the 3-inch Hamamatsu R11410-22 model has been adopted; this tube contains ∼1,000 times less radioactivity than a standard off-the-shelf item and is the result of a coordinated development with the manufacturer and a rigorous screening campaign of sub-components before the items are even manufactured.

The dynode optics in the R11410 are electrically identical to those used in LUX (2-inch R8778), exhibiting similar gain and single photoelectron response. The photocathode diameter is 64 mm. This tube has 12 dynodes and provides a minimum gain of 2×10^6 at 1,500 V bias voltage. The PMTs are assembled to passive voltage-divider bases and will be negatively biased so that the signal can be collected by directly coupling the front-end electronics at near-ground potential. High peak-to-valley ratios (>2) are obtained for the single photoelectron response, which is a key parameter to ensure high detection efficiency for the smallest S1 signals that are composed of single photoelectrons appearing in multiple PMTs.

Aside from good VUV sensitivity, these quartz-windowed PMTs are designed to be operated at LXe temperature featuring a special low-temperature bialkali photocathode with low surface resistivity. This obviates the need for metallic underlayers or conductive fingers [14]. They also have a pressure rating of 4 atm absolute for operation in liquid xenon. Nominal performance will be verified for every unit through a comprehensive low-temperature test program to confirm optical and electrical parameters during and after thermal cycling.

3.4.1 PMT Test Program

The full order of the R11410 PMTs is split between the U.S. (2/3) and the U.K. (1/3), delivered in batches of 40 per month. It is crucial to characterize every PMT before they are installed, and a detailed testing program is designed to test and radio-assay all the PMTs. This is the testing sequence that will be carried out at Brown University for all tubes (except for the confirmatory radioactivity screening, as explained below):

1. Warm test #1
2. Cryogenic test
3. Radioactivity screening
4. Warm test #2

In the first warm test the after-pulsing, gain, single photoelectron resolution, dark count rate and linearity will be measured. These measurements are categorized as "standard testing" and they will identify any PMT that fails to meet agreed specifications for room temperature operation. In the cryogenic test PMTs will be thermal-cycled from 300 K to 160 K and the standard testing measurements will be repeated, plus some exceptional studies such as photocathode uniformity and long-term stability monitoring. The Brown PMT test chamber known as PATRIC, shown schematically in Figure 3.4.2 (left), is designed to hold 14 R11410 PMTs for batch testing. After radioactivity screening (carried out at SURF and Boulby underground laboratories) the PMTs will undergo a second warm test to establish stability over time.

The U.K.-procured PMTs will go through the same test sequence, but a sample of 30 units will undergo characterization of quantum efficiency (QE) and dual-photoelectron emission probability at room temperature and at LXe temperature at Imperial College London. The main goal of the QE test is to establish a statistical correction function to relate the QE at 175 nm obtained by Hamamatsu at room temperature and the relative change of QE upon cooling [15]. The PMT test chamber at Imperial, shown in Figure 3.4.2 (right), uses a xenon scintillation cell maintained at room temperature to shine 175 nm scintillation light into a cryostat containing 7 PMTs (6 under test plus a reference tube) which are cooled to LXe temperature. Correlation of QE data with PMT gains, dark counts and the QE values provided by Hamamatsu will also be studied.

3.4.2 PMT Radioactivity

Due to their complexity, total mass (≈100 kg), and proximity to the active volume, the Xe-space PMTs are a significant source of radioactivity background in LZ. For this reason, they will be subject to a thorough screening campaign using HPGe detectors (see Chapter 9). Screening of fabrication materials and subcomponents has taken place prior to PMT manufacture, and every assembled PMT will again be screened after delivery from Hamamatsu.

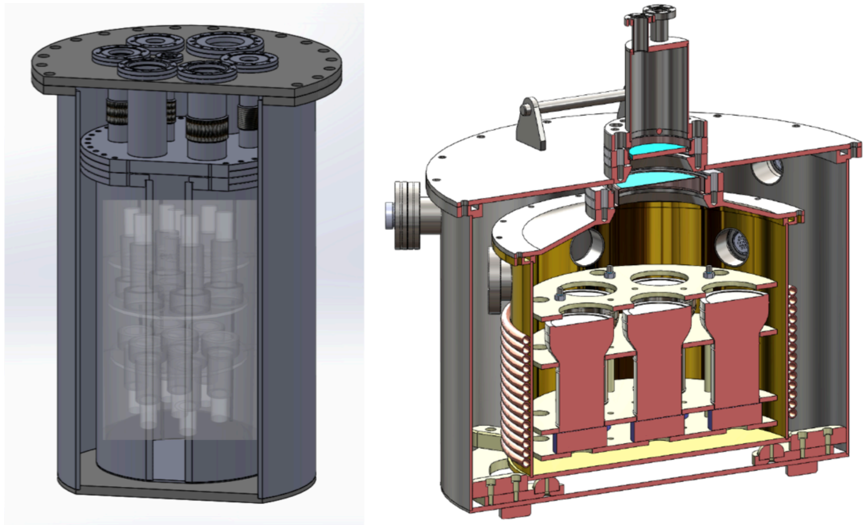

Figure 3.4.2: PMT test setups. The Brown PMT Array Test Rig In Cryogens (PATRIC), shown on the left, is a pressure vessel that can test 14 PMTs at LXe temperature and pressure. After the R11410 PMT testing is completed, the chamber will be modified to test R8520 PMTs. The Imperial setup on the right uses a xenon scintillation cell on top of a vacuum cryostat, shining onto 7 PMTs located in cold nitrogen gas.

The 3-inch R11410 has been delivered in part through a 4-year NSF S4 development program with Hamamatsu, which achieved unprecedented radioactivity performance compared with previous generation tubes [13, 16]. This same model has also been advanced by other collaborations, notably XENON1T with variant R11410-21. Comprehensive radioactive screening results for 216 of these PMTs are publicly available [17]. Screening results from our prototype tubes are in broad agreement, and the pre-screening of construction materials also yielded similar results to those obtained by XENON1T—as detailed in Chapter 9. LZ will procure the most recent (-22) version of these tubes.

The 1-inch R8520 PMTs used in the top side of the Skin Detector have radioactivity levels that are well understood thanks to their wide use in previous detectors. Nevertheless, they will follow the same screening procedures as the larger R11410 model. The contribution of the 93 Skin PMTs to the background of the instrument is sub-dominant given their comparable specific activity but more peripheral location and smaller number.

The 2-inch R8778 PMTs used in the bottom of the Skin Detector will be reused from the LUX experiment and are also well understood from both a radioactivity and performance perspective. Although they have somewhat higher radioactivity per PMT relative to the R11410 PMTs, their background contribution is also sub-dominant given their peripheral location and small number.

3.4.3 PMT Bases

Individual voltage-divider bases connected to two coaxial cables (for HV bias and signal) are attached to each PMT. Given their locations, these components are under detailed scrutiny as part of the radioactivity and radon-emanation screening programs, and they must meet also demanding requirements related to operational reliability and xenon poisoning.

The electrical circuits are shown in Figure 3.4.3 for the 3-inch and 1-inch tubes (the 2-inch R8778 base is similar to the former), and a prototype base for the R11410 PMT is shown in Figure 3.4.4. The voltage distributions are those recommended by Hamamatsu. High-resistance chains are used for

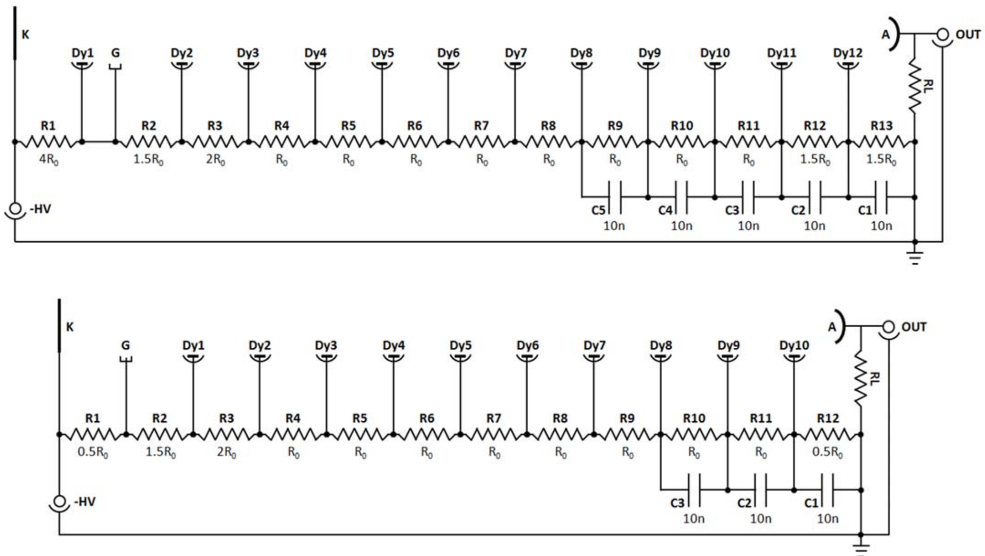

Figure 3.4.3: Photomultiplier base voltage-divider circuits for the R11410 PMT (upper panel) and R8520 PMT. In both cases the voltage distribution recommended by Hamamatsu was adopted, with R_0=4.99 M Ω. R_L=49.9 Ω for the R11410 base and R_L=100 k Ω for the R8520 base. The 2-inch R8778 Skin PMT bases will employ the same circuit design as the 3-inch R11410 units.

low power dissipation in the LXe: 24.3 mW/unit at the nominal 1,500 V for the 3-inch PMTs, and 10.3 mW at 800 V for the 1-inch PMTs. This is required for minimal impact on the thermal design of the detector and to prevent localized bubbling of the liquid. We have confirmed the bubble nucleation threshold of liquid xenon as ≈20 mW/mm^2, in agreement with Ref. [18]; all resistors operate far from this value. Still, the divider current is much higher (≈100×) than the average PMT anode current expected during calibration, which is required for response linearity. Anode pulse linearity is also addressed by charge supply capacitors (10 nF, de-rating to ≈8 nF at LXe temperature) which are added to the last few dynodes. Our main requirement ensures accurate response to ^{83m}Kr calibration events, translating to percent-level non-linearity in top-array channels for S2 signals from this key calibration source. This determines a minimum of five decoupling capacitors for the TPC PMTs. These S2 signals also approach the ±5 % pulse non-linearity expected in these PMTs above ≈20 mA anode current.

The bases are made from thick polyimide (Cirlex™) PCBs with surface-mounted passive components. Cirlex is a good material for this purpose, having very high dielectric strength, a low thermal expansion coefficient, high tensile strength and low internal stress. It is, however, prone to delamination and fiber release at the edges, demanding careful quality control. The Cirlex is patterned with standard photo-lithography and the cutout and drill-holes are made with a PCB router—all processes are conducted in-house to ensure strict control of radioactivity and cleanliness. Candidate components and full prototypes were tested in gaseous and liquid xenon for electrical resilience and outgassing as

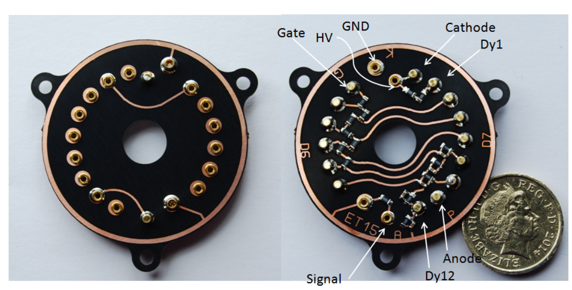

Figure 3.4.4: Prototype of the R11410 PMT voltage-divider base.

well as for spurious optical photon emission. All bases will be thermal-cycled in LN_2 and tested at ambient temperature for 5 days above their maximum allowable voltage. Final inspection, cleaning and radon-tight packaging are conducted in a class 1,000 cleanroom.

The radioactivity performance of the PMT bases is of special concern, both from the point of view of neutron/gamma emission and from radon emanation. Although Cirlex is intrinsically a radio-clean material and a good Pb-free solder has been identified, the discrete components have significant U/Th contributions in spite of the small masses employed. The X7R ceramic capacitors, the thick-film ceramic-chip resistors, and the PMT-pin receptacles all posed significant challenges and we radio-assayed some 25 components in order to select a viable set meeting our radioactivity goal—to be sub-dominant to the PMTs. Ceramic capacitors have typically high uranium content, with those selected (Kemet, 0603 package) showing the lowest levels (11.5 mBq/g); fortunately, the XR7 ceramic is barium titanate (confirmed through SEM/EDX elemental analysis) which has an order of magnitude lower intrinsic neutron yield than alumina, making these components viable—although they pose some radon emanation risk as discussed below. The selected resistors (Vishay, 0805 package) showed acceptable levels of U/Th (<1 mBq/g), but high levels of ^{210}Pb (found in all models tested); the resulting (α,n) yield on the alumina becomes a significant contribution to the neutron yield from the bases. Finally, the greatest challenge came from the receptacles that mate to the PMT contact pins and to the cable connectors. These contain BeCu alloy spring clips which are very "hot" in early uranium (≈100× out of equilibrium). Avoiding the use of these sockets by directly soldering to the PMT pins and cables would have cleanliness implications that would delay the integration sequence of the PMT arrays, and was thus not considered an attractive option. We identified suitable sockets from Harwin which feature $CuNi_2Be$ alloy spring clips within a brass shell; these have lower Be content (0.4 %) and lower radioactivity than the other models we assayed (note that ≈50 % of ^{9}Be (α,n) reactions can be vetoed due to the 4.4 MeV gamma ray [19]; this was considered in the background calculations). In conclusion, we were able to obtain a suitably low radioactivity content, where no single component dominates too significantly, balanced against practical considerations such as robustness and ease of integration. The bottom-up radioactivity estimates are: 390/140 µBq/unit in mid-U/Th for the R11410 and R8778 base (0.06 n/yr) and 230/80 µBq/unit for the R8520 base (0.04 n/yr), respectively.

Radon emanation from the bases was a concern, prompted especially by the total ^{226}Ra content observed in the capacitors. Fortunately, the ^{222}Rn emanation rate measured from a very large number of these components was found to be below 1 % relative to production even at room temperature. The emanation from all bases in the xenon space is expected to be ≈1 mBq at ambient conditions; a modest reduction with cooling is expected from the resistors and capacitors, while the Cirlex should exhibit a significant decrease. Therefore, expect the bases to make a limited contribution to the LZ radon budget (and to confortably meet the radon budget requirement).

3.4.4 Cabling

The PMT signals and HV supplies are carried separately between the PMT bases and the warm breakout interface by low-radioactivity coax cables. The baseline design is to use Gore 3007 Coax with no outer jacket, the same cable that was used in this role for LUX. The 50 Ω characteristic impedance cable uses an AWG 30, silver-plated, Cu-clad steel, surrounded by an AWG 40 stainless steel braid. The cables from the PMTs associated with the upper and lower parts of the TPC are housed in separate conduits, so that no cabling is routed through the side Skin region (these conduits can be seen in Figure 1.2.1 in Chapter 1). This could interfere with the ability to hold a high voltage on the cathode and it would degrade the light collection efficiency in the Skin.

The lengths of typical top and bottom cables are 12.8 m and 11.6 m, respectively. The upper routing carries 801 cables and the lower routing consists of 625 cables, as listed in Table 3.4.1. The total heat load calculated

Table 3.4.1: Coaxial cables in the xenon space routed via upper and lower conduits.

	Upper	Lower
TPC PMTs	506	482
Skin PMTs	186	76
LED calibration	39	45
Dummy channels	11	11
Monitoring sensors	59	11
Total	801	625

from the cables is less than 6 W, which is a sub-dominant contribution to the thermal model. The total cable length within the xenon space is ≈17 km, weighing some 72 kg.

A screening program has been initiated to measure the radon emanation from the baseline cabling, as well as possible alternatives, to ensure that the finally selected model will meet the overall Rn requirements discussed in Chapter 9. Rn emanation from cables is expected to be dominated by the warm region, which is ≈8 m long for the upper routing, and only ≈1 m for the lower routing. To mitigate excessive Rn emanation due both to dust and radioactivity of the cable materials, we are evaluating the benefit of having the cables sheathed in a 150 µm thick coat of FEP Teflon to reduce the rate of Rn reaching the active detector volume. The MJD and GERDA collaborations have observed that including such a FEP jacket provides a suitable Rn barrier in their detectors. Emanation from the feedthroughs (which were previously used in the LUX experiment) will also be measured. Finally, we are planning to add a radon trap to the gas purification system, as discussed in Section 6.4.5, to address emanation from the cables and room temperature feedthroughs.

The Gore 3007 cable has been tested and shown to support 2 kV, comfortably meeting the HV requirements of all PMTs. The way the cable affects the signal characteristics can be seen in Figure 8.3.8 in Chapter 8, which shows the effect of a full cable run (internal and external to the detector) on the single photoelectron response of a R11410 PMT. For these signals there is an amplitude reduction of 47 % and a pulse area loss of 20 %.

3.4.5 Assembly and Integration with TPC

The 253/241 PMTs per top/bottom array will be assembled onto titanium support frames. The PMTs will be held in position using cobalt-free metal belts fabricated by Hamamatsu from the same material used for the PMT body production. Three PTFE columns will then be used to hold the collar to the PMT mounting plates, as shown in Figure 3.4.5. This mounting system is specified to hold the PMTs in place in the Ti mounting plate both when the plate is in the vertical and horizontal orientations (during assembly and transport).

The PMT arrays are shown in Figure 3.4.6. The support frames consist of a flat titanium plate with supporting truss-work. The loads on this structure are substantial, particularly in the case of the lower array. For the submerged PMTs, the buoyancy force far exceeds the gravitational force: the net upward load is approximately 8 N per PMT, and collectively the total load for the bottom array is approximately 2,200 N. Many configurations of the support frame were considered and simulated using finite element analysis. Starting with a bare plate (no truss-work), a single 6 to 7-mm thick Ti plate deflected upward approximately 19 mm. Other options include successively thicker plates, double plates, curved plates, honeycomb reinforcement, and truss reinforcement. The truss reinforcement had the best overall performance when trying to limit deflection, minimize mass (and therefore background radiation), and provide a relatively open volume for scintillation light in the dome Skin to find its way to the Skin PMTs. The baseline lower PMT support frame

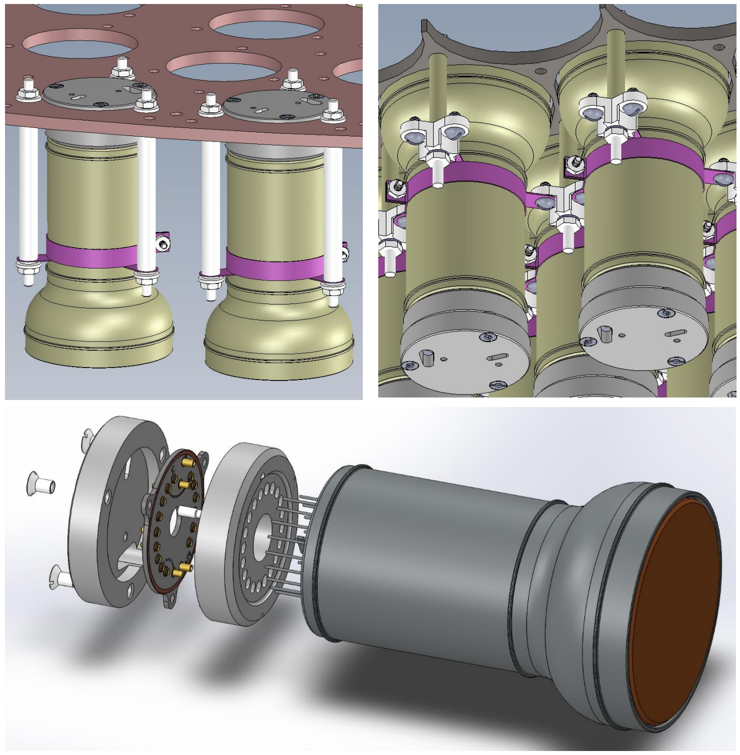

Figure 3.4.5: PMT assembly to the top and bottom array supports(upper right and left, respectively). The lower array PMTs are sleeved in PTFE and attached to the Ti plate with three PTFE rods. The lower panel shows the assembly to the base circuit, which is encased in PTFE caps; that at the back provides high reflectivity for the Skin detector and is used to strain-relive the cables.

is expected to deflect approximately 1 mm upward in operation. The upper PMT support frame (in the gas phase) will have a similar design, but the expected downward deflection is only ≈0.3 mm for that array.

The Ti surfaces surrounding the front faces of the PMTs, in both the top and bottom arrays, will be covered by PTFE pieces designed for photon recycling, and so increase photon detection efficiency in the main chamber, as discussed in Section 3.5. The pieces are designed to provide at least 95 % coverage of the Ti structural elements, while accommodating the differential thermal contraction coefficients of the PTFE and the Ti mount.

The lower LXe region, below the bottom PMT array, forms part of the Xe Skin detector in which the goal is to maintain over 50 % detection efficiency for ER events above 100 keV in more than 95 % of the Skin volume—see Section 3.7. The rear of the bottom PMTs, which project into this volume, are also sleeved in PTFE in order to increase photon recycling in the LXe below the array—this includes both a PTFE sleeve for the PMT body, and end-caps to cover the PMT bases. The PTFE base covers also prevent stray light leaking into the PMT envelope, and avoid pin short-circuits. The underside of the PMT mounting structure and braces will also be covered in PTFE reflectors where required, to increase the overall photon detection efficiency in the Skin region.

The PTFE components will be fabricated from material that has been pre-screened to achieve the intrinsic activity budget with respect to both gamma and neutron emission, as discussed in Chapter 9. During machining of the components and the assembly of the PMT arrays, the PTFE components will be maintained in purge boxes to reduce the plating of alpha emitters associated with airborne Rn, and ensure that additional (α,n) neutron generation is significantly below the intrinsic neutron emission goals.

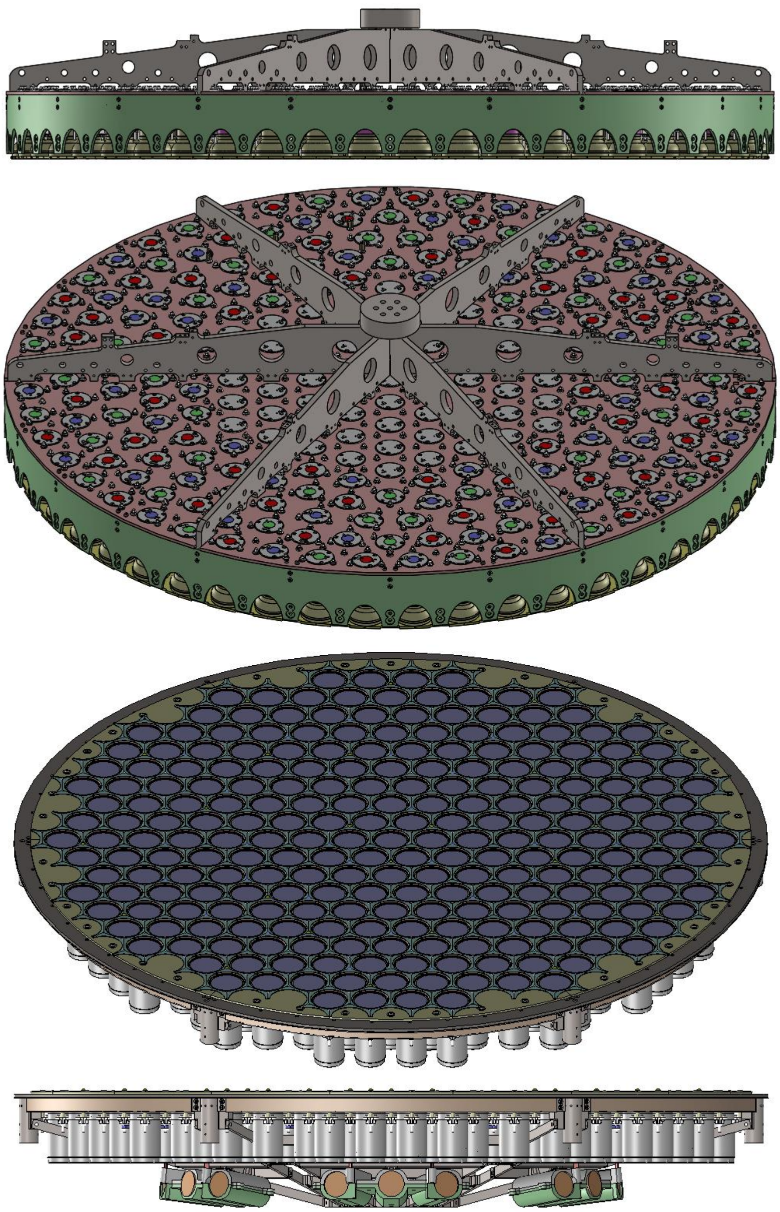

Figure 3.4.6: The bottom PMT array has 241 3-inch PMTs arranged in hexagonal configuration. The top PMT array accommodates 253 PMTs in a hexagonal-circular hybrid configuration.

PMTs passing all the testing and screening procedures will be installed onto their arrays inside a dedicated cleanroom at Brown University. Two PMT Array Lifting And Commissioning Enclosures (PALACE) will be built for this purpose. The arrays will be hanged vertically so that all PMT slots can be easily accessed during assembly. PALACE is also designed to be an airtight vessel so that the whole array and PMTs are under nitrogen purge when there is no assembly work on-going. With appropriate high voltage and signal feedthroughs, PALACE will also be used as dark chambers for final testing before TPC integration. Since each PALACE will hold the PMT array and over 240 PMTs, using PALACE as a radon emanation chamber will help understand the radon backgrounds in the detector; we are pursuing the goal of building PALACE as a radon emanation chamber with a target sensitivity of 0.3 mBq.

To meet these design goals, PALACE will consist of a stainless steel frame creating a $6 \times 6 \times 1.5\text{-foot}^3$ space to hold the PMT array. The nitrogen purge system will feed a 10 slpm flow from LN_2 boil-off into the chamber. All materials will be chosen so they emanate less than 0.1 mBq radon, and the vessel will be welded and electropolished to help achieve this. For the top lid a 1-inch thick plastic plate would be a sufficient radon barrier; we are investigating the best sealing technique for this purpose.

After PMTs are installed and the final electronics checkout is complete, PALACE is ready to be transported to SURF. The chambers will be sealed, purged and triple-bagged. During shipment PALACE will remain airtight, with the PMT arrays sitting in a nitrogen environment. Before the actual shipment happens test shipments with empty crates and accelerometers will be carried out to verify that PALACE is well taken care of under a medical equipment shipping company. After PALACE arrives at SURF it will be unwrapped and placed in the SURF cleanroom. PMTs will also be checked repeatedly to ensure their stability.

3.4.6 PMT Calibration

Three calibration techniques will be employed to monitor the PMT performance during LZ operation. The first one entails flashing 470 nm LEDs producing O(100) photons per pulse to measure after-pulsing, providing a direct indication of vacuum integrity of each tube. It is caused by residual gas ions inside the PMT body hitting the photocathode, creating a secondary signal appearing at a certain time after the main pulse. The after-pulse from Xe^+ ions would appear around 3 μs after the main pulse [20]. The second calibration is of the single photoelectron response, i.e. the absolute gain. The LEDs can be pulsed at a very low voltage such that signals seen by the PMTs come from single photons with high probability. The LZ LED calibration system is an evolution on the system developed for LUX. Calibration LEDs will be mounted on the face of each array to shine onto the PMTs opposite under individual DAQ control. A synchronized trigger is also fed into the DAQ system so the LED pulse timing is recorded along with the calibration data.

While the LED measurements monitor PMT gain (at 470 nm) and after-pulsing stability, the VUV response will be measured in-situ as the third calibration technique. In LUX this was achieved by extracting single photoelectron signals from tritium beta decay calibration data. The same calibration will be done in LZ (see Chapter 7). It was understood from LUX experience that when a PMT sees a 175 nm VUV photon, there is a $\approx$20 % probability that a second photoelectron is emitted in coincidence [21]. This double-photoelectron emission phenomenon has very important consequences—for understanding the optical performance of the detector, and on its energy resolution; therefore, it must be well characterized for all PMTs in operating conditions. The combination of the LED calibration, which produces the true single photoelectron response, with analysis of the response induced by xenon scintillation photons will allow us to obtain this information.

3.5 S1 Light Collection Design

3.5.1 Overview of Design and Optical Performance of the TPC

Achieving the highest possible collection of scintillation photons is a design priority: It leads to the lowest energy thresholds in the S1 and S2 channels and, by reducing statistical fluctuations in the S1 signal, it improves ER/NR discrimination. It also improves energy resolution, which is important for identifying gamma-ray background lines and for $0\nu\beta\beta$ sensitivity. The scintillation yields for electron and nuclear recoils depend on both energy and electric field. For reference, at the LZ field design goal 445 scintillation photons are expected to be emitted from a 10 keV ER track and 84 photons from a 10 keV NR interaction. The experimental challenge is to maximize how many are recorded as photoelectrons (phe) in the PMT arrays. In comparison, the high electroluminescence yield in saturated Xe vapor (typically $\approx$1,000 photons/cm per emitted electron [6]) leads to very large S2 signals such that single electrons are readily measured and sub-keV detection thresholds are obtained. The LXe scintillation emission is centered at 178 nm, with FWHM

= 14 nm [22]. Light from electroluminescence in Xe gas has a similar spectrum, but not quite identical [23]. Wavelength shifting is not required since the Xe luminescence spectrum is compatible with quartz-windowed photomultipliers. The basic optical properties of LXe are established: The refractive index for scintillation light is $n = 1.67$ [24], which is well matched to that of quartz ($n = 1.57$). This allows good optical coupling to the PMTs immersed in the liquid phase. The Rayleigh scattering length is 30 cm to 50 cm (see [23] and references therein), which must be considered in optical simulations.

The key issue is then to maximize the S1 photon-detection efficiency, α_1, defined as the number of detected photoelectrons per emitted scintillation photon from the event site. The main factors affecting α_1 in LZ are: (1) the VUV reflectivity of internal surfaces made from PTFE, especially those in the liquid; (2) the photon absorption length in the liquid bulk; (3) the geometric transparency and reflectivity of all grids; (4) the PMT photocathode coverage fraction; and (5) the PMT optical performance.

Most of these VUV optical properties have uncertainties that can result in significant differences in overall light collection. The factors affecting each of these properties are discussed in some detail below. In order to assess the detector performance we have adopted three sets of properties for light collection simulations which should bracket the final LZ response. The first is a realistic "baseline" set, which in most cases matches or only slightly exceeds the design requirements for individual optical parameters. The model which feeds into the estimation of the baseline LZ performance is slightly more conservative (≈10 % lower α_1) than this baseline optical model, to ensure that the baseline cross-section sensitivity is achieved with high probability. There is also a more optimistic (but still plausible) set of values which feed into the more ambitious sensitivity goal. Finally, for reference, there is a set of pessimistic values which are each somewhat unlikely, and highly unlikely to all occur together. These three sets of properties are listed in Table 3.5.1.

Table 3.5.1: Baseline as well as optimistic and pessimistic sets of optical properties considered for the LZ detector. The baseline LZ sensitivity is calculated using an optical model which is slightly more conservative than the optical baseline model (yielding a fiducial volume (FV) averaged α_1 of 7.5 %). The LZ sensitivity goal assumes the optimistic model.

Property	Pessimistic	Baseline	Optimistic
PTFE – in liquid	93 %	95 %	97 %
PTFE – in gas	75 %	80 %	85 %
Average PMT QE	22 %	25 %	28 %
Grid reflectivity (liquid and gas)	0 %	20 %	40 %
Absorption length in liquid	15 m	30 m	100 m
FV-averaged S1 PDE (α_1)	5.5 %	8.5 %	13.3 %

In Figure 3.5.1 we show the photon detection efficiency (PDE, or α_1) as a function of depth for the three sets of properties, and its partitioning into the top and bottom PMT arrays for the baseline properties. This is defined as the probability of a photon from the interaction site reaching a PMT and creating a photoelectron. The resulting S1 PDE averaged over a preliminary 5.6-tonne fiducial volume is also given in Table 3.5.1.

We effectively assume here that there is zero probability for single photons to create two photoelectrons. However, for the baseline we adopt an average PMT QE of 25 %; while typical QEs reported by the manufacturer for LXe scintillation are more like 30 %, this conservative QE matches the manufacturer specification—and it also allows for the 20 % fraction of double-photoelectron emission, not captured by the QE specification, that has been observed in these tubes for LXe scintillation [21]. Note that there will be an additional 92 % efficiency for triggering on single photoelectrons, as discussed in Chapter 8. This is applied for LZ performance estimates, but is not included here.

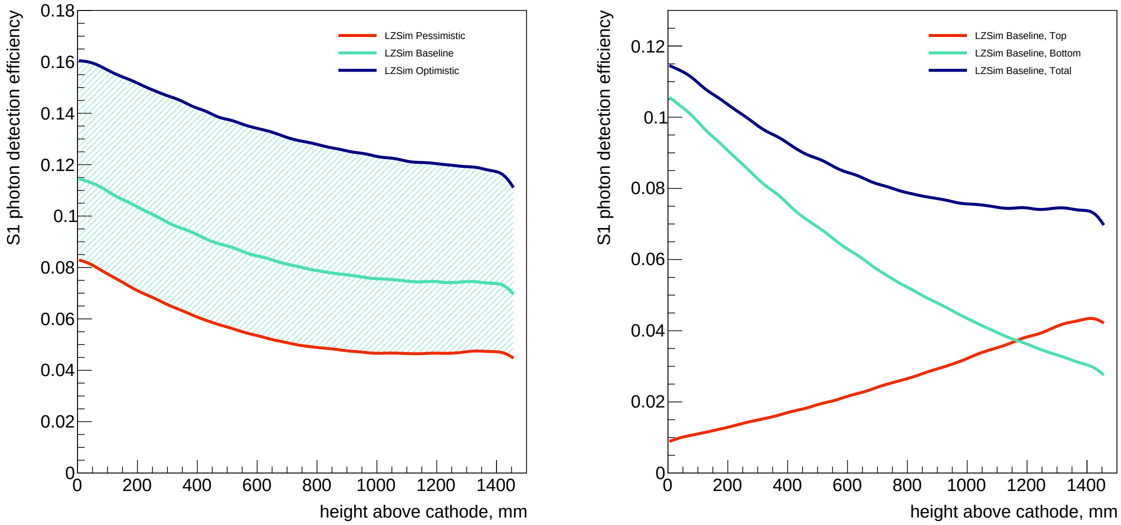

Figure 3.5.1: Left: Photon detection efficiency (α_1) versus interaction height above the cathode for the three optical scenarios listed in Table 3.5.1 (fiducial volume averages are also given in the table). Right: contributions from top and bottom arrays for the baseline optical model.

The baseline PDE of 8.5 % translates to an S1 response of 5.3 phe/keV at zero field for ^{57}Co γ-rays (a traditional measure of light yield in LXe chambers)—cf. 8.8 phe/keV in LUX [25], 6.6 in XENON10 [26, 27], 6.0 in PandaX-I [28], 5.0 in ZEPLIN-III [29], 4.3 in XENON100 [30], and 1.1 in ZEPLIN-II [31]. According to NEST, the corresponding NR energy threshold is ≈5.3 keV for a 3-phe coincidence requirement (while we adopt 5.8 keV for sensitivity estimates). Note that a lower, 2-fold coincidence may be possible (as in LUX) that would lower this threshold.

There are several basic features of the light collection response shown in Figure 3.5.1. The first, obvious from the figure, is that for most depths more light is collected in the bottom array that the top. This is due to the strong total internal reflection at the liquid surface due to the mismatch in refractive index, giving a critical angle for total internal reflection of 36°, and also the good match in VUV refractive indices between the quartz in the PMT windows and LXe. The second is the high degree of scattering from PFTE surfaces. This can be seen by considering the 8.5 % mean PDE (baseline scenario), which, with a 25 % PMT QE, implies a 34 % probability of a photon striking a photocathode, while the photocathode coverage is only ≈14 % of the total TPC internal surface. In the simulations the average number of scatters on PTFE is a depth dependent value between about 3 and 5. Thus, the value of PTFE reflectivity is quite important: the detector is effectively a "mirrored box" in which the value of light collection is the result of a competition between a photon being detected at a photocathode, and absorption that occurs with low probability but a high number of chances as the photon scatters around the detector. Finally, though not obvious in the figure, is that the mean path length traveled is a depth-dependent value between 3 and 5 m. Rayleigh scattering is also strong (with 30 cm length, the mean number of Rayleigh scatters is between 10 and 20), but does not significantly alter either the pattern or amount of light collection.

3.5.2 TPC Optical Properties

Here we discuss the reflectivity of PTFE in LXe, the absorption length in LXe, and the optical properties of the grids. The values shown in Table 3.5.1 are based on our best understanding, but, remarkably, they also happen to result in roughly equal loss of photons to absorption in the PTFE, LXe, and the grids. Somewhat modest gains (or losses) can be achieved by maximizing (or doing less well in) any one of these parameters, while the combined effect of improving (or doing worse in) all three could result in perhaps doubling (or near halving) of the overall light collection.

The photon absorption length in the bulk LXe depends on the purity of the liquid with respect to trace amounts of contaminants with absorption bands overlapping the LXe scintillation spectrum, mostly H_2O and O_2. For the tight purity requirements for those electronegative species (0.1 ppb, see Chapter 6), values in excess of 100 m can be expected (see Figure 15 in [23]). We have adopted a somewhat conservative 30 m baseline, along with 15 m and 100 m as pessimistic and optimistic values, respectively. The S1 PDE depth profile is shown in Figure 3.5.2 (left) for several values of this parameter. In the baseline and pessimistic scenarios, absorption is a comparable loss term to absorption on PTFE and grids, but becomes sub-dominant with the optimistic 100 m length and achieving even longer lengths gives diminishing benefit.

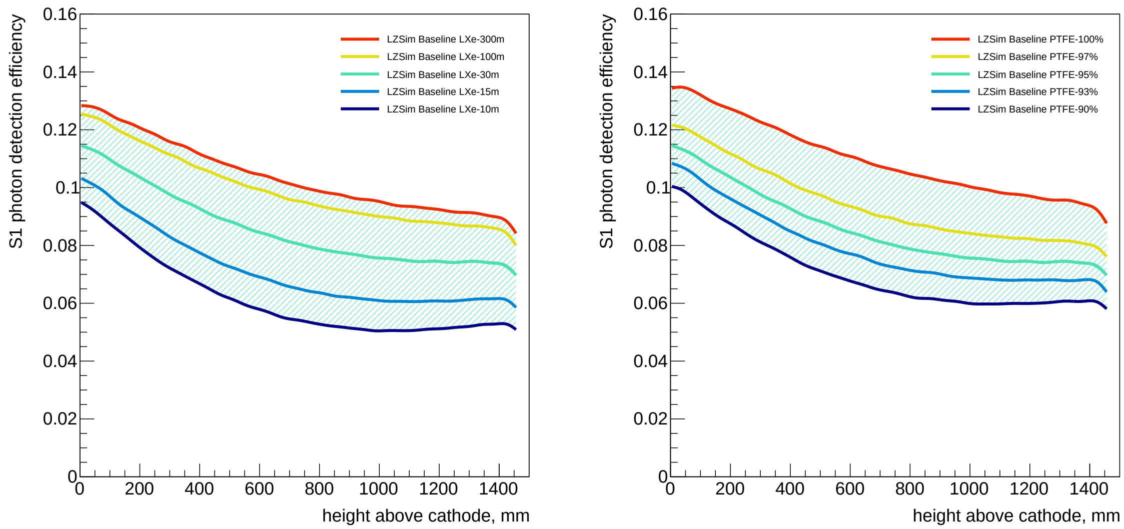

Figure 3.5.2: Left: S1 PDE (α_1) as a function of the photon absorption length in the liquid; Right: S1 PDE as a function of the PTFE/LXe interface reflectivity.

The four electrode grids in the LZ TPC all affect light collection through obscuration and wire reflectivity and, in a chamber where other sources of optical extinction have been minimized, these grids can have a significant effect on the light yield. The limited literature on reflectivity for metals at 178 nm indicates that very high values are unlikely, hence we have adopted values between 0 % and 40 %. This range is motivated by expectation that the specific surface treatment of the stainless steel grid material might have an effect on reflectivity, and that the final electropolishing step that we take in grid production could be beneficial. It is conceivable that a (conductive) reflective coating could be deployed (e.g., Al). The grid opacities shown (for normal incidence) in Table 3.6.3 are selected as a compromise between minimal opacity and minimizing the electric field at the wire surfaces, especially for the cathode and the gate grid, which is also cathodic. It is possible that the ongoing HV tests of grids (Section 3.10) may allow to deploy grids with higher geometrical transparency, which has a similar effect as increasing the reflectivity. Because light is partially trapped in the liquid phase by total internal reflection at the liquid surface, the grids in liquid have a relatively larger effect than the anode in the gas. This is fortunate, because considerations of generating uniform S2 light, discussed in Section 3.6, lead to the anode being the least transparent of the grids.

Perhaps the most important optical parameter is the reflector used in constructing the TPC. Based on a decade of experience, PTFE is indeed the best reflector for LXe scintillation, and also for properties other than optical: The manufacturing process yields very radiopure material (~1 ppt in U/Th); it has good mechanical properties (despite the 1.4 % to 1.5 % thermal contraction to LXe temperatures [9, 10]); and outgassing rates are relatively low. The reflectivity values we have adopted are based on optical simulations of the performance of LUX, similar analysis of other detectors, and recent results from small chamber measurements ongoing at LIP-Coimbra and recently starting up at Michigan. These test studies are discussed in Section 3.10. The effect of this parameter on the S1 PDE is shown in Figure 3.5.2 (right).

To reduce the dead volume around the active LXe, as well as outgassing and potential backgrounds, it is desirable to minimize the thickness of the PTFE walls of the TPC and Skin detectors. A lower limit is established by the transmittance of PTFE to Xe scintillation light, and the need for optical isolation between the TPC and Skin regions as well as between these and any dead regions containing LXe. The transmittance of the PTFE used in LUX was measured at LIP-Coimbra as a function of thickness and for different wavelengths: Xe gas scintillation (178 nm) as well as 255 nm, 340 nm and 470 nm. Results for Xe scintillation light show a transmittance <0.1 % for 1.5 mm PTFE thickness (but rising significantly to as much as 10 % for 5 mm in the case of 470 nm blue light). The TPC wall thickness in LZ is 15 mm, while the covering tiles of the vessel in the skin region is 1 mm and a similar though non-uniform thickness is used on the PMT arrays.

3.5.3 PMT Arrays

The two PMT arrays, shown in Figures 3.4.6 an 3.5.3, are similar, but not identical. Since most light is collected in the bottom array, it is a closed-packed hexagonal array of 241 PMTs, optimized purely for maximum photocathode coverage within the mechanical constraints of the low-mass structure that holds the PMTs. The mechanics of the array and PMT mounting are discussed in Section 3.4.5. In the bottom array the 76 mm diameter tubes are housed in 80 mm-diameter holes on an 82.5 mm center-to-center spacing, resulting in a 54 % coverage fraction of the 64 mm diameter photocathode surfaces. The spaces between the photocathode surfaces are fully covered with PTFE.

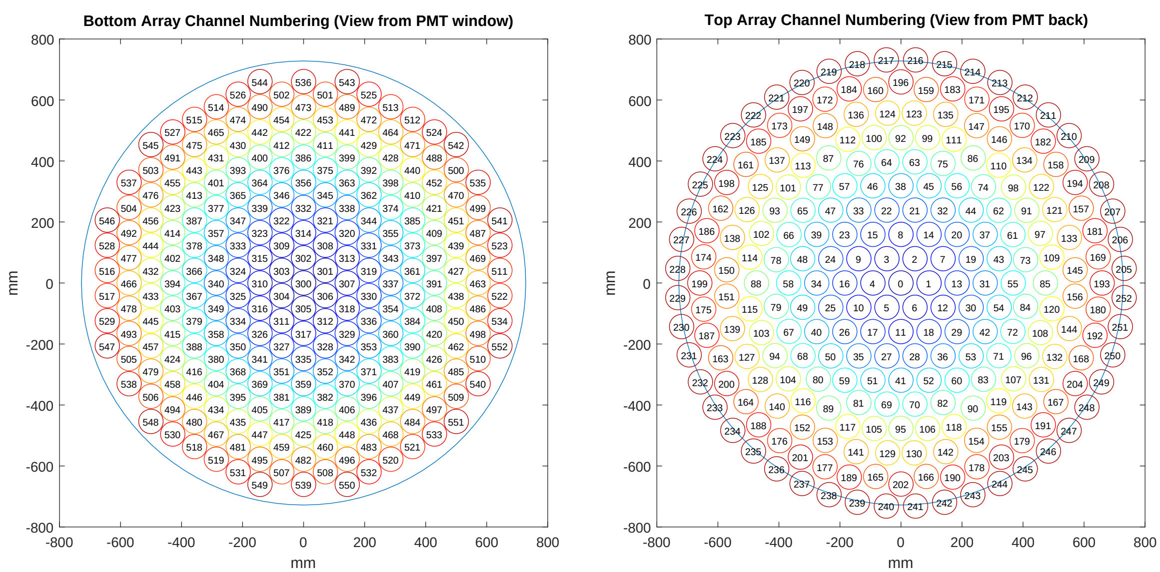

Figure 3.5.3: Layout of the bottom (left) and top (right) PMT arrays viewed from above. The channel numbering is done by radial position, with similar distances to the center indicated by color.

By contrast, while the top array collects a significant fraction of S1 light for events near the top of the detector, this array has the crucial role of reconstructing the x,y location of events from the S2 signal. Especially critical is the accuracy of reconstructing the position of “wall events” that result from interactions near the vertical cylindrical surface of the PTFE that defines the TPC. A particular concern is the population of decays from radon progeny plated out on the TPC walls. These consist of ER interactions from the beta decays and gamma-ray emission from the ^{210}Pb sub-chain, and from alpha particles and ≈100 keV ^{206}Pb nuclear recoils from the alpha decay of ^{210}Po. All of these, due to both energy and charge loss at the wall, lead to a broad distribution of low-energy signals that in part overlaps with the NR signal region in S2-S1 space. Therefore, it is critical to minimize the leakage of these events towards the center of the detector from errors in the reconstruction algorithm in order not to compromise the fiducial mass at low energy. Here the placement of the outer few PMT rows is critical. In contrast to the bottom array design, which is fully contained within the TPC diameter, the top array must overhang the edge of the TPC or all the reconstruction bias will point inward. Ideally, at least a full row of tubes would be located beyond the inner radius of the chamber. This is not possible due to the proximity of the inner cryostat vessel, and instead we locate the outermost circle of tubes at the largest-possible radius, which aligns the PMT centers above the TPC wall. From among a study of several layouts we adopted a "hybrid" array of 253 PMTs which has two nearly circular rows of PMTs at the perimeter but transitions to an hexagonal pattern in the center. The two outer circular rows maximize uniformity at the edge of the detector, which improves the uniformity of the x,y response near the wall and minimizes inward leakage. The larger overall diameter leads to the larger number of tubes, and the array is slightly less compact it the central hexagonal region, with a 93 mm center-to-center spacing (with the same 80 mm holes as the bottom array). We return to this optimization in Section 3.6.5.

3.6 S2 Production and Detection

Electrons escaping the interaction site are drifted under the influence of the "drift" electric field in the central part of the TPC to the electroluminescence region where they create the S2 signal. In this section we discuss the design of this region, including that of the electrode grids that create the drift and extraction/electroluminescence fields. The field cage that works in conjunction with the grids to generate the drift field is described in Section 3.2.

The electroluminescence region of the TPC is located at the top of the field cage, with the gate and anode electrodes (nominally 13 mm apart) straddling the liquid surface. The liquid level is controlled by a weir system at the edge of the TPC, as detailed in Section 3.8. This region controls the emission of the drifting electrons into the vapor phase and the subsequent production of electroluminescence photons, in proportion to the number of ionization electrons drifted away from the interaction site. This response channel readily provides sensitivity to single ionization electrons emitted from the liquid.

The S2 signal is also used for spatial localization of the interactions. In particular, the accurate reconstruction of "wall events" drives both the gain of the S2 response (involving the optimization of both photon production and collection efficiency) and of the layout of the top PMT array; this optimization is discussed below too.

Three main parameters characterize the S2 response: (1) the photoelectron yield, which depends itself on the cross-surface extraction probability for ionization electrons, the electroluminescence gain, and the efficiency of light collection for photons generated in the electroluminescence region (α_2); (2) the S2 pulse width, which is proportional to the electron transit time in the gas phase to first order; and (3) the resolution of the S2 signal, which depends on the detailed electric field distribution near the grid wires. Once the gate-anode separation is fixed (and therefore the gas gap L_g), these characteristics depend on operating parameters such as the xenon vapor pressure P and the voltage applied to those electrodes ΔV.

The S2 performance is affected by other electrostatic considerations (such as the maximum fields that can be sustained at the wire surfaces), and by mechanical considerations, such as the manufacture feasibility of large and densely-meshed wire grids, grid deflection and non-parallelism, etc. In the following sections we highlight the baseline design and the design goal, and describe how the S2 response depends on these operating conditions.

3.6.1 S2 Photon Production

For the smallest S2 signals, generated by one to a few ionization electrons, the main S2 requirements are: (1) definition of the single-electron response with a high signal-to-noise ratio, to allow absolute calibration of the ionization channel and to enable physics searches down to S2 signals as small as a few electrons; and (2) sufficiently large S2 signal for accurate reconstruction of the (x,y) location of peripheral interactions, such as those arising from contamination on the TPC walls. This motivates a photon yield of at least ≈50 photoelectrons per emitted electron, especially at the edge of the TPC. More details on how the S2 pulse size affects the reconstruction of wall events was given in LZ CDR [1]. Key parameters related to S2 photon production in LZ are presented in Table 3.6.1.

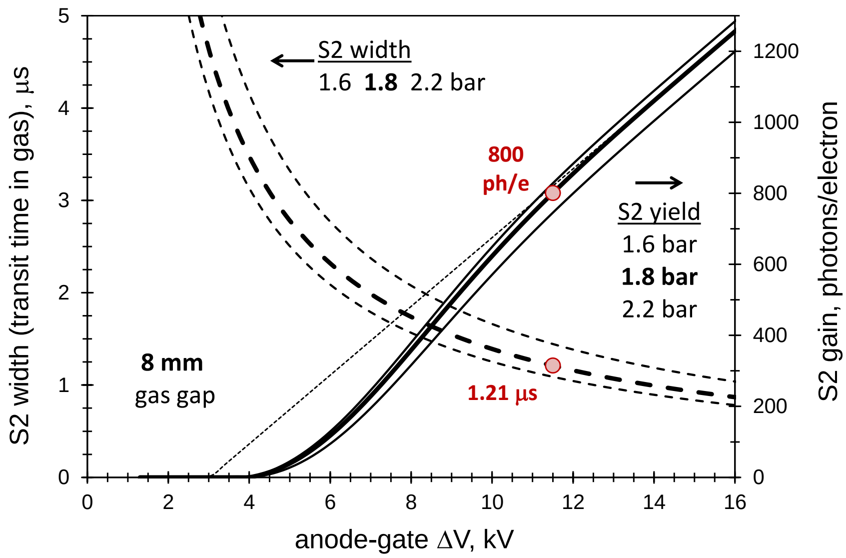

Figure 3.6.1: Dependence of the S2 photon yield and mean S2 pulse width (ignoring longitudinal diffusion in the liquid) on the voltage between anode and gate electrodes. The nominal photon yield [6], including the electron emission probability [5], and the electron transit time in the gas phase (S2 pulse width) [32], are indicated at the nominal ΔV=11.5 kV, for operating pressures around the 1.8 bar nominal and a gas gap of 8 mm).

Considering an S2 photon detection efficiency of ≈5 % for the top array for peripheral interactions, predicted by simulation as presented below, the above photoelectron yield implies a minimum of 800 photons generated per emitted electron. For a gate-anode distance of 13 mm with L_g=8 mm, this is achieved with ΔV=11.5 kV at the operating pressure P=1.8 bar, as shown in Figure 3.6.1. A voltage of +5.75 kV will be applied to the anode and −5.75 kV to the gate, leaving the liquid surface near −2.7 kV. Note, however, that the total gate-anode voltage is the real requirement, which gives the flexibility to trade-off between anode and gate voltages in case the nominal division becomes problematic (the anode sits in the gas phase, which is less resilient electrically and can give rise to spurious electroluminescence, but the gate is a cathodic electrode, and therefore susceptible to spurious electron emission).

All of these parameters are intimately connected to S2 light production: Both the electroluminescence yield and the electron drift velocity in the gas are determined by the reduced electric field in that region, E/P; in addition to the applied voltages, the electric field depends on both L and L_g. Therefore, these parameters must be studied together and their optimization is subtle. We described two viable configurations in the CDR and the one described here is intermediate between them in terms of gas gap and photon yield. The gas gap is sufficiently large to provide high gain, low variance of S2 photon production, and allowance for electrostatic deflection during operation (which will force the grids closer together at the detector center), but small enough to preserve the required dynamic range of the optical readout.

Table 3.6.1: Main S2-related parameters. The predicted S2 response is indicated for the parallel-field model assumed in Figure 3.6.1, as well as for the more detailed modeling illustrated in Figure 3.6.4. A nominal yield of 800 ph/e is used for sensitivity calculations (this includes a non-unity emission probability.

Parameter	value
Gate-Anode separation (and tolerance)	13.0 mm (±0.2 mm)
Gas gap (and tolerance)	8.0 mm (±0.2 mm)
Field in LXe (GXe)	5.2 kV/cm (10.2 kV/cm)
Electron emission probability	97.6 %
S2 photon yield	820 ph/e
S2 width FWHM	1.2 μs
Detailed modeling	
S2 photon yield	910 ph/e
S2 photon *rms*	2.0 %
S2 width FWHM	1.0 μs to 2.0 μs[a]

[a] The larger value is for diffusion-broadened S2 pulses from interactions near the cathode (see Figure 3.6.4).

Nonetheless, the choice of higher voltages across a longer gap has some disadvantages which must be mitigated. The electron emission probability at the liquid surface decreases rapidly when the field in the gas drops below 10 kV/cm [5]. In Figure 3.6.1, the S2 yield assuming full extraction efficiency is represented by the dotted line, while the continuous lines include the field-dependent extraction probability. For our nominal parameters, that probability is close to unity, but poor extraction efficiency may result if nominal voltages fail to be achieved. We mitigate this with Phase-II of our System Test program described in Section 3.10.4—this includes testing the final gate-anode assembly to ensure that the design voltages can be realized.

Longer electron transit times in the gas also hide the effect of electron diffusion in the liquid, which encodes (modest) interaction-depth information on the S2 pulse shape. This information allows some coarse fiducialization, which is important for an "S2-only" analysis. The mean S2 pulse width is 1.2 μs, which will make the precise measurement of diffusion-broadening of the S2 response more difficult. If required, this may be mitigated with operation at lower drift field (see Table 3.3.1).

3.6.2 S2 Photon Detection

The LZSim model was used to obtain the baseline photon detection efficiency for the S2 response (α_2), representing the fraction of photons which are detected by the PMT arrays. This parameter multiplies the photon yield per electron discussed in Section 3.6.2 and the number of ionization electrons drifted away from the interaction site to yield the total S2 response (assuming no loss to electronegative impurities). The dependence of α_2 on radius is shown in Figure 3.6.2 and values for central and peripheral locations are summarized in Table 3.6.2.

The optical parameters are as assumed for the α_1 simulation described in Section 3.5.2. In this instance, the top array makes the largest contribution to α_2 as expected, partly due to the optical mismatch between

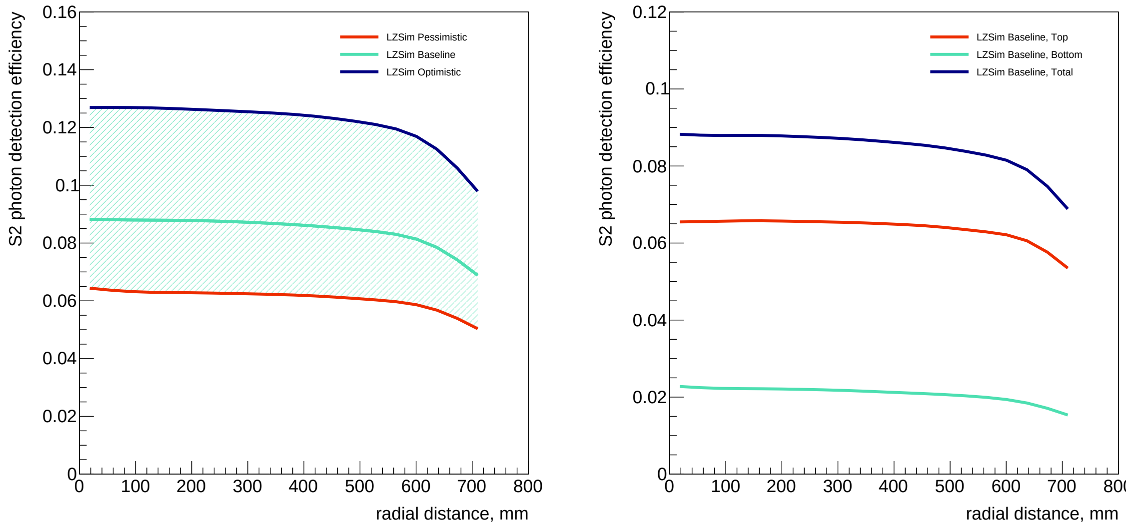

Figure 3.6.2: Left: Radial dependence of S2 photon detection efficiency for several scenarios; the nominal optical model averages α_2=12.0 % and is used to calculate the LZ baseline performance; Right: Contributions from top and bottom arrays for baseline optical model.

the gas and liquid phases. Other driving parameters are the anode transparency and the reflectivity of PTFE in the gas phase (trefoil structures surrounding the PMT windows).

Table 3.6.2: S2 photon detection efficiency (α_2) and photoelectron yield for single electron signals (in brackets, assuming 800 ph/e) for central and TPC-wall interactions.

PMT array	Center	Edge
Top	6.6 % (52 phe/e)	5.4 % (43 phe)
Bottom	2.2 % (18 phe/e)	1.5 % (12 phe)
Top+Bottom	8.8 % (70 phe/e)	6.9 % (55 phe)

Towards the center of the TPC α_2 exceeds 8 %, decreasing to below 7 % for wall events, which enables a single electron response comfortably above 50 phe/e everywhere in the detector. For wall events the top array detects some 40 phe/e, which is sufficient for the effective reconstruction of plateout backgrounds as discussed later in this section.

The bottom array converts just over 2 % of the S2 photons, with each PMT contributing a fairly constant 0.01 % to the overall detection efficiency in that array. This allows LZ to reconstruct large S2 pulses which will saturate many channels in the top array, where an individual PMT located just above the S2 vertex can convert 2 % of the S2 photons—as much as the whole of the bottom array.

Using instead the optimistic optical parameters presented in Section 3.5.2—which bring the baseline α_1 from 8.5 % to 13.3 %—the effect on α_2 is comparable: the baseline S2 detection efficiency increases from 8.8 % to 12.7 % for central interactions, with roughly equal gains in both arrays in absolute terms.

3.6.3 S2 Resolution and Electrode Configuration

In addition to appropriate S2 gain and pulse width, we must ensure that the overall energy resolution of the TPC is good. At low recoils energies (ER and NR) this is dominated by statistical fluctuations on the small number of detected S1 and S2 quanta (including significant recombination fluctuations) and the quality of the S2 design is unlikely to be a dominant factor for WIMP searches. However, for MeV electron-recoil energies, instrumental effects eventually dominate the overall resolution since a combined energy scale using both S1 and S2 can eliminate the recombination fluctuations, and the number of S1 and S2 quanta is large.

This demands a low dispersion of photon production from the electroluminescence region, which in turn drives the detailed design of the gate and especially the anode grids. This is intimately related to the characterization of detector backgrounds, in particular enabling high-quality spectroscopy of radioactivity gamma-rays generating up to $\sim 10^5$ electrons—see Figure 3.6.3. These are important to understand low-energy, external ER backgrounds, but especially to constrain radioactivity neutrons. Clearly, fine energy resolution is also required if LZ is to attempt the detection of $0\nu\beta\beta$-decay in ^{136}Xe. We quantify our resolution requirement at the respective Q-value of 2,458 keV, and we designed to achieve 2 % in the combined energy scale (1.5 % goal).

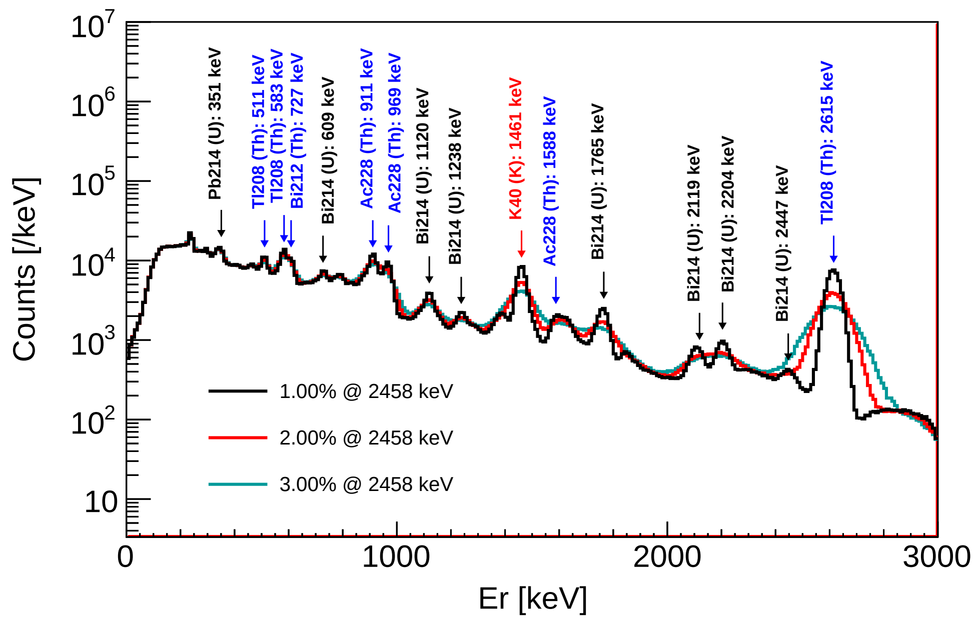

Figure 3.6.3: Energy-resolution for high energy electron recoils (S1-S2 combined energy scale). Spectrum is simulated ER background from the titanium cryostat in the full active volume in 1,000 days.

Therefore, fluctuations related to S2 photon production and detection must remain small, at ∼1 % level. This motivated a detailed study of electroluminescence and electrode grid configuration presented in the LZ CDR, and subsequently the selection of the electrode grids listed in Table 3.6.3. Other factors contributing to the S2 resolution are the uniformity of response in the horizontal plane over the whole TPC diameter (e.g., wire sagging and electrostatic deflection), although those can be calibrated and hence removed to first order.

Aside from diffusion (in both gas and liquid phases), drifting electrons follow electric field lines and therefore their length and the field strength close to the wires must be carefully controlled to avoid substantial dispersion or even the possibility of significant charge multiplication (the first Townsend coefficient for cold Xe vapor at the 1.8 bar operating pressure reaches 1 e/mm at 35 kV/cm [32, 33]). Two additional concerns, which are intimately related, are the ability of the electrodes to hold HV and their VUV reflectivity, which depend strongly on the wire material and surface properties; we have investigated these issues through the dedicated R&D activities described in Section 3.10.2.

Table 3.6.3: TPC electrode grid parameters (all 90° woven meshes). Surface fields are wire-average for −100 kV cathode voltage. The geometric opacity is given at normal incidence.

Electrode	Voltage	Wire diameter/pitch	Number	Wire field	Opacity
Anode	+5.5 kV	100 µm / 2.5 mm	1,184	+55 kV/cm	8.0 %
Gate	−5.5 kV	75 µm / 5.0 mm	592	−62 kV/cm	3.0 %
Cathode	−50 kV	100 µm / 5.0 mm	592	−31 kV/cm	4.0 %
Bottom	−1.5 kV	75 µm / 5.0 mm	592	+34 kV/cm	3.0 %

The optimization of the anode geometry involves a compromise between optical, electrostatic, mechanical, and electroluminescence properties. The latter were assessed through full electron transport modeling, in particular examining the S2 photon production statistics from single electron drifts in the gas phase of several candidate geometries. This method has been validated by comparison of simulated and actual signals in the LUX detector [34]. Subsequently we applied this methodology to the baseline gate-anode electrode configuration, and some results are shown in Figure 3.6.4. This involved the detailed modeling of electrostatic fields in the electroluminescence region using the Elmer solver [35] and the meshing tool Gmsh [36], followed by simulation of electron transport and photon production with Garfield++ [37] using xenon transport parameters from Magboltz [33].

As discussed below, all of the grids are woven meshes. Increasing the density (smaller pitch and/or larger diameter wires) decreases the electric field near the wire surfaces, reducing spurious electron emission from the gate and charge multiplication near the anode. It also provides more uniform field lines, especially near the anode, which is important for reducing dispersion of the produced S2 signal. However, decreasing the opacity increases α_1 and α_2, and increases the ease of manufacture. The gate pitch is half that of the anode pitch, and the two grids are aligned such that an anode wire crossing sits directly above the center of each open square in the gate grid. As the electrons pass through the gate they are focused towards the center of each square, and hence towards this crossing. This alignment gives smallest spread in path lengths traversed from the liquid to the anode, and hence smallest dispersion in the generated S2 signal.

Details of the simulated performance of the baseline gate-anode design are shown in Figure 3.6.4. This study assumes that electrons start evenly spread in (x,y) below the gate grid. The S2 signal resolution and the timing performance are those reported in Table 3.6.1 above. Without diffusion the pulse would have a "box" shape if the anode were a plane; the spike at the end of the pulse (shown in d) is from electrons moving through the short region of enhanced field near the anode wires. The predicted photon yield is slightly higher than suggested by the parallel-plate calculation presented in Figure 3.6.1 for this reason. Conversely, some electrons move near the center of the unit cell, experiencing lower average fields, and this motivates the occasional lower yield visible in panel c) of the same figure. Those electrons also arrive slightly later, and form the tail above 1 µs shown in d). Sparser grids aggravate both of these effects very quickly.

3.6.4 Design and Fabrication of the Grids

The four grids, whose basic parameters are list in Table 3.6.3, are all of a crossed mesh design. They are fabricated by weaving and individually tensioning a set of series 300 stainless steel wires, and held by a set of low mass grid stainless steel rings housed within the field cage. The crossed mesh design has several benefits. Compared to a parallel set of wires, it presents a more uniform load on the ring, allowing it to be smaller in mass. The crossed wire mesh is also more mechanically robust than free-standing wires, and the fields are more uniform. Note that electroformed grids are not readily available at the size of LZ, and also

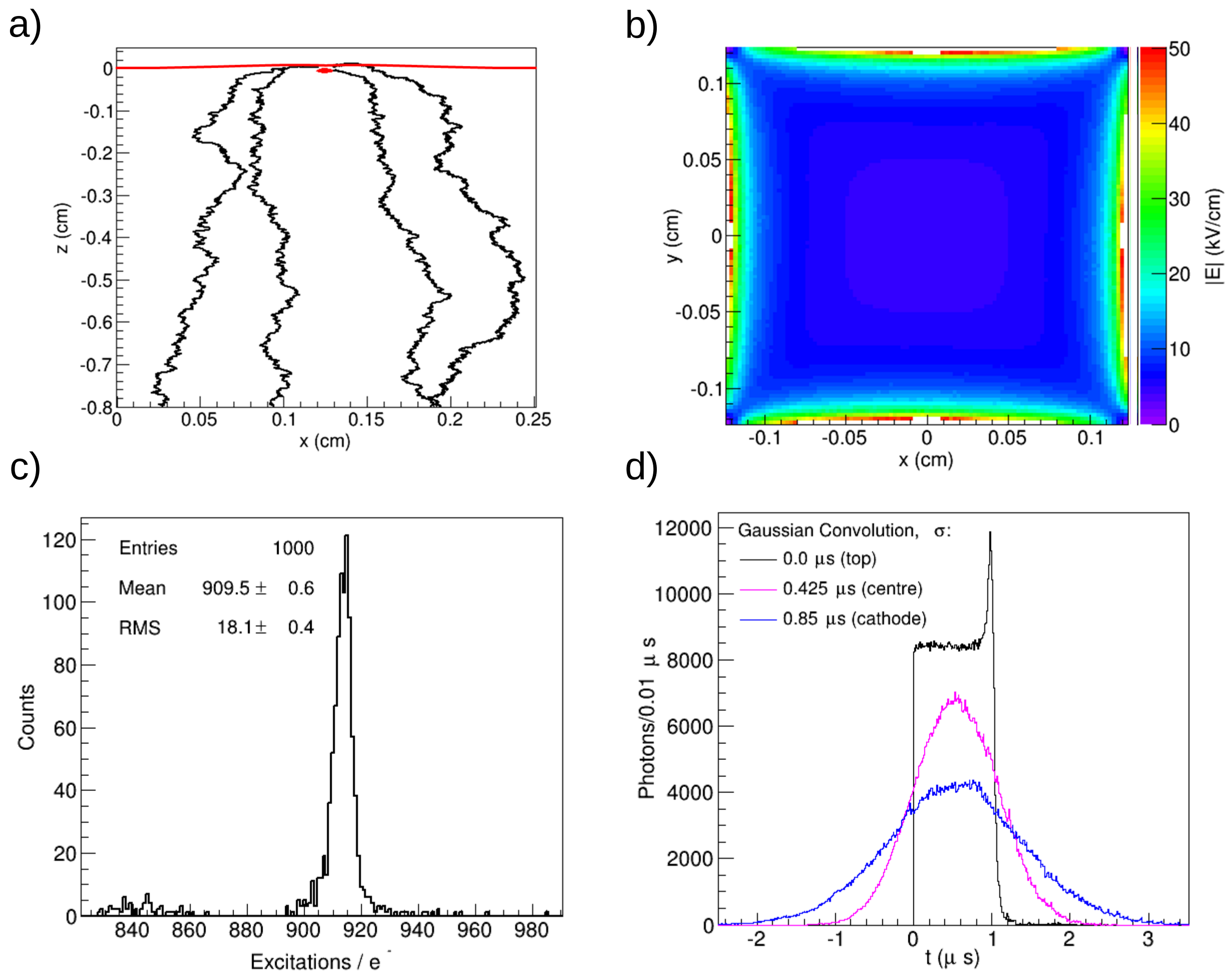

Figure 3.6.4: Simulated S2 electroluminescence response of 1,000 electrons for the baseline gate-anode design [34]. a) Examples of electron drifts from the liquid surface (at $z=-0.8$ cm) until their collection at the anode mesh wires (shown in red); b) Electrostatic field strength through the anode plane; c) Photon yield (number of excitations), confirming 2 % *rms* for electrons distributed evenly in the liquid xenon bulk; d) S2 simulated pulse shape of the electron signal, without longitudinal electron diffusion in the liquid (black), and the same distribution convolved with the amount of Gaussian diffusion expected for drift from the center (magenta) and bottom of the detector (blue).

do not naturally have the minimum-surface field producing the profile of a round wire. The wires are chosen to have the highest available surface smoothness.

Large, attractive electrostatic forces exist between the gate and anode grids because of the strong electroluminescence field and, to a lesser extent, between the cathode and bottom grids due to the high field in the reverse field region. The tension on the wires in these grids, nominally 0.25 kg on the anode and 0.5 kg on the others, should achieve less than 2 mm combined maximum deflection between the gate and anode, when the grids are treated as individual wires. These loads are well within the yield strength of available stainless steel wires, but nonetheless represents an important mechanical requirement on the assembly. Evaluation of the mesh grid is much more difficult, though approximate treatments may be possible. We expect that the resulting deflection will be smaller than that estimated from the individual wire calculation, possibly allowing a reduction in tension. The actual tension in full-size prototype grids will be directly measured under field. Note the tension needed to minimize this overall deflection is larger than the minimum tension needed to prevent the well-known wire-to-wire "saw-tooth" instability encountered in a single plane of wires in a wire chamber.

The technique for weaving the wires is analogous to the process used in the textile industry for making woven cloth with a loom. Initially, the wire forces are supported by the loom. The technique for anchoring the grid wires is to capture them between two support rings that are epoxied together. The epoxy locks the grid wires in the space between the support rings. Once the epoxy is fully cured, grid wires outside the support rings are trimmed off, and the wire load is solely carried by the rings. The process for making all the grids is the same as the cathode, albeit with different diameter wires and spacings. After production, the entire grid assemblies will be electropolished and passivated chemically to achieve the highest possible surface quality. Such a treatment has been shown to be beneficial on single wire samples as described in Section 3.10.2. We have demonstrated the technique of electropolishing completed grids for the Phase-I System Test TPC prototype which is described in Section 3.10.3.

3.6.5 Reconstruction of Peripheral Interactions

The mis-reconstruction to smaller radii of peripheral background events—such as those arising from radon progeny plateout on the inner field cage walls—can be a leading source of background in double-phase xenon TPCs (e.g. ZEPLIN-II [31] and LUX [25] were so affected). This must be addressed by both lowering plateout rates and ensuring good quality spatial reconstruction for the remaining decays. The layout of the top PMT array, and in particular of the peripheral tubes, is therefore of great importance. We considered five array configurations in our initial optimization and this was discussed in the LZ CDR (Section 6.5.3 in Ref. [1]). An additional study was carried out to optimize the hybrid configuration selected previously, based on further considerations including electric field between PMTs, S2 light collection uniformity, and mechanical feasibility.

Based on this new study we adopted for the top array a circular/hexagonal hybrid layout containing 253 PMTs, transitioning from a close-packed hexagonal core to a 48-unit circular outer row (see Figure 3.5.3). The minimum PMT separation is 86.3 mm. Our methodology involved extensive optical Monte Carlo using the code ANTS2 [38] coupled to the Mercury vertex reconstruction algorithm [39]. This provided a realistic assessment of the position resolution of the chamber for small S2 signals and, in particular, the fraction of peripheral events that is misreconstructed into the TPC volume. This "leakage" fraction was the main design criterion used to select the best array configuration. In addition to the position of the outer PMTs, two other design parameters influence the peripheral position resolution: the distance between the anode grid and the PMT windows, and the reflectivity of the lateral wall in the gas. Regarding the latter issue, a low-reflectance material is desirable so as not to overly distort the spatial response of the outer PMTs. Titanium has 16 % reflectance at 178 nm, but its oxides can be more reflective in the VUV [40], and a non-conducting material is preferred to minimize fields. Thus, that region will be covered by Kapton™ foil instead.

Figure 3.6.5 summarizes the results from a high-statistics study of the leakage past various reconstructed radii, with 40-mm being the nominal distance to our preliminary 5.6-tonne fiducial volume. This leakage is indicated as a function of S2 signal size (with 4,000 S2 photons corresponding to about 5 emitted electrons). This confirms that we can achieve a very small leakage into the fiducial volume above the nominal S2 threshold.

It should be noted that the ionization removed from wall interactions tends to be pushed into the TPC as it drifts and ends up being emitted up to several centimeters away from the TPC edge (as shown in Fig. 3.2.2), which will help mitigate this background. We do not take this field distortion into account in this calculation.

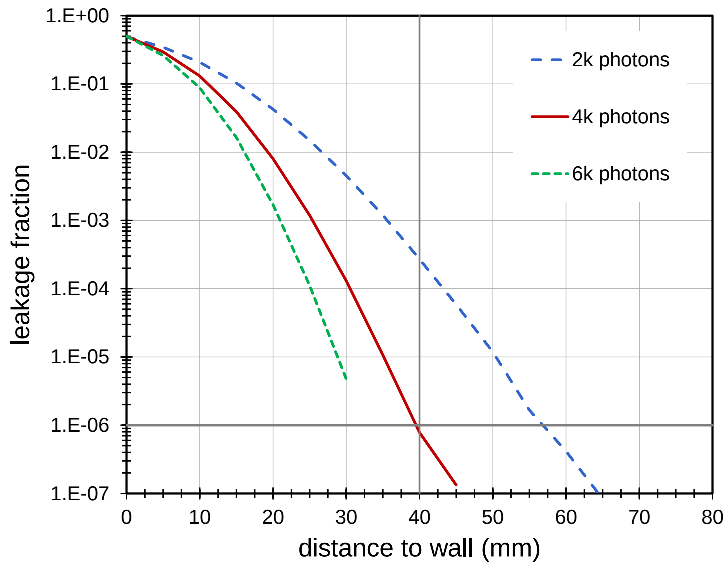

Figure 3.6.5: Simulated reconstruction of wall events as a function of signal size. For 4,000-photon S2 signals (≈5 electrons emitted) a leakage of 10^{-6} is achievable at the edge of our preliminary fiducial volume which is located at 40 mm from the wall.

3.7 The Xe Skin Detector

The region between the outer walls of the TPC and the inner cryostat vessel is called the "Xe Skin". This region provides necessary mechanical clearance to allow for detector assembly, houses instrumentation including PMTs and other sensors, and provides a standoff between biased TPC components and the electrically-grounded inner vessel. The Xe Skin contains more than 2 tonnes of LXe, and it is divided into two primary functional regions: a cylindrical, "side Skin" region outside of the main TPC field rings, and a "dome Skin" region underneath the TPC.

Because of the high density of LXe, gamma rays (and, to a lesser extent, neutrons) have a high probability of interacting or being absorbed in the Skin region. This poses a problem for the efficiency of the outer LS veto detector, a key element in reducing backgrounds in LZ, as secondary scatters that would otherwise be tagged in the Outer Detector are lost in the Skin. Additionally, for events that deposit energy in both the main TPC and the Xe Skin, leakage of light from the Skin to the TPC can compromise the rejection of the dominant ER background by increasing the observed S1 signal and lowering the S2/S1 ratio used for particle discrimination. To counter these effects, we instrument the Xe Skin region with 93 dedicated 1-inch R8520 PMTs in the top half of the side Skin, 20 2-inch R8778 PMTs in bottom half of the side skin, and 18 more 2-inch R8778 PMTs in the dome, turning the Xe Skin into a second component of the LZ veto strategy to clearly identify events with scattering vertices in the Skin. Instrumenting the Xe Skin also increases the amount of information available about the background environment of the WIMP target, improving the background model and the efficiency of the data analysis. The goal for the Xe Skin detector design is to achieve an energy threshold for observing ER scatters produced by gamma-ray backgrounds or radiative neutron capture on detector materials of 100 $\mathrm{keV_{ee}}$ in over 95 % of the volume of the Xe Skin. A second goal is to minimize light leakage between the Xe Skin and the TPC. These are related goals: Since optical isolation is never perfectly realized, any scintillation emitted in "S2-inactive" regions of the detector must be read out to prevent the dangerous background topologies described above.

The side Skin is 4 cm wide near the top of the TPC, increasing to 8 cm in the lower half due to the tapered vessel shape. This region is instrumented with 93 1-inch R8520 PMTs viewing down located just below the LXe surface and a further 20 2-inch R8778 PMTs looking up. 18 of the R8778 tubes are arranged symmetrically around the bottom of the TPC, with 2 extra PMTs looking specifically at the region where the cathode HV feedthrough enters the detector. Light emission from surfaces is often the first sign of issues maintaining high voltage, and photons produced near the cathode region, whether from radioactivity or from voltage breakdown, have a high probability of entering the feedthrough umbilical and being absorbed. The additional PMTs increase the photocathode coverage in the area to mitigate such photon losses.

The Skin PMTs mount to the weir system as shown in Figure 3.1.1 on page 56, and to the bottom array as depicted in Figure 3.7.1. The inside surface of the inner cryostat vessel is lined with thin PTFE sheets for improved light collection, and the outer surface of the TPC walls also provides a PTFE reflector. The top side Skin region uses 1-inch PMTs, rather than the larger model in the TPC due to mechanical constraints. The Hamamatsu R8520 is specifically designed for LXe operation and was the primary PMT used, for example, in the XENON10 and XENON100 detectors [26, 30]. The R8520 is a compact 1-inch, square PMT with quartz window and bialkali photocathode with a typical QE of 30 % at 175 nm. A gain of 10^6 is provided by an 11-stage metal channel dynode chain. We use a smaller number of 2-inch R8778 tubes in the bottom side skin and in the dome also for mechanical constraints, as R11410 PMTs would not fit in either region. The R8778 PMTs will be recovered from the LUX experiment, where they have operated for several years in a low-background, LXe environment and have been well characterized.

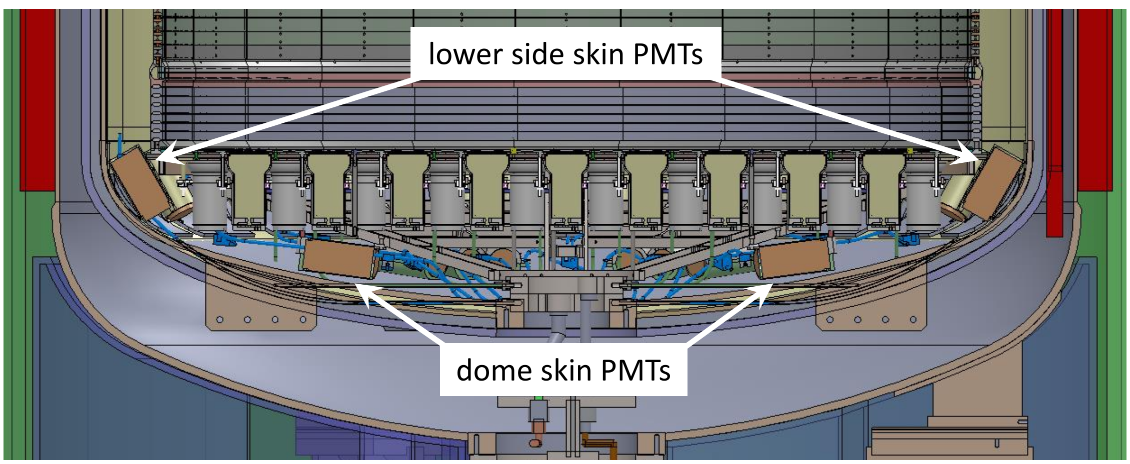

Figure 3.7.1: Mounting of the Skin PMTs in the dome and lower side regions. The upper Skin PMTs mount to the weir system as shown in Figure 3.1.1.

Similar to the inside surface of the TPC, PTFE will be used to cover the underside of the TPC PMT support structure facing the Skin. Both the main TPC PMTs and the R8778 PMTs will have reflective PTFE sleeves to reduce photon absorption on their metal envelopes. The dome Skin PMTs will be mounted to to the lower truss of the TPC structure as depicted in Figure 3.7.1.

3.7.1 Skin performance

Design studies for this region begin by assessing the combined Xe Skin and Outer Detector veto performance as a function of threshold in the Skin. As described in Chapter 12, a comprehensive model of the LZ detector is implemented in GEANT4, and the effect of radioactivity in various detector components is simulated. The key performance metric of the combined anti-coincidence system is the veto inefficiency, defined as the number of unvetoed single scatter events in a detector divided by the total number of single scatters in that volume. This inefficiency varies with threshold in both veto regions. Figure 3.7.2 shows the veto inefficiency for single scatters caused by gamma-rays as a function of Skin threshold, showing a 50 % increase as the threshold varies from 100 $\mathrm{keV_{ee}}$ to 200 $\mathrm{keV_{ee}}$. In other words, the un-rejected background rate increases by that factor as the Skin threshold is increased. The requirement that the number of electron recoil events produced by detector materials be less than 10 % of the predicted rate of neutrino-electron scatters therefore drives the requirement that the energy threshold in the Skin must be 100 $\mathrm{keV_{ee}}$. As the light collection efficiency in the Xe Skin is very non-uniform (comparing, for example, the side and dome regions), we include in the requirement the demand that 95 % of the volume in the Skin meets the 100 $\mathrm{keV_{ee}}$ threshold target.

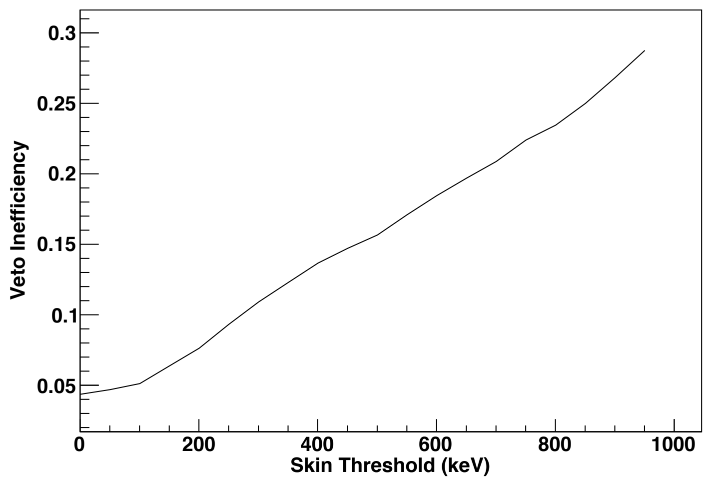

Figure 3.7.2: Skin veto inefficiency for gamma backgrounds, defined as the number of unvetoed single-scatter events divided by the total number of single-scatter events as a function of energy threshold in the Xe Skin. The inefficiency increases from 5.1 % to 7.6 % as the threshold rises from 100 $\mathrm{keV_{ee}}$ to 200 $\mathrm{keV_{ee}}$, representing a 50 % increase in gamma backgrounds from internal radioactivity. The background requirements for LZ demand that an energy threshold of 100 $\mathrm{keV_{ee}}$ be achieved in over 95 % of the Xe Skin volume.

The next step of the design is to create an optical model for the Skin to understand how much photocathode coverage and surface reflectivity are needed. We use the same simulation geometry developed for the background studies, taking care to define the optical interfaces to understand the effect of surface reflectivity. We first divide the Xe Skin into 1 cm × 1 cm × 1 cm pixels. The electric field in each pixel is calculated from an electrostatic model, and we use the NEST package to find the mean number of photons produced by a 100 keV electron recoil in each pixel, accounting for suppression in scintillation yield caused by the high electric field. Photons are then generated in each pixel and propagated through the optical model, and the photon collection efficiency (PDE) is defined as the number of observed photoelectrons per generated photon, including PMT effects such as quantum efficiency (as for the TPC). Finally, a pixel is deemed "good" if the PDE is high enough that 50 % of 100 $\mathrm{keV_{ee}}$ events produce at least 3 detected photoelectrons. Figure 3.7.3 shows the PDE in the Skin as a function of position (averaged over azimuth) for the design described here. Over 97 % of the Skin region achieves an energy threshold of 100 $\mathrm{keV_{ee}}$, meeting the requirement.

The Skin PDE is highly dependent on the wall reflectivity, especially in the side Skin, and the left panel of Figure 3.7.4 shows how this parameter varies as a function of z in the side Skin for different reflectivity assumptions. Given the strong dependence, we set a requirement on the PTFE reflectivity of the cryostat liner of 95 %, the same as for the TPC walls. The final model described above assumes that only 98 % of the

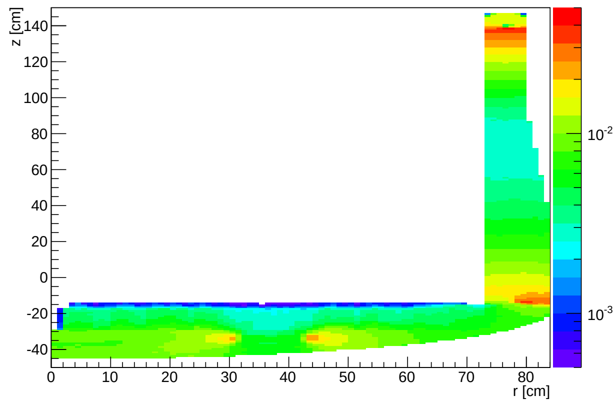

Figure 3.7.3: Photon detection efficiency (PDE) in the Skin region as a function of position (averaged over the azimuth) for the design described in the text. Over 97 % of the Skin region achieves an energy threshold of 100 $\mathrm{keV_{ee}}$, meeting the requirement.

wall is covered, allowing for joints or other imperfections in the liner. The threshold requirements are met in the dome region without any additional PTFE beyond that covering the PMTs.

The PTFE liner will be supported by metal "buttons" that are bonded to the cryostat walls using cryogenic epoxy. Simulations of the field in the skin show that metal buttons can be used without causing excessive surface fields, even near the cathode ring. A schematic showing how the buttons will hold PTFE tiles in place can be seen in the right panel of Figure 3.7.4. Holes will be cut into the liner to go around the buttons, and PTFE screws will hold PTFE washers above the liner, capturing it in place.

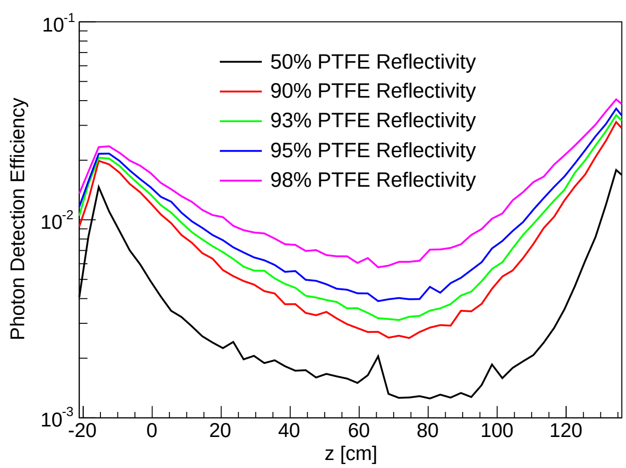

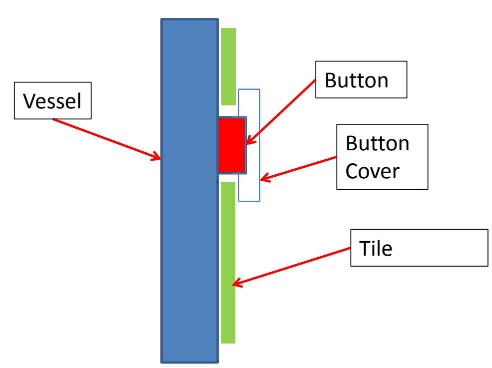

Figure 3.7.4: Left: Photon detection efficiency as a function of z in the side Skin region for different values of PTFE reflectivity (in percent), where the inner wall of the cryostat is lined with PTFE and the outer wall of the TPC is made of PTFE. The LZ requirement is 95 % reflectivity for the PTFE/LXe interface. Right: A schematic showing how buttons bonded to the cryostat wall will hold PTFE tiles in place to line the cryostat with reflective material.

3.8 Internal Fluid System

Efficient purification of LXe is a significant challenge, and is especially important given the large size of LZ and the resultant long electron drift lengths and long photon path lengths involved. Purification is discussed in detail in Chapter 6, and the overall internal flow diagram is shown schematically in Figure 3.8.1. Liquid in the detector is continuously circulated to a purification tower located outside of the water tank, where it is evaporated in a two-phase heat exchanger and passed to a gas purification system. There, it is purified by a commercial heated getter. While the getter is highly efficient in a single pass, continuous purification has proved necessary in most previous such detectors, primarily because of the large amount of PTFE and other plastics especially in cables that serve as a long-term source of outgassing. After passing through the getter, the Xe returns to the liquid tower, where it is recondensed in the two-phase heat exchanger, degassed and subcooled, and then passed back to the detector. In addition, separate gas flow through the external purification system purges the space above the liquid, and the conduits. The overall flow rate is 500 slpm of gas, which is 16 cm^3/s of liquid flow, 2.8 kg/min, and fully processes 10 tonnes of Xe in 2.5 d.

While much of the functionality and complexity of the system shown in Figure 6.4.1 is external to the detector and is described in Chapter 6, the "internal circulation system" that resides within the detector has important design considerations too. Primarily, the system must purify the liquid while sweeping all regions of LXe to avoid stagnant fluid, which is especially important when using the dissolved tritium calibration source. It must do this while maintaining a stable liquid surface with no boiling throughout the volume, and allowing operation within the 1.6 bar to 2.2 bar (a) pressure range. Along with the cryogenics system, it provides cooling to counter the various heat loads in the system. Finally, it should allow, to the extent possible, operation in two modes: one where the liquid is convectively mixed on a time scale that is much shorter than the 2.5-day circulation time, and one where the fluid has a stable thermal gradient with minimal mixing.

The overall flow path is shown in Figure 3.8.1. No plumbing is routed near or through any of the challenging high-field regions of the detector. This limits locations where fluid lines can access the central TPC volume to the bottom PMT array, and to the perimeter of the TPC near the liquid surface, both of which regions have voltages relatively close to ground. Accordingly two streams of liquid enters the detector from the bottom conduit, one of which is distributed into the dome Skin, and one of which is distributed through the bottom PMT plate and into the TPC. The flow rates into the Skin and TPC are separately controlled. The overall movement is then upward, with LXe spilling over a set of six evenly spaced level-defining weirs for each of the skin and TPC regions. These drain into a triply-segmented drain collection trough, and out through drain tubes. These penetrate the vessel walls to avoid the high field region of the skin near the cathode, and then back to the bottom conduit and over to the purification tower. All tubing and associated fittings housed in the skin will be made from high-reflectivity PTFE so as to minimize absorption of scintillation photons.

The entering fluid is distributed in the dome region, and through the bottom of the TPC through a set of some 20 each small diameter distribution tubes, as seen in Figure 3.8.2. The weirs are housed just outside the gate anode rings, a challenging region with confined mechanical space and relatively high fields created by the the two different voltages of the gate and anode grids rings. Details of the weir assembly are shown in Figure 3.2.4. When the liquid flows over the weir, there is a small height of liquid that depends on the flow rate. This design allows a long weir length, and the weir location to be well registered to the grids. This is important because the S2 light production depends directly on the relative levels of the gate and anode grids and the liquid height.

LXe in the bottom conduit and the HV feedthrough conduit is slowly circulated outward by pumping on the gas space at the ends of these conduits while also applying heat to the LXe. The conduits must be purged because of the outgassing from the plastics in the cables in them, especially at their warm ends for which

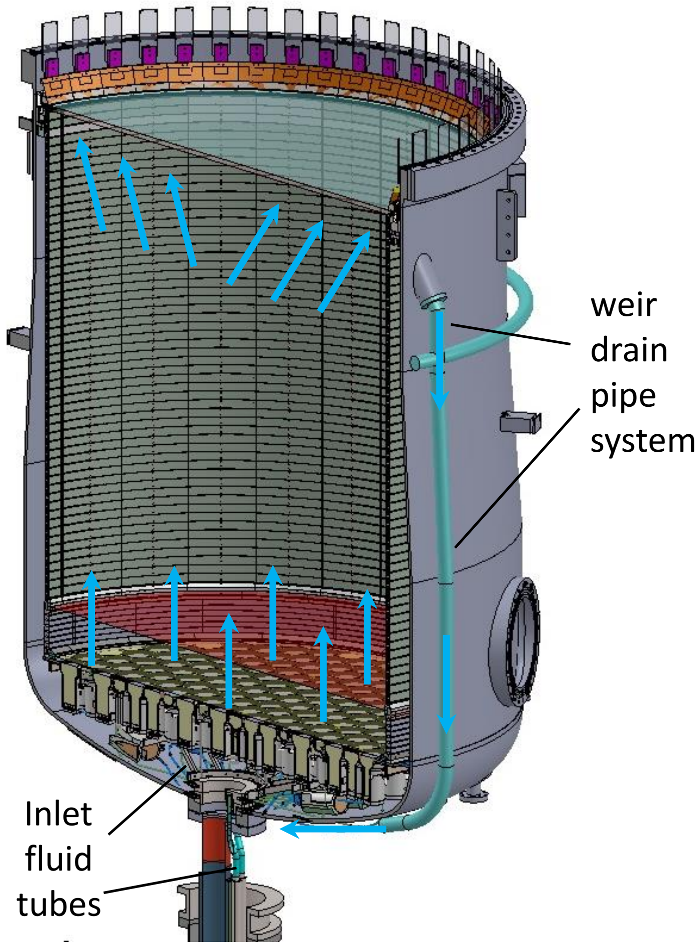

Figure 3.8.1: Cutaway of the Xe detector system, with the internal circulation system elements and flow paths indicated. Purified LXe in two separate tubing sets is distributed into the bottom of the TPC and the bottom of the dome Skin region. The flow is then up to the liquid surface and over a set of liquid level-maintaining weirs, into a set of thee collection troughs and drain pipes, and then return via the bottom conduit to the external system.

outgassing is orders of magnitude higher than from cold plastics. A second potential issue is Rn emanation, especially from the cables in the conduits, some portion of which is warm, especially for the top conduit. The flow from the conduits is thus passed through a Rn removal system described in Section 6.4.5, before it is passed through the main purification system. None of these flows are routed through the heat exchange system. Finally, there is separate capability to pump the gas directly above the TPC (i.e., in the “S2” space) at a low rate, using a set of tubes distributed in the top TPC array much like those in the bottom array.

A central goal in all of these flows is to eliminate as far as practical any stagnant “dead” regions—the prime example of which would be the conduits if they were not purged. Such dead spaces, once impure, serve as a slow source of diffusively-driven impurities that can greatly complicate purification. This is an issue not only for purity that affects charge and light collection, but, critically, following the use of radioactive tritium introduced as a calibration source (see Chapter 7), which must be subsequently removed.

Both the LXe circulation system and the cryogenic system (Section 6.8) must work together to control the overall thermal environment of the detector and also the degree of convection, if any, of the fluid in the TPC.

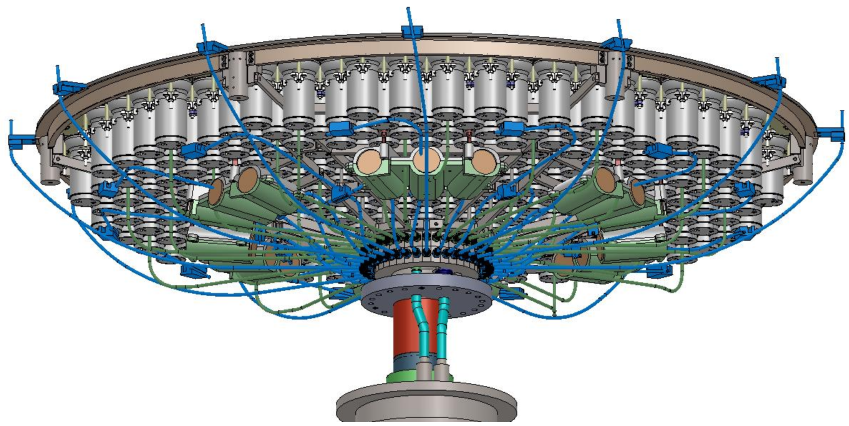

Figure 3.8.2: Fluid distribution in the bottom dome region. Fluid tubes in blue distribute flow into the dome and wall skin regions, while tubes in green distribute fluid into the TPC.

Most cooling of the detector while running will be provided by a set of six thermosyphons attached to the vessel at the level of the liquid surface. The total heat load internal to the vessel (not including cables, whose load is in the conduits) is roughly 40 W, and we plan to deploy up to 30 W from heaters in the bottom PMT array (see below). Most of this heat is applied to the Skin, and so a set of six thermosyphon heads will be deployed around the vessel at the level of the liquid surface. Liquid cooled by these heads and liquid warmed by the radiative load on the wall and the bottom PMT bases in the Skin should set up convective currents that lead to a fairly uniform temperature in the Skin.

The interior of the TPC has a much smaller heat load than the Skin, with only a fraction of the 8 W from the bottom PMTs being transmitted into the TPC (ditto for the 1.4 W from the resistor chains embedded in the TPC field cage). The temperature of the fluids returning to the detector will be set in the purification tower, and so with the fluid entering the TPC can be set to a lower temperature than that in the TPC; this fluid should counter the heat loads from the PMT bases.

In this mode a fairly stable fluid should be achieved in the TPC. Running with a stable, non-mixing fluid has several advantages. It should allow much faster purification because impurities are mostly directly swept out of the detector in the 2.5-day time scale for circulating the fluid. This is termed “batch mode” purification in chemical engineering, as opposed to the “mixed tank” mode obtained with strong mixing in which purification reduces only exponentially with the circulation time as the time constant. Another advantage of a nearly static fluids is that it may be possible to reduce the effect of Rn events by tagging the position of the various daughters and in particular ^{214}Bi, the decay of which produces an important ER background.

However, the use of the dissolved source ^{83m}Kr argues for convective mixing that is at least as fast as its 1.83 h half-life. This source provided the main calibration of position response of S1 and S2 signals in LUX, including the crucial measurement of the electron drift length, which varies over time. Because it is outside (but relatively near) the WIMP-search energy window it was used on a frequent basis, and it would be highly desirable to do the same for LZ. The basic plan for achieving mixing in the TPC is to use heaters installed just inside the outlets of the fluid tubes at the bottom of the TPC, so that fluid enters in a heated state. The amount of power planned to use is up to 30 W. We plan to remove this heat by evaporating liquid from the LXe surface via a set of tubes in the top array that mirror those in the bottom array, and a flow that is limited to rates that do not induce boiling. The combination of cooling at the top and heating below should induce convection motion. It is challenging to fully predict the motion of the fluids, though we plan some studies to analyze design using computational fluid dynamics. The goal of the system described here is to support operations with the fluid in either static or convective states.

Initial cooling of the detector must be done with care in order to avoid large thermal gradients in the TPC structure, which has no obvious thermal anchor point. We thus plan to circulate Xe gas, cooled in the purification tower, to slowly cool the entire system at a controlled rate. We will make use of the separate flow streams in the TPC and Skin, as well as the gas purge in the top dome area, and are using computational fluid dynamics (CFD) to plan the rate of cooling. Sensors described in the next section will be used to monitor this process. We will also attach a thermosyphon head to the bottom of the vessel to allow us to cool the bottom of the detector.

3.9 Xenon System Monitoring

Monitoring sensors are required for controllable and reliable operation of LZ; this Section describes the monitoring systems contained in the xenon space. Some of the data generated by these devices can also be used to identify temporary departures from optimal operating conditions and thus provide additional information for the science analyses. For example, achieving good resolution of the S2 signal relies on a quiet liquid surface, which we will monitor through precision level sensors and acoustic bubble sensors. The thermal profile of the detector is an important aspect of liquid circulation and the stability of the liquid surface, and this is measured by an array of thermometers. The ability of the system to sustain high voltages is very important and a set of loop antennae will measure discharges but may also detect any precursor signals and thus enable mitigation. Bubbles encountering a high-field surface can also lead to discharge and spurious light emission, and thus detection of bubbles is an important aspect of achieving high voltages. Finally, it is important to confirm that the very significant thermal contraction of the plastic field-cage system behaves as expected, and so this motion will be monitored by a set of position sensors. This section discusses the monitoring systems in detail, which are summarized in Table 3.9.1.

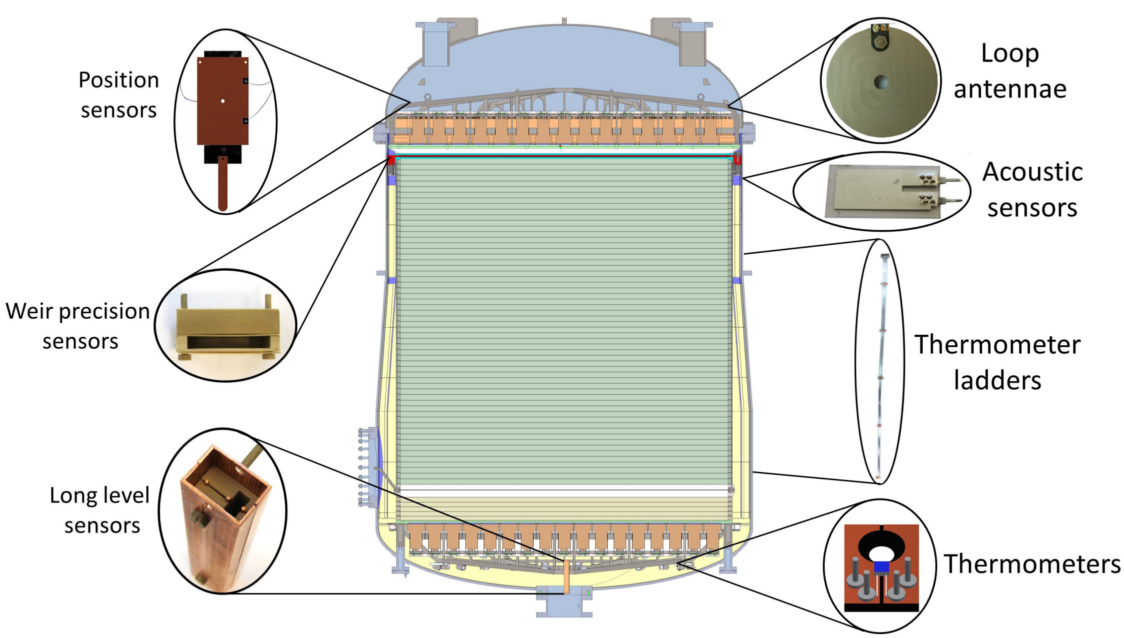

Figure 3.9.1: Schematic diagram of the internal monitoring sensors in the xenon detector.

Table 3.9.1: Monitoring sensors located in the LZ xenon space.

Sensor	Acronym	Number	Location
Thermometers	–	101	66 in Xe space, 35 in vacuum space
Weir Precision Sensors	WPS	6	Surface level
Long Level Sensors	LLS	4	Surface level, dome Skin
Position Sensors	POS	6	On top PMT truss
Loop Antennae	LA	8	On PMT trusses and near HV feedthrough
Acoustic Sensors	AS	8	Attached to IVC outer wall

3.9.1 Thermometers

Temperatures need to be monitored at approximately 100 locations throughout the Xe detector and nearby. The chosen temperature sensor is a platinum (PT100-type) resistor. The readout method is 4-wire throughout and the cabling used is twisted wire bundles in the xenon space, while in the vacuum space of the LZ cryostat it is a semi-rigid polyimide-stainless steel layered composite structure; the latter features parallel strip-line pairs sandwiched between shielding/ground planes on the outside. The design of the semi-rigid cabling is individual to each group of sensors, with a maximum length of a single section being 1.5 m, which is sufficient to cover the height of the ICV. There is a connector block at one end of the semi-rigid cabling at which the signals transition to conventional shielded 4-core wiring to cover the long stretch towards the electronics "breakout boxes", where mechanical robustness and threading capability are important. At the vacuum barriers of the breakout boxes, standard DB25 connectors are used, with 100 thermometers (400 wires) requiring at least 16 such connectors. The provision of DB25 connectors marks the interface to the LZ Slow Control system (Section 8.8). Calibration of the platinum resistors is via a generic table available for these, where precision requirements are less stringent, or from individual calibrations and corresponding look-up tables or polynomial corrections (within the Slow Control), where higher precision is required. At positions where the potential effects of intrinsic component radioactivity is minor, commercial pin headers and sockets can be used. Closer to the center of the detector, a combination of pins and clean PTFE, PEEK, or Delrin connector bodies will be used. All materials used are checked for compatible radiopurity (see Chapter 9).

Cryogenic, laminated, layered semi-rigid cabling will be used for reading out the bulk of the thermometers in the vacuum. This cabling and the low-radioactivity connectors (where needed) will be made in-house to individual designs for easy installation on site. The cable is based on polyimide/Kapton, to which stainless steel is laminated. These raw materials are etched to produce individual cabling and are laminated to receive shielding and ground layers on either side. A minimum track width of 150 μm and pitch of 300 μm have been demonstrated. The electronic capacitance between wire pairs is ≈80 pF/m, depending on detailed geometry and operating temperature (via the temperature-dependent permittivity of Kapton). Thermometer mounting blocks in the xenon space will be based on Cirlex boards.

3.9.2 Liquid Level Sensors

For level sensors, two main designs are needed: a parallel-plate type for precision surface sensing, and long coaxial types. The precision surface sensor (or Weir Precision Sensor, WPS) has the plates installed horizontally, straddling the boundary between the LXe and the electroluminescence region to measure the liquid level with high precision, allowing any tilt of the detector to be readily measured, and seeing variations in the liquid surface—for example from bubbles or surface waves. Six WPS sensors are installed at the weir overflow openings. The coaxial Long Level Sensors (LLS) monitor primarily the liquid levels during filling and emptying of the TPC. There are three such sensors, that will span the height of the weir trough and the full 13-mm gate-anode distance.

The sensors will be read out with high bandwidth (up to 200 kHz) aiming to monitor the condition of the Xe surface (level, ripples, waves) and, as such, will have a precision of ∼10 µm. Further sensors will monitor the bottom Skin region during filling and emptying, and a LLS will be used inside the PMT cabling standpipe to monitor the filling process. A pressure sensor at the bottom of the cryostat vessel measures the head of the liquid and provides further information about the Xe level during filling and emptying. The readout method is via determination of capacitance with respect to a reference capacitance (all sensors employ three electrodes and a feedback readout circuit). This arrangement greatly reduces systematic effects arising from the long cabling in LZ and its variable capacitance (mechanical and thermal effects). The feedback readout circuit is based on modulated readout with a minimum number of analogue components and the bulk of front-end complexity absorbed into the firmware of a field-programmable gate array (FPGA). For feedthroughs at the vacuum barrier, a standard flange with DB25 connectors is foreseen into which the 8-channel readout boards plug directly without need for external cabling. Figure 3.9.2 shows results obtained in a liquid xenon test chamber. The achieved precision satisfied the requirements and features visible in the data are understood.

3.9.3 Acoustic Detection

Acoustic sensor (AS) heads based on a polymer film (PVDF) have been chosen due to constraints on radioactivity levels. The sensors will be installed in direct contact with the outside of the inner cryostat vessel to pick up internal sound. Eight sensors are foreseen, with three at 120° spacing near the lower cylindrical section of the cryostat, three near the top of that section with the same spacing, and one each on the top and bottom domes. The vacuum-barrier electrical connection is via a standard flange with a DB25 connector, interfacing to a dedicated 8-channel differential readout front-end board. Connection to Slow Control is via a standard ModBus interface, allowing to query minimal information such as when an acoustic signal (above trigger) occurred, along with its magnitude and a crude classification of the likely nature of the sound. Simultane-

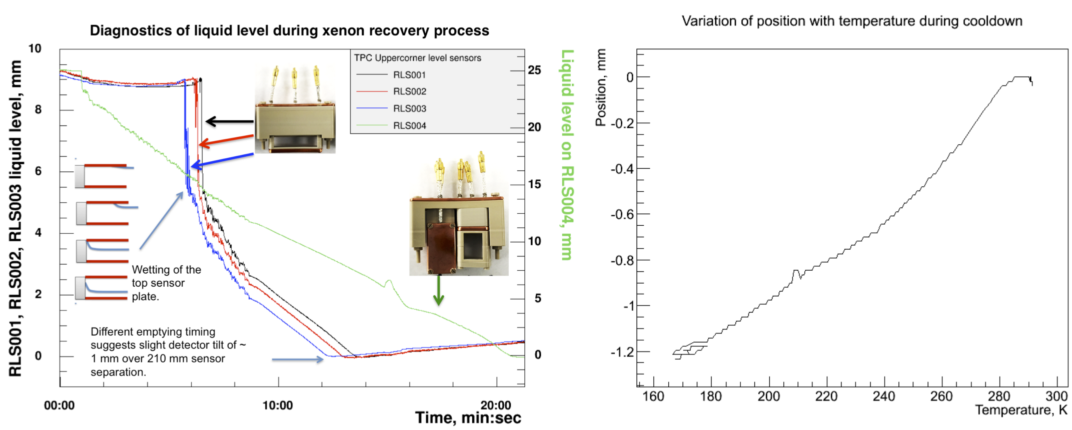

Figure 3.9.2: Left: Data from a Weir Precision Sensor (WPS) and a Long Level Sensor (LLS), installed inside a liquid xenon test chamber, showing xenon being emptied. The shapes of the graphs are well understood; for example, regions pointed to by the arrows can be linked to xenon gradually overflowing level sensor plates, capillary effect, or known fringe fields. Right: Data from a position sensor, showing the contraction of the TPC as it cools.

ously, via a different Ethernet readout channel, complete acoustic recordings from the sensors, sampled at rates up to 200 kS/s will be available for feeding into the fast data stream and for subsequent off-line analysis.

3.9.4 Loop Antennae for Discharge Detection

To monitor for onsets or occurrence of HV breakdown events, loop antennae (LA) capable of picking these up will be installed in critical positions. Eight such antennae will be assembled on the top and bottom PMT-array trusses, sufficiently far from high-field regions to ensure that the presence of the metal aerials does not interfere. With such a set of LA sensors, insight into locations of possible HV breakdowns and types should be possible. The feedthrough at the xenon space to the external environment will be through a DB25 connector, similar to the PMT readout. Two sets of fast 4-channel readout electronics with a sampling rate of up to 200 MS/s will be used. The readout board can be polled by the Slow Control through a standard ModBus interface. It will provide a fast digital signal for alerting the HV power supplies to situations when a quick shut-down is required, and there will be capability for reading out triggered fast signals for inclusion in the data stream and further offline analysis.

3.9.5 Position Sensors

Position Sensors (POS) capable of measuring linear displacements of up to about 2 cm will be fitted on and around the top PMT array to monitor the thermal contraction and expansion of the TPC during cooling and warming, allowing to apply countermeasures, if needed, to ensure uniform cooling or warming of the TPC. These sensors will also give important information on any lateral displacements that would alter the Skin region gap, and the alignment of the top PMT array with respect to the TPC anchor points. The operating principle of the displacement sensors is based on picking up linear travel via a slider that moves a dielectric between two adjoining parallel plate capacitors. The position sensors are of simple and robust design and made from radiopure materials. The electronic readout is based on the same feedback circuit used in the level sensors, which acts to minimize the effect of cable capacitance on the sensor output. Eight sensors (three for vertical movement, three for horizontal movement, and two for helical movement) will be installed.

3.10 Integrated System Testing

A vital part of the preparation for LZ is the testing of key design aspects and critical components of the Xe Detector and integrated "System Testing" of the TPC and associated systems. Several small LXe test chambers, with less than 10 kg of LXe, are available at LZ member institutions, targeting studies in specific areas (spurious electron and photon emission from grid wires, VUV reflectivity measurements, small-component QA testing). Additionally, a larger System Test platform has been developed at SLAC which can operate with over 100 kg of LXe, conducting integrated tests to answer broader HV performance questions, and involving full-scale sub-systems in some cases. This coordinated, multi-scale approach is a key part of the risk mitigation strategy in LZ. We outline the tests being performed at collaborating institutions in Table 3.10.1.

3.10.1 Reflectivity Measurements

The performance of both the TPC and the Skin detectors is strongly dependent on their ability to collect xenon scintillation light, and this is in great measure driven by the reflectance of the surfaces that surround these LXe volumes. The optical performance of these systems has been described in Sections 3.5 and 3.7. PTFE is the material of choice in LZ and past LXe detectors, used due to its surprisingly high bi-hemispherical reflectance. However, there remains some uncertainty as to the precise value and angular distribution of this reflectance, and its dependence on precise material provenance and surface properties. In fact, high-quality

Table 3.10.1: High priority studies and tests to be performed with small LXe chambers or the SLAC System Test facility. Note that SLAC I (II) denotes SLAC (Phase-I) or (Phase-II). Timing of results is indicated (calender years).

Studies/Tests	Topics	Groups Involved	Results
Reflectivity	PTFE reflectivity in LXe	Coimbra / U-M	2016
	PTFE reflectivity vs thickness	Coimbra / U-M	2016–2017
Wire tests	Electron/photon emission studies	Imperial	2015
	Small wire-grid testing	LBNL	2016
	Effect of electropolishing/passivation	Imperial	2016
HV studies	Cathode ring: large area at HV	UC Berkeley	2016
	Effects of surface treatment	SLAC I	2015–2017
TPC prototype tests	Reverse field region (RFR)	Yale/SLAC I	2014–2015
	HV performance	SLAC I	2016
	Skin optics and performance	SLAC I	2016
	Handling/cleanliness protocols	SLAC I/SLAC II	2016–2017
Full scale grid tests	Electroluminescence region	SLAC II	2017
	RFR with full surface fields	SLAC II	2017

optical data is lacking in the VUV range for many materials of interest. As was shown in Figure 3.5.2, a few percent difference in PTFE reflectivity has a noticeable impact on the performance of the detector.

At LIP-Coimbra, Portugal, a dedicated chamber is operated for the measurement of PTFE reflectance in LXe, which follows on from earlier studies of angular profile and total reflectance of different PTFE samples for the xenon scintillation wavelength at room temperature [7, 8]. The chamber used for the new measurements is represented schematically in Figure 3.10.1 (left and center). A volume of LXe enclosed by PTFE walls is topped by a PTFE "plunger"; the chamber is 10 mm × 10 mm in cross section and up to 150 mm in height. The scintillation light is provided by an ^{241}Am source deposited onto a small stainless steel holder and attached to inner surface of the movable wall. After traveling across the LXe volume and bouncing between the PTFE walls, the scintillation light is detected by a single PMT which makes up the bottom of the chamber.

Preliminary experimental results obtained for one PTFE sample (APT #807NX, a possible material for LZ) are shown in Figure 3.10.1 (right), overlaid with the corresponding fit. The PTFE/LXe reflectivity ($\boldsymbol{R}$) is obtained by fitting the measured relative light collection at different LXe heights with the prediction of the detailed simulation model described in Ref. [7]. The Monte Carlo framework for this model is the ANTS2 package [38]. The free fitting parameters were the PTFE albedo in LXe (A_{liq}), the PTFE refractive index (n), and the attenuation length (λ) for the scintillation light in LXe (these are indicated in the figure, and λ>2 m). The LXe refractive index and the mean free path for Rayleigh scattering were fixed and set to 1.69 and 29 cm, respectively.

These optical measurements are challenging and prone to systematic uncertainty and, due to the importance of PTFE to our design, additional reflectivity studies are being conducted with the MiX detector at the University of Michigan. These utilize a cylindrical PTFE structure with a PMT on the bottom, a circular PTFE disc on the top that floats on the LXe, and a ^{210}Po alpha source on the circular disc facing down, as shown schematically in Figure 3.10.2 (left). As the chamber is filled, the floating circular PTFE disc rises and

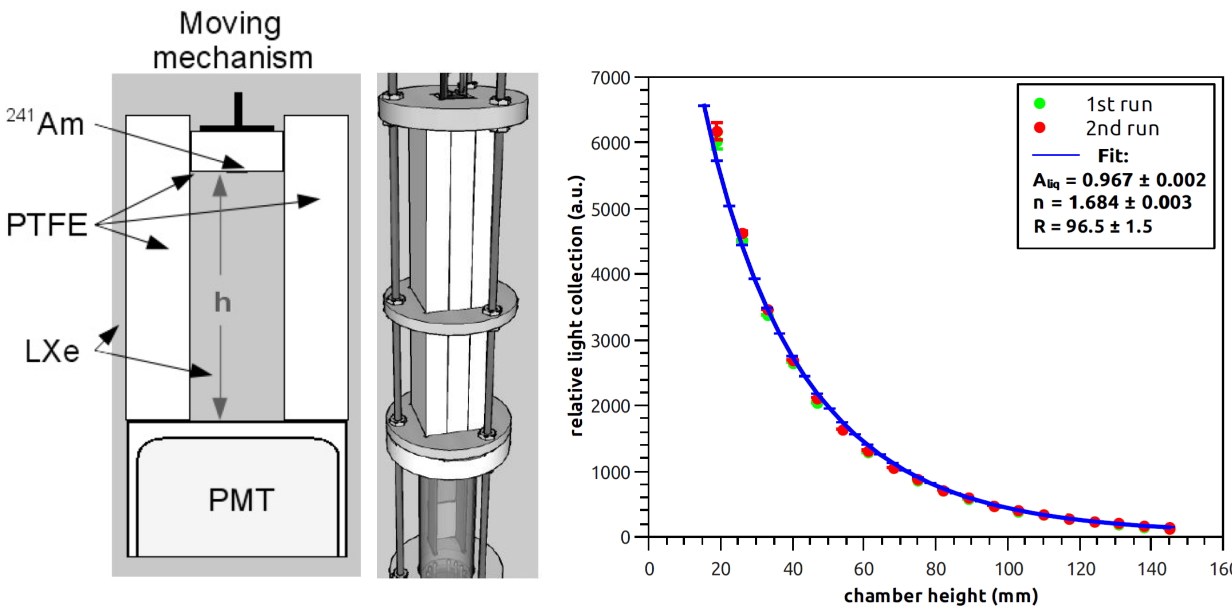

Figure 3.10.1: Measurements of PTFE/LXe reflectivity at LIP-Coimbra. The PTFE-built chamber is shown schematically on the left and center. The height of the chamber (h) is varied with a "plunger" mechanism as an alpha source generates scintillation in the LXe; this is detected with a PMT at the bottom. The relative optical response as a function of the chamber height is fitted by the optical model described in Ref. [7] with three free parameters, from which the reflectivity, R, is derived. Preliminary results are shown on the right for two independent runs with the same PTFE sample (the error bars are smaller than the markers); the fit result indicates R=(96.5 ± 1.5) % for this sample.

the fractional area, defined as the PMT photocathode area divided by the total surface area of the chamber, diminishes.

It is desirable to minimize the thickness of any PTFE panels in the LZ TPC and Skin detectors, in order to reduce dead volumes around the active LXe, outgassing and potential backgrounds. A lower limit on this thickness is established by the PTFE transmittance to xenon scintillation light, and the need for optical isolation between the TPC and Skin regions—as well as between these and any dead regions containing LXe. Preliminary measurements have been carried out for APT #807NX PTFE that cover chamber wall thicknesses from 1 mm to 9.5 mm, as shown in Figure 3.10.2 (right), to verify the minimum panel thickness required in LZ. These data suggest that decreasing the PTFE wall thickness in this range does not appear to change reflectance. Further measurements will be carried out for various surface treatments and PTFE materials at thicknesses from 1 mm to 9.5 mm. Following the PTFE measurements, these chambers will go on to study the optical properties of grid wires and other materials (e.g., the non-reflective PEEK used at the perimeter of the gas region).

3.10.2 HV Studies in Small Two-Phase Chambers

To ensure the successful delivery of HV to the LZ TPC we take a comprehensive approach, beginning with an experimental study of the physics processes involved in the electric breakdown of individual cathode wires at a microscopic (quantum) level. Chambers at Imperial College London and Lawrence Berkeley National Lab have been built and operated for this purpose.

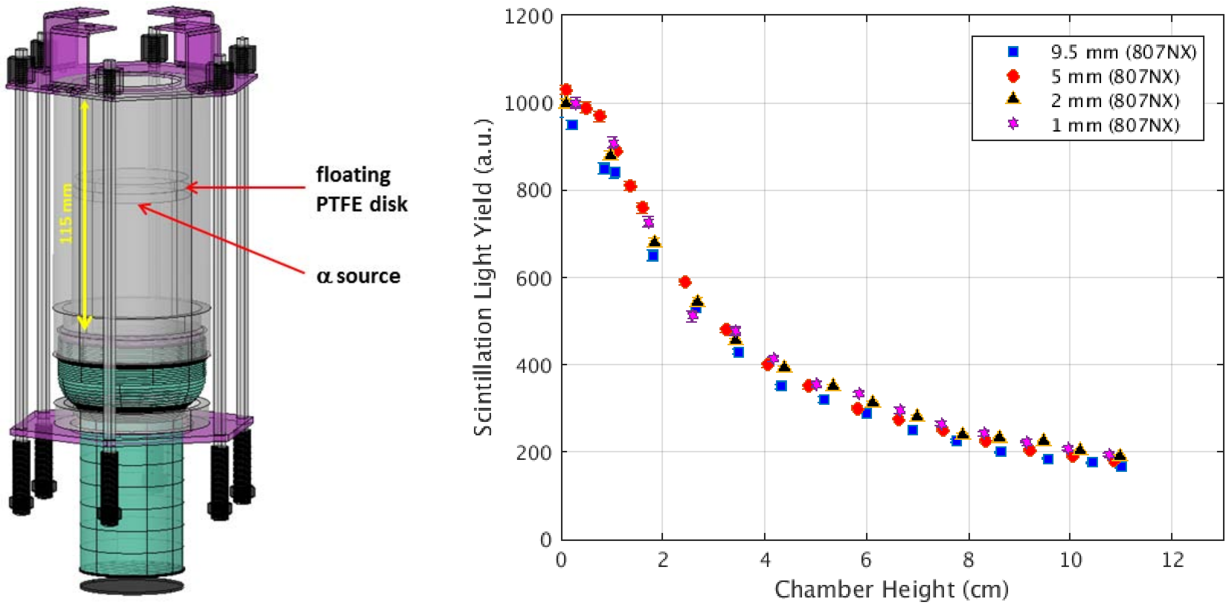

Figure 3.10.2: Left: Schematic view of the U-M PTFE reflectivity setup which is based on the MiX chamber [41]. It consists of a 3-inch Hamamatsu R11410 PMT which covers the bottom part of the 4.6-inch high and 2.45-inch ID PTFE cylinder, and a Po-210 source to provide a mono-energetic light source. The fractional area in the setup is varied as the floating disc raises or descends inside the PTFE cylinder. Right: Preliminary results for light yield as a function of PTFE wall thickness for APT #807NX PTFE. **Draft figure, will be updated soon**

Electron and photon emission are observed from cathodic surfaces in LXe at relatively low electric fields: ~10 kV/cm, a factor of 100 to 1,000 lower than expected for standard (cold cathode) field emission from metals. These have caused serious limitations to the operating voltage of previous LXe TPCs, almost without exception. These emissions can be caused by local enhancement of the electric field combined with the presence of thin insulating layers, surface defects, or other effects that result in a lower effective work function. This may be accompanied by simultaneous photon emission. We must understand the physical origin of these emissions and then develop effective mitigation in time to inform the production of the LZ wire grids. The extraordinary sensitivity of the S2 response, discussed in Section 3.6, means that electron emission must be prevented at all cost up to the 50 kV/cm maximum field which we allow for cathodic surfaces in LXe (e.g., the cathode and gate grids and their connections).

At Imperial, a small two-phase chamber was developed to study individual cathode wire samples installed at the bottom of the liquid region, where a cathode grid would normally exist—see Figure 3.10.3. This configuration ensures that high electric fields can be achieved at the wire surface by applying modest voltages (e.g. ≈150 kV/cm for a 100-µm sample and ≈400 kV/cm for 40 µm wire for a cathode voltage of 5.5 kV). This study focuses on the phenomenology associated with the onset of electron and/or photon emission. In particular, we are exploring its dependence on electric-field strength, wire material, surface quality, history, as well as the effectiveness of mitigation steps such as conditioning, electropolishing, and chemical passivation.

The chamber has a single internal PMT viewing down from the gas phase to detect both photon and electron emission from the wire sample. The electroluminescence response has single-electron (SE) sensitivity, allowing to measure minute currents (~100 e/s, or 10^{-17} A). The gate and anode grids, 14 mm apart, straddle the liquid surface, ensuring S2 yields that are mostly independent of the cathode voltage and sufficiently high

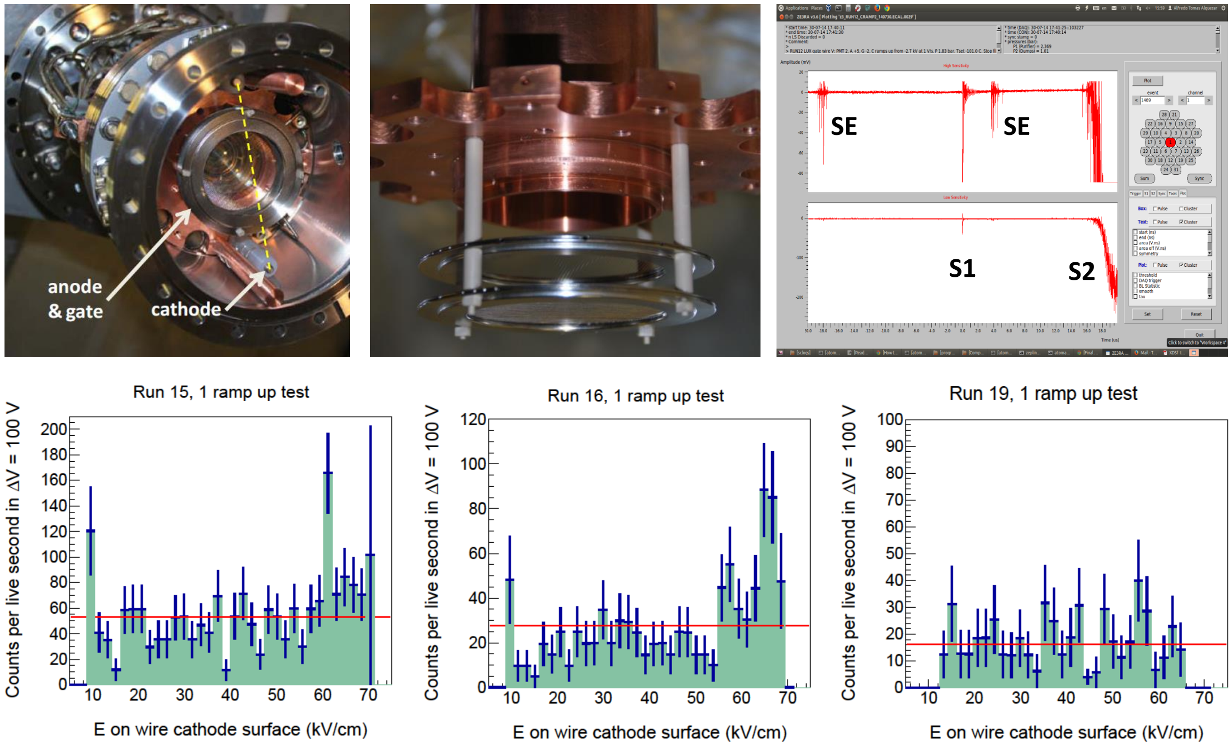

Figure 3.10.3: Imperial chamber to study electron and photon emission from thin wires; Top from left: Photograph of upward view of the chamber from the bottom, indicating the location of the cathode wire and the gate-anode system (a PMT window can be seen through those grids); Photograph of side view of the gate and anode grids, 14 mm apart; An example event showing S1 and S2 pulses (in dual dynamic range) as well as two single electron (SE) pulses; we search for candidate SE pulses unrelated to any particle interactions producing S1 and S2. Bottom: Evidence for electron emission from a 200 μm stainless steel wire (same type as used in LUX) before treatment (two samples shown left and center) and after electropolishing (right).

for efficient cross-phase extraction and SE detection. The 130-mm-long cathode wire is mounted 25 mm below the gate, stretched between two feedthroughs that deliver up to −5.5 kV to the liquid. Electric field lines radiating from the upper surface of the sample guide emitted electrons to the electroluminescence region in the gas where they are detected with high efficiency. Most subsystems required to operate the chamber were inherited from ZEPLIN-III. The ZE3RA analysis software allows full exploitation of the 2-ns-sampled waveforms [42], which are recorded in high- and low-sensitivity channels to cover both very small signals and larger S1 and S2 pulses (Figure 3.10.3, top right). The voltage applied to the wire sample is ramped up slowly (1 V/s) to several kV, with PMT signals being digitized simultaneously. Electron emission from the cathode can, if accompanied by prompt light, be reconstructed to the cathode depth by electron drift time.

We find such emission occurring from fields as low as ≈10 kV/cm in some wires (e.g. 200 μm stainless steel), while at least one other could withstand hundreds of kV/cm without any discernible effect (40 μm BeCu). Emission episodes are consistent with average SE rates of 100 Hz to 1,000 Hz (faster, “impulsive” structure can be observed within these). Two examples are shown in Figure 3.10.3 (bottom left and center) for samples from the 200 μm LUX cathode wire, the least resilient tested so far. In some instances we have evidence of simultaneous photon emission, which suggest that the local electric field is higher than the electroluminescence threshold of LXe [43]. Emitters are (probably) localized in field, and they are rarer and fainter on a second ramping test, suggesting a partial conditioning effect. Significantly, they subside at higher fields and are not reproducible subsequently. We tested electropolished samples of the same wire and obtained significantly improved results, as shown in the same figure (bottom right). Finally, we will explore chemical passivation. Both of these measures can be applied to the LZ grids.

At LBNL, the test bed pictured in Figure 3.10.4 is operated which is functionally similar to that at Imperial, but devoted to evaluate small cathode wire planes consisting of a stainless steel frame and stretched wires. A key question is whether this performance can be simply inferred from the single-wire studies, or if the length of wire is in fact a critical parameter. A complete cathode grid frame will allow an approximate 10-fold increase in wire length compared with a single wire. This chamber has also improved electric field uniformity as well as higher light collection, allowing a better understanding of the correlation between electron and photon emission. The baseline gate-anode design can be studied in detail at this scale. Other studies with this chamber will include understanding more rigorously the cross-phase electron emission process at the liquid surface.

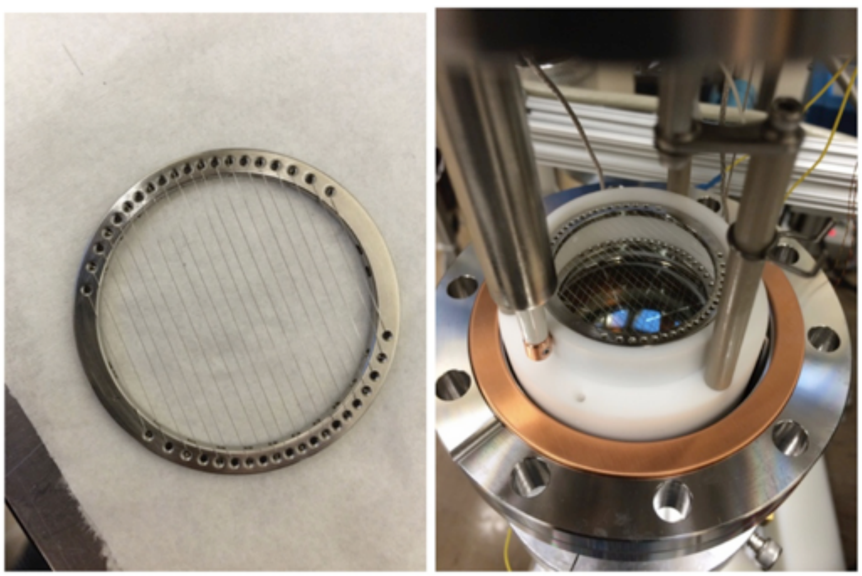

Figure 3.10.4: Left: A wire grid that will be tested in the small LBNL test chamber. Right: Photograph of the LBNL small grid test chamber.

3.10.3 TPC Design Testing

Larger, scaled components of the LZ TPC must also be tested to assure high voltage performance. It is critical that these assemblies sustain the applied cathode voltage without producing light from electrical discharges across their components or to the inner wall of the cryostat. The scaled Phase-I TPC design for testing has a 6-inch inner diameter, and with appropriate scaling of the vessel, achieves the same surface and bulk fields as LZ with the application of half the desired cathode voltage, i.e. $-50\,\mathrm{kV}$ in LZ is equivalent to $-25\,\mathrm{kV}$ in the System Test.

The design of the Phase-I TPC is shown in Figure 3.10.5. It follows closely that of the LZ TPC, being roughly divided into three functional sections. The first is the reverse-field region between the cathode and bottom grids, with five pairs of resistors grading down to ground with a total $12.5\,\mathrm{G}\Omega$ impedance set between four field-shaping rings enclosed in PTFE. Above that, the drift field region consists of 20 resistor

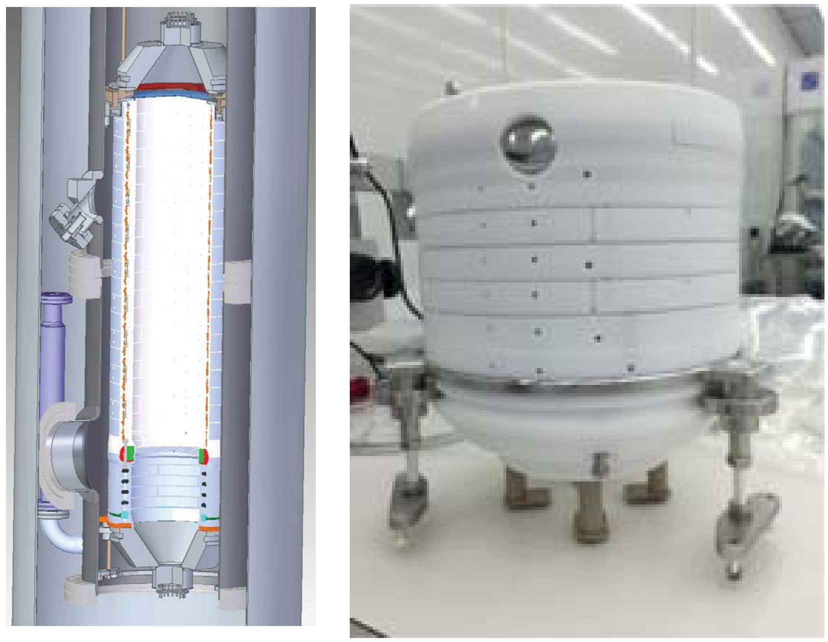

Figure 3.10.5: Left: Schematic CAD representation of the full SLAC Phase-I TPC; Right: Photograph of the Phase-I reverse-field region.

pairs running from the cathode to the gate grid between field shaping electrodes encased in PTFE rings within the LXe. The final section is the electroluminescence region, which consists of the gate grid, weir manifold, and anode grid, and spans the liquid surface. PMTs, located at the bottom and top of the TPC, provide the primary data on emission, supplemented by optical fibers running to an external camera for data on electrical breakdown.

A scaled reverse field region, from the cathode to the bottom grid, was first tested in liquid argon (LAr) at Yale University in 2014. A schematic view of the setup is shown in Figure 3.10.6 (left) and dewar and HV connection (right).

The HV tests were performed within a 240-liter cryogenic dewar of 16-inch bore. The bottom of the tested assembly was grounded by the platform; the top was connected to HV that can be ramped to 200 kV to simulate the LZ cathode. The HV is delivered through a polyethylene cable that originates at a feedthrough located 8 foot above the top of the dewar. The feedthrough is connected to a DC power supply from Glassman High Voltage. A controlled electrostatic environment was maintained around the test assembly by surrounding it with a highly transparent grounded metal mesh that shields any nearby structures. Seven lenses at various locations viewed the assembly from just outside the mesh. These were connected to fiber bundles that routed the images to a charge-coupled device (CCD) camera located just above the top flange of the LAr dewar, providing a real-time view of any electrical discharges that occurred during testing. Below the tested assembly was a quartz window coated with fluorescent tetraphenyl butadiene (TPB) wavelength shifter. This window was viewed by an 8-inch PMT, giving efficient detection of ultraviolet light with single-photon sensitivity.

The tests completed at Yale identified the installed RFR resistors as a weak point when oriented vertically (required by the small radius of curvature of the Phase-I TPC) and with resistors connected in series together between field shaping rings. The camera system identified light produced at the resistor locations during breakdown, as shown in Figure 3.10.7 at fields equivalent to 200 kV applied in LZ, and this guided us to the current design of more field shaping rings in the reverse field region with resistors oriented horizontally and not connected directly to each other.

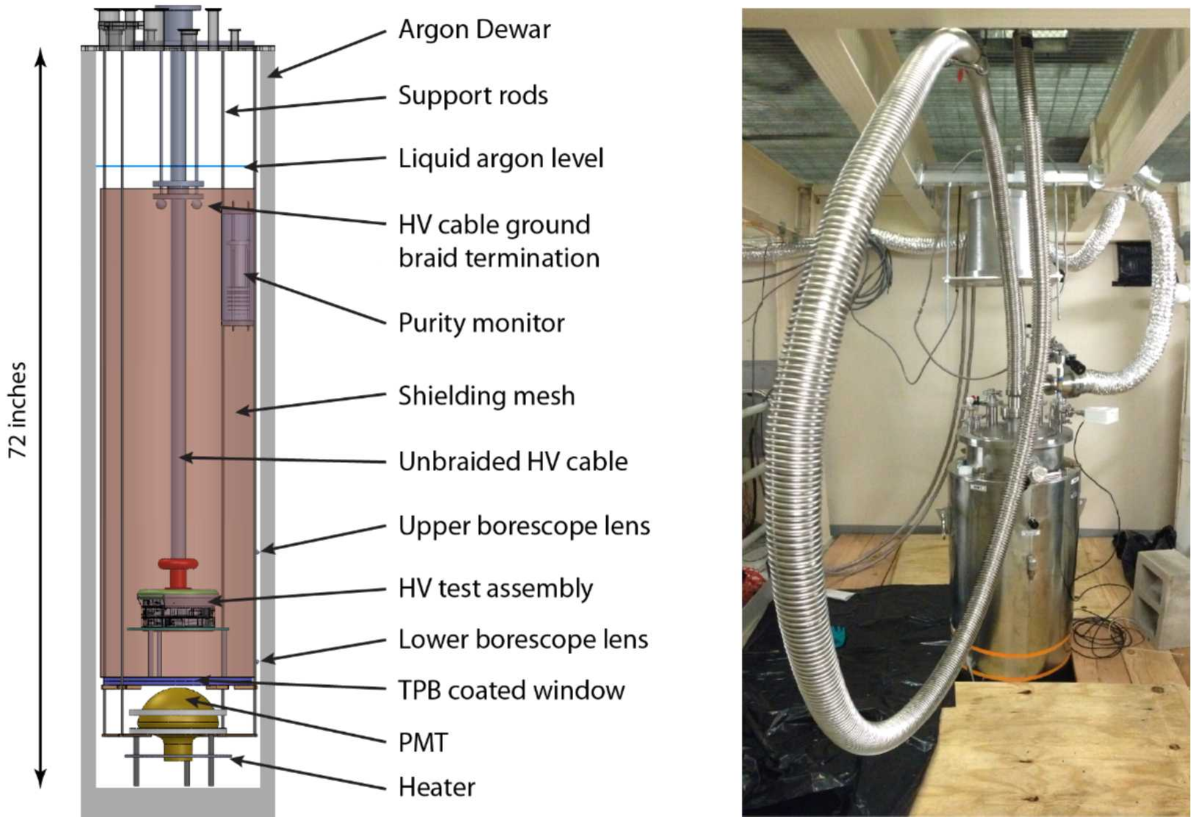

Figure 3.10.6: Left: Side view showing the internal components of the liquid argon test system. Note that the vertical support rods (shown out-of-plane in this view) are positioned outside the shielding mesh. For clarity, only two of the seven borescope lenses are shown. The HV test assembly shown here is a portion of the grading structure of the reverse- field-region of the detector. Right: The liquid argon Dewar and HV cable conduit. The HV feedthrough sits above the square hole in the steel grating at the top of the image.

Using this system, future HV tests are planned for the cathode connection region. The cathode connection grading structure and the connection itself will undergo testing at voltages up to -150 kV, while viewed by a PMT and CCD camera as in previous tests. Any glow of these components under applied voltage, or electrical discharges from high voltage to ground will be immediately visible. Purity of the LAr will be monitored using a small TPC with Au photocathode to ensure that electron lifetime is sufficiently high that impurities do not suppress electrical breakdown. A schematic of this test setup may be seen in Figure 3.10.8.

The Phase-I TPC will undergo testing in liquid xenon at the SLAC System test platform. The staging at SLAC is shown in Figure 3.10.9. The former BaBar counting room and surrounding space in the IR2 experimental hall was renovated for the purpose of hosting this system, with ample room for expansion. A soft-wall clean area with HEPA units surrounds the vessels. The support systems for these test vessels, partially visible in Figure 3.10.9, are extensive. They build on developments from LUX and ZEPLIN and serve as prototypes of what will be used on LZ. Cryogenics for both phases are supplied by a thermosyphon system, which consists of a multi-port LN_2 dewar capable of providing more than 12 separate PID-controlled cooling heads.

The system for online purification through a hot getter uses highly automated gas-handling panels based on 1/2-inch-diameter tubing that will accommodate flow rates well in excess of 100 slpm. The system also

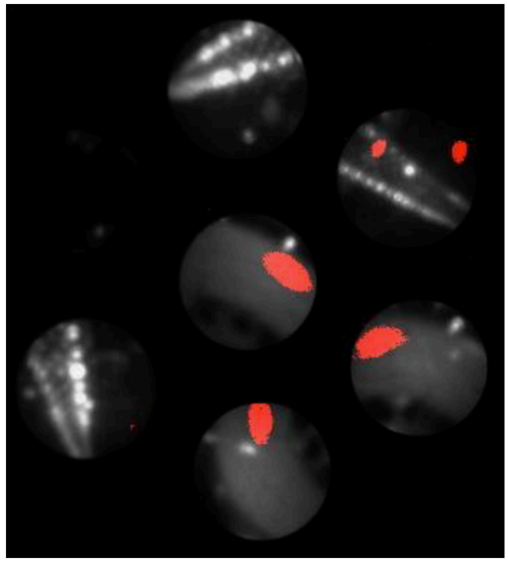

Figure 3.10.7: Image from 7 fibers from the RFR tests at Yale. Light preceding breakdown at the locations of the resistors is shown in red, overlaid on the images of the RFR under LED illumination.

features a high-flow capacity metal diaphragm compressor as the circulation pump. This technology allows very high flow rates and has been identified (Chapter 6) as the technology for LZ, but to our knowledge it has not been used in any previous similar Xe experiment. Thus, the system will provide an important test of these pumps.

Critical elements of control and fail-safe recovery of the Xe have also been developed as part of the system test platform, including integration of process loop controllers (PLCs) for essential systems and integration with larger slow-control system development. Phase-I Xe recovery uses a thermosyphon-driven storage and recovery vessel patterned on a similar device used for LUX. Elements of the planned LZ online and slow-control systems have been developed for the system test to allow a high degree of test automation. The gas system is also designed to be closely integrated with an automated, high-sensitivity purity-monitoring system initially developed by the Maryland group. This will be important in order to achieve purity for successful HV testing; it also allows us to check our understanding of various parameters related to purification that will be important for LZ. Finally, the system is designed to accommodate the range of gaseous radioactive calibration sources deployed in LUX and planned for LZ.

The SLAC Phase-I vessel set is shown in Figure 3.10.10 (left) with the primary Xe vessel on the left, and the purification tower on the right of the image. The purification tower includes prototypes of the elements of the circulation system planned for LZ: a weir reservoir, two-phase heat exchanger, gas-phase heat exchanger, and a "sub-cooling" thermosyphon head on the condensing stream, along with an extensive set of fluid level sensors and thermometers.

The Phase-I tests will continue at SLAC through the spring of 2017 and will allow the assurance of HV operation of the TPC under controlled conditions as well as other LZ subsystems.

3.10.4 Full Scale Grid Testing at SLAC

A second stage of testing will occur at the SLAC platform to test full LZ-scale grids in liquid xenon. Initially, prototype full scale grids will be tested to confirm the cleaning and handling procedures developed through the Phase-I tests, prior to the testing of the final LZ grids, including the full gate-anode assembly.

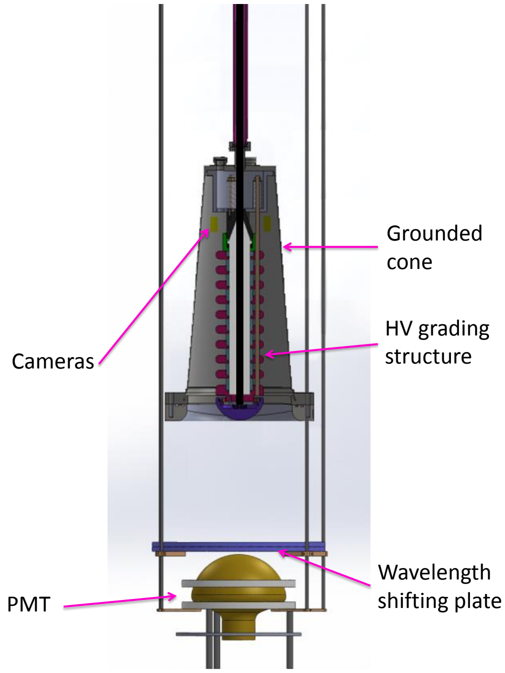

Figure 3.10.8: Schematic of the planned HV test of the cathode connection region immersed in LAr.

The cryostat for Phase-II is shown in Figure 3.10.10 (right). It will hold 60 kg of LXe per cm of liquid height, and is expected to operate at approximately 6 cm of depth. The extraction region of the gate and anode grids will be tested as a full assembly to full operational voltage. A shortened reverse field region with the cathode and bottom grid will, as in the Phase-I tests, scale the surface fields to LZ values with a reduced cathode voltage.

Optical cameras and a limited number of PMTs will instrument the Phase-II vessel set to look for emission at operational fields. Other instrumentation in the xenon will also combine LZ prototypes, final hardware (such as temperature and level sensors), and some hardware used specifically in the SLAC tests (cathode feedthrough and digitizers).

For Phase-II the purification and circulation system developed for Phase-I will be used, with the exception of requiring a compressor-based recovery system for the larger quantity of xenon. We will recover into standard storage cylinders, as is planned for LZ. This requires a highly reliable system with generator-based backup power.

The Phase-II testing of the final LZ grids in liquid xenon will be the culmination of the system test program and the final assurance of the TPC meeting both the HV performance requirements and goals.

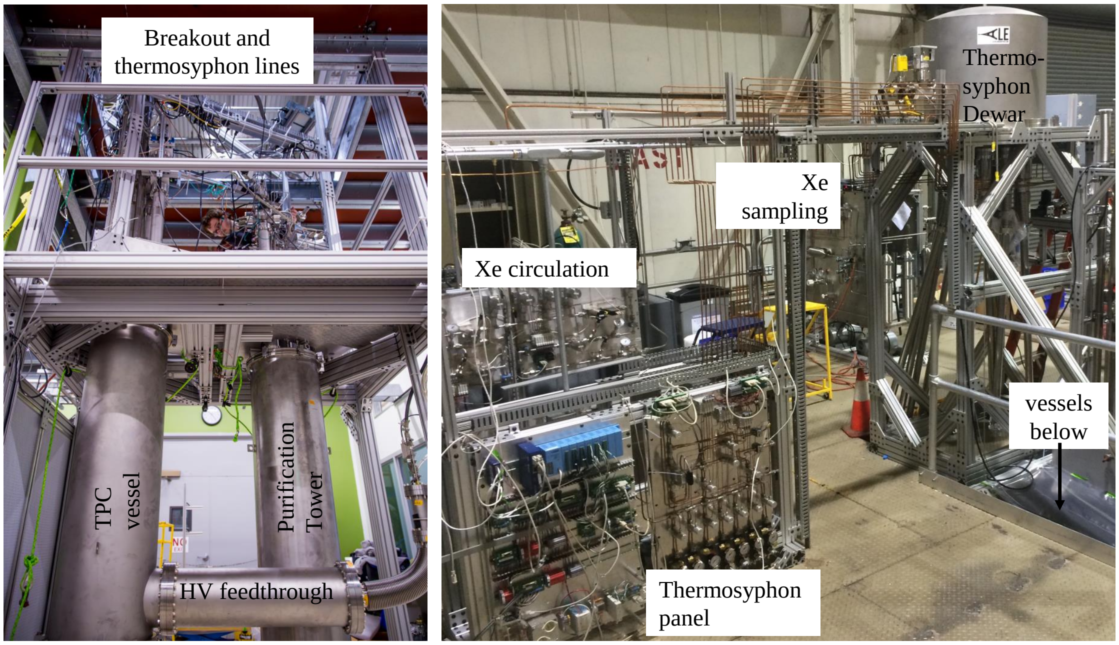

Figure 3.10.9: The LZ System Test platform at SLAC. Left: Phase-I system, consisting of the TPC vessel on the left with a side-entry cathode HV feedthrough visible at the bottom, purification tower on the right, and various PMT, other grid HV, plumbing and cryogenic breakouts above. Right: Support infrastructure housed above the vessels, consisting of thermosyphon system gas panel at front left, Xe circulation panel behind that, and the multi-port thermosyphon dewar at upper right. The cold-trap Xe assay system developed by the Maryland group is in the back right.

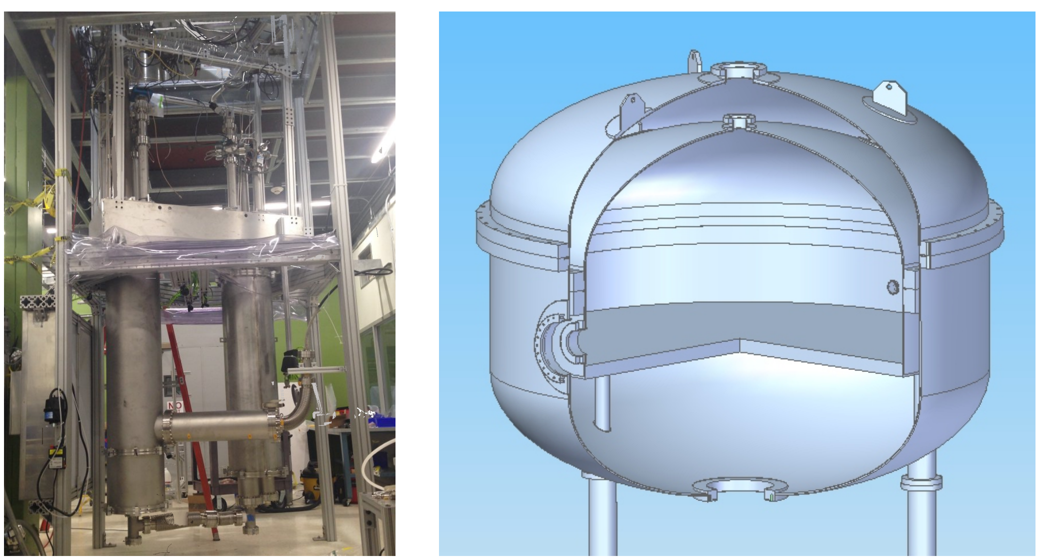

Figure 3.10.10: Left: SLAC Phase-I vessel set; On the left is the primary Xe vessel containing the TPC, and the HV feedthrough extends horizontally to the right. The purification tower is the vessel on the right, containing the weir reservoir, heat exchangers and sub-cooler. The HEPA units are visible on the left of the stand, and the cleanroom curtains are rolled up on the detector stand for the photograph. Right: Phase-II Xe vessel design, to test full-scale LZ grids. At the full diameter, 60 kg of xenon will be needed per cm of liquid height.

3.11 Bibliography

[1] D. S. Akerib *et al.* (LZ), (2015), Conceptual Design Report; LBNL-190005, FERMILAB-TM-2621-AE-E-PPD, arXiv:1509.02910 [physics.ins-det].

[2] W. Blum, W. Riegler, and L. Rolandi, *Particle Detection with Drift Chambers*, Particle Acceleration and Detection (Springer Berlin Heidelberg, Germany, 2008).

[3] K. McDonald, *Notes on Electrostatic Wire Grids*, Tech. Rep. (Joseph Henry Laboratories, Princeton University, Princeton, NJ 08544, 2003).

[4] Y. Mei, *Direct Dark Matter Search with the XENON100 Experiment*, Ph.D. thesis, Rice University (2011).

[5] E. Gushchin, A. Kruglov, V. Litskevich, A. Lebedev, and I. Obodovski, Sov. Phys. JETP **49**, 856 (1979), [Zh. Eksp. Teor. Fiz. **76**, 1685 (1979)].

[6] A. Fonseca, R. Meleiro, V. Chepel, A. Pereira, V. Solovov, and M. Lopes, in *Nuclear Science Symposium Conference Record, 2004 IEEE*, Vol. **1** (2004) pp. 572–576, *Study of secondary scintillation in xenon vapour*.

[7] C. F. P. da Silva, *Study of the reflectance distributions of fluoropolymers and other rough surfaces with interest to scintillation detectors*, Ph.D. thesis, Universidade de Coimbra, Faculdade de Ciências e Tecnologia (2009).

[8] C. Silva, J. Pinto da Cunha, A. Pereira, M. I. Lopes, V. Chepel, V. Solovov, and F. Neves, Nucl. Instrum. Meth. **A619**, 59 (2010), arXiv:0910.1058 [physics.ins-det].

[9] G. K. White and P. J. Meeson, *Experimental Techniques in Low-Temperature Physics* (Oxford University Press, 2002).

[10] DuPont Fluoroproducts, *DuPont PTFE Properties Handbook* (DuPont Fluoroproducts, 1996) P.O. Box 80713, Wilmington, DE 19880-0713.

[11] J. K. Miller, S. Howe, and W. E. Spear, Phys. Rev. **166**, 871 (1968).

[12] U.S. Department of Energy, *DOE Handbook: Electrical Safety*, Tech. Rep. DOE-HDBK-1092-2013 (Forrestal Building, 1000 Independence Avenue, SW, Washington, DC 20585-0002, USA, 2013).

[13] D. S. Akerib *et al.* (LUX), Nucl. Instrum. Meth. **A703**, 1 (2013), arXiv:1205.2272 [physics.ins-det].

[14] K. Nakamura, Y. Hamana, Y. Ishigami, and T. Matsui, in *1^{st} International Conference on Technology and Instrumentation in Particle Physics, TIPP09, Tsukuba, Japan, March 12-17, 2009*, Nucl. Instrum. Meth., Vol. **A623** (2010) pp. 276–278, *Latest bialkali photocathode with ultra high sensitivity*.

[15] H. M. Araújo *et al.*, Nucl. Instrum. Meth. **A521**, 407 (2004).

[16] D. C. Malling, *Measurement and Analysis of WIMP Detection Backgrounds, and Characterization and Performance of the Large Underground Xenon Dark Matter Search Experiment*, Ph.D. thesis, Brown University (2014).

[17] E. Aprile *et al.* (XENON1T), Eur. Phys. J. **C75**, 546 (2015), arXiv:1503.07698 [astro-ph.IM].

[18] T. Haruyama, AIP Conf. Proc. **613**, 1499 (2002).

[19] Z. Liu, J. Chen, P. Zhu, Y. Li, and G. Zhang, Appl. Rad. Isot. **65**, 1318 (2007).

[20] C. H. Faham, *Prototype, Surface Commissioning and Photomultiplier Tube Characterization for the Large Underground Xenon (LUX) Direct Dark Matter Search Experiment*, Ph.D. thesis, Brown University (2014).

[21] C. H. Faham, V. M. Gehman, A. Currie, A. Dobi, P. Sorensen, and R. J. Gaitskell, J. Instrum. **10**, P09010 (2015), arXiv:1506.08748 [physics.ins-det].

[22] J. Jortner, L. Meyer, S. A. Rice, and E. G. Wilson, J. Chem. Phys. **42**, 4250 (1965).

[23] V. Chepel and H. Araújo, J. Instrum. **8**, R04001 (2013), arXiv:1207.2292 [physics.ins-det].

[24] V. N. Solovov, V. Chepel, M. I. Lopes, and A. Hitachi, Nucl. Instrum. Meth. **A516**, 462 (2004), arXiv:physics/0307044 [physics.optics].

[25] D. S. Akerib *et al.* (LUX), Phys. Rev. Lett. **112**, 091303 (2014), arXiv:1310.8214 [astro-ph].

[26] E. Aprile *et al.* (XENON10), Astropart. Phys. **34**, 679 (2011), arXiv:1001.2834 [astro-ph].

[27] P. F. Sorensen, *A Position-Sensitive Liquid Xenon Time-Projection Chamber for Direct Detection of Dark Matter: The XENON10 Experiment*, Ph.D. thesis, Brown U., Phys. Dept. (2008).

[28] X. Xiao *et al.* (PandaX), Phys. Rev. **D92**, 052004 (2015), arXiv:1505.00771 [hep-ex].

[29] V. N. Lebedenko *et al.* (ZEPLIN-III), Phys. Rev. **D80**, 052010 (2009), arXiv:0812.1150 [astro-ph].

[30] E. Aprile *et al.* (XENON100), Astropart. Phys. **35**, 573 (2012), arXiv:1107.2155 [astro-ph].

[31] G. J. Alner *et al.* (ZEPLIN-II), Astropart. Phys. **28**, 287 (2007), arXiv:astro-ph/0701858 [astro-ph].

[32] F. P. Santos, T. H. V. T. Dias, A. D. Stauffer, and C. A. N. Conde, J. Phys. D. Appl Phys. **27**, 42 (1994).

[33] S. F. Biagi, Nucl. Instrum. Meth. **A421**, 234 (1999), (Magboltz).

[34] A. Bailey, *Dark matter searches and study of electrode design in LUX and LZ*, Ph.D. thesis, Imperial Coll., London (2016).

[35] M. Lyly, J. Ruokolainen, and E. Järvinen, *ELMER - A finite element solver for multiphysics*, Tech. Rep. (CSC - IT Center for Sciene Ltd., P. O. Box 405, FI-02101 Espoo, Finland, 1999-2000) (Elmer).

[36] C. Geuzaine and J.-F. Remacle, Int. J. Numer. Meth. Eng. **79**, 1309 (2009), (Gmsh).

[37] R. Veenhof, in *Programming and mathematical techniques in physics. Proceedings, International Conference on programming and mathematical methods for solving physical problems, June 14-19, 1993, Dubna, Russia*, Conf. Proc., Vol. **C9306149** (1993) pp. 66–71, (Garfield++).

[38] A. Morozov, V. Solovov, R. Martins, F. Neves, V. Domingos, and V. Chepel, JINST **11**, P04022 (2016), ANTS Package Downloads, arXiv:1602.07247 [physics.ins-det].

[39] V. N. Solovov *et al.* (ZEPLIN-III), in *Nuclear Science Symposium and Medical Imaging Conference (NSS/MIC), 2011 IEEE* (2011) pp. 1226–1233, *Position Reconstruction in a Dual Phase Xenon Scintillation Detector*.

[40] D. W. Lynch and W. Hunter, in *Handbook of Optical Constants of Solids*, edited by E. D. Palik (Academic Press, Burlington, 1997) pp. 233–286.

[41] S. Stephenson, J. Haefner, Q. Lin, K. Ni, K. Pushkin, R. Raymond, M. Schubnell, N. Shutty, G. Tarlé, C. Weaverdyck, and W. Lorenzon, JINST **10**, P10040 (2015), arXiv:1507.01310 [physics.ins-det].

[42] F. Neves *et al.* (ZEPLIN-III), J. Instrum. **6**, P11004 (2011), arXiv:1106.0808 [astro-ph].

[43] E. Aprile, H. Contreras, L. W. Goetzke, A. J. Melgarejo Fernandez, M. Messina, J. Naganoma, G. Plante, A. Rizzo, P. Shagin, and R. Wall, J. Instrum. **9**, P11012 (2014), arXiv:1408.6206 [physics.ins-det].